

# **OPTIMIZATION AND FABRICATION OF A WIDENED X-BRANCH OPTICAL DEMULTIPLEXER IN GLASS**

**by Loïc Babin**

**Department of Electrical Engineering**

**Mc Gill University  
Montreal, Quebec**

**December 1993**

A thesis submitted to the Faculty of Graduate Studies and Research in partial fulfillment of the requirements for the degree of Master of Engineering

©Loïc Babin 1993



## Abstract

In this thesis, a widened X-branch optical waveguide by  $K^+$ - $Na^+$  ion-exchange in glass, to be used as a single mode-optical wavelength division demultiplexer (WDM) at the wavelengths  $1.31\mu\text{m}$  and  $1.55\mu\text{m}$  is designed, fabricated, and tested. The widened X-branch is a channel guide structure. To carry out the design, the effective-index method (EIM) together with the 2D-beam propagation method (FD-BPM), are employed. In order to get an accurate model for the lateral effective index in the channel guide, in the EIM, the diffusion process related to the ion-exchange is numerically simulated using an explicit 3D finite difference scheme. Experimentally, extinction ratios about -20 dB are obtained for TM mode devices, and in reasonably good agreement with the design predictions. These results are discussed and possible improvements to the present work are pointed out.

*A mes parents, pour le soutien et les encouragements,  
qu'ils m'ont apportés tout au long de mes études.*

*Ce travail est aussi le leur.*

## Résumé

L'objectif de cette thèse, était d'étudier d'un point de vue théorique, et de fabriquer, un démultiplexeur optique aux longueurs d'ondes  $1.31\mu\text{m}$  et  $1.55\mu\text{m}$ . La configuration que nous avons retenue pour notre démultiplexeur, est un guide d'onde du type "widened X-branch", réalisable pratiquement par échange ionique sodium-potassium sur substrat de verre. Les guides d'ondes d'une telle structure, sont à deux dimensions. Aussi, la méthode de l'indice effectif ainsi que la méthode BPM à deux dimensions ("Beam Propagation method") ont été employées pour les simulations numériques. Afin de disposer d'un modèle plus précis pour l'indice effectif, calculé par la méthode EIM, dans la direction transverse, nous avons simulé numériquement le processus de diffusion associé à l'échange ionique, en utilisant la méthode des différences finies à trois dimensions dans sa version explicite. Expérimentalement, nous avons pu effectivement séparer deux lumières de longueurs d'onde  $1.31$  et  $1.55\mu\text{m}$ , polarisées TM, avec un taux d'extinction d'environ  $-20$  decibels. Ces résultats sont en bon accord avec ceux des simulations numériques effectuées, ils sont discutés en conclusion de notre travail en même temps que la manière de les améliorer.

# Contents

## **CHAPTER 1: INTRODUCTION ..... p 1**

1.1 Overview of integrated optics ..... p 1

1.2 Wavelength division multiplexing technology (WDM) ..... p 2

1.3 Chapter description ..... p 5

## **CHAPTER 2: METHOD OF ANALYSIS FOR DIFFUSED OPTICAL WAVEGUIDES ..... p 9**

2.1 Wave equation ..... p 9

2.2 The effective index method (EIM) ..... p 12

2.3 The Runge-Kutta method ..... p 15

## **CHAPTER 3 WAVEGUIDES BUILT BY THE ION EXCHANGE PROCESS ..... p 21**

3.1 The ion-exchange technology ..... p 21

3.2 The ion exchange diffusion theory ..... p 22

3.3 Finite difference solution to the ion-exchange problem ..... p 25

3.4 Numerical results for the exchanged ion concentration ..... p 27

3.4.1 The single channel waveguide case ..... p 28

3.4.2 Coupled waveguides configuration ..... p 35

3.5 Numerical results for the index profile ..... p 36

3.6 Effective index modelling (EIM) ..... p 38

3.6.1 The single waveguide case ..... p 38

3.6.1.1 The solution by step index approximation ..... p 38

3.6.1.2 The semi analytical solution ..... p 39

3.6.1.3: Dispersion curves	p 40
3.6.2 Coupled waveguides	p 47
3.7 Conclusion	p 48

## CHAPTER: 4 DESIGNS OF A WIDENED X-BRANCH

### DEMULTIPLEXER ..... p 53

4.1 Introduction	p 53
4.2 The device operation principle	p 54
4.3 R parameter	p 58
4.4 Dispersion relation	p 59
4.4.1 The effective index method	p 60
4.4.2 The step index model	p 64
4.4.3 The side diffused model	p 67
4.4.4 Design example	p 71
4.4.5 Comparison between the step-index model and the side-diffused model	p 72
4.5 Design considerations	p 77
4.5.1 Device length	p 77
4.5.2 Effect of the taper branch angle	p 77
4.5.3 Waveguide width $w$ and diffusion time $t_d$	p 77
4.5.4 Bandwidth	p 81
4.5.5 Limitations of the design method	p 81
4.6 Conclusion	p 82

## CHAPTER 5: BEAM PROPAGATION ANALYSIS ..... p 89

5.1 General theory of the BPM	p 89
5.2 The EIM and the BPM method	p 91
5.3 The 2D finite difference method	p 92

5 3 1 The implementation . . . . .	p 92
5 3 2 Stability-Step size . . . . .	p 95
5 3 3 The boundary conditions . . . . .	p 96
5 3 4 The input excitation . . . . .	p 96
5 3 5 The output power evaluation . . . . .	p 97
5 4 BPM simulations . . . . .	p 98
5 4 1 Preliminary tests . . . . .	p 98
5 4 2 Numerical results for the design of the widened X-branch . . . . .	p 102
5 4 3 Radiation modes . . . . .	p 102
5 4 4 Fabrication tolerances . . . . .	p 103
5 5 Conclusion . . . . .	p 103

## **CHAPTER 6: EXPERIMENTAL RESULTS . . . . . p 115**

6 1 The photolithographic mask . . . . .	p 115
6.2 The fabrication process . . . . .	p 118
6 2 1 Substrate cleaning . . . . .	p 118
6 2.2 Metallization . . . . .	p 119
6 2 3 Photolithography . . . . .	p 119
6 2.4 The channel guide width measurement . . . . .	p 122
6 2 5 Ion-exchange . . . . .	p 124
6 2.6 Preparation of the samples for measurement . . . . .	p 124
6 3 Device testing . . . . .	p 127
6 3.1 Extinction ratio measurement tests . . . . .	p 126
6 3 2 Experimental results . . . . .	p 127
6 4 Conclusion . . . . .	p 128

## **CHAPTER 7: CONCLUSION . . . . . p 133**

# List of figures

## CHAPTER 1:

Fig 1.1 Signal powers $P$ and crosstalk powers $N$ at the ports of WDM devices . . . . .	p 3
Fig 1.2: Plan of the thesis . . . . .	p 6

## CHAPTER 2

Fig 2.1: Typical waveguiding structures . . . . .	p 10
Fig 2.2: Schematic representation of the EIM . . . . .	p 14
Fig 2.3: Order of the TE-TM mode calculation (example of a TE mode)	p 14

## CHAPTER 3

Fig 3.1: The ion exchange process to fabricate a channel waveguide . . . . .	p 23
Fig 3.2. The sodium ( $c_a$ ) and potassium ( $c_b$ ) concentrations in the glass during the ion-exchange . . . . .	p 23
Fig 3.3: Calculation grid for the solution of the exchange diffusion equations . . . . .	p 29
Fig 3.4: A 3-D plot of the concentration profile resulting from a single ion exchange ( $T=385^\circ\text{C}, t_d=270\text{min}, w=6.0\mu\text{m},$ $D_a=1.867 \times 10^{-4}\mu\text{m}^2/\text{s}$ ) . . . . .	p 33
Fig 3.5: Constant concentration contours produced by a single ion exchange ( $T=385^\circ\text{C}, t_d=270\text{min}, w=6.0\mu\text{m}, D_a=1.867 \times 10^{-4}\mu\text{m}^2/\text{s}$ ) (Single waveguide case) . . . . .	p 34
Fig 3.6: Compared concentration contours produced by an ion-exchange ( $T=385^\circ\text{C}, t_d=270\text{min}, w=6.0\mu\text{m}, D_a=1.867 \times 10^{-4}\mu\text{m}^2/\text{s}$ ) (Single waveguide case) . . . . .	p 35
Fig 3.7: Constant concentration contours resulting from a single ion- exchange( $T=385^\circ\text{C}, t_d=270\text{min}, w=6.0\mu\text{m}, D_a=1.867 \times 10^{-4}\mu\text{m}^2/\text{s}$ ) (Directional coupler configuration) . . . . .	p 37
Fig 3.8: Justification for using a linear interpolation between the discrete values of $n(x,y)$ (in this example $x=0$ ) . . . . .	p 42
Fig 3.9: Discrete values of the local effective index $N_{\text{eff}}(x)$ along with erf fit and step-index model (Ion exchange parameters $T=385^\circ, t_d=270\text{min}$ ) (Single waveguide case, TM modes.)	p 43

Fig 3.10 Dispersion curve  $V'$  vs  $b'$  (normalized parameters) . . . . . p 46

Fig 3.11 Discrete values of the local effective index  $N_{\text{eff}}(x)$  along with erf fit and step-index model (Ion exchange parameters:  $T=385^\circ, t_d=270\text{min}$ ). (directional coupler configuration, TM modes) . . . . . p 49

**CHAPTER 4:**

Fig 4.1. Widened X-branch perspective view . . . . . p 55

Fig 4.2 The symmetric and antisymmetric modes in the central and tapered regions . . p 55

Fig 4.3: Lateral effective index for the widened X-branch . . . . . p 63

Fig 4.4 Lateral effective index in the tapered regions . . . . . p 64

Fig 4.5:  $\Delta\beta_c$  vs  $t_d$  for different waveguide widths  $w$  at  
 $\lambda=1.31\mu\text{m}, 1.55\mu\text{m}$  . . . . . p 68

Fig 4.6:  $\beta_s(\lambda), \beta_a(\lambda)$  vs  $s$  at  $\lambda=1.31\mu\text{m}, 1.55\mu\text{m}$  ( $w=6.0\mu\text{m}$ ) . . . . . p 69

Fig 4.7:  $\Delta\beta_s(\lambda)$  vs  $s$  at  $\lambda=1.31\mu\text{m}, 1.55\mu\text{m}$  ( $w=6.0\mu\text{m}$ ) . . . . . p 69

Fig 4.8:  $\phi_s(\lambda)$  vs  $\alpha$  at  $\lambda=1.31\mu\text{m}, 1.55\mu\text{m}$  ( $w=6.0\mu\text{m}$ ) . . . . . p 70

Fig 4.9:  $R_1^m$  and  $R_2$  vs  $t_d$  ( $w=6.0\mu\text{m}$ ) . . . . . p 73

Fig 4.10 Field plots for the TM modes in the widened  
X-branch ( $E_y$ ) (lateral dependence in the central and tapered regions) . . . . . p 75

Fig 4.11:  $\Delta\beta_c(\lambda=1.31\mu\text{m}) - \Delta\beta_c(\lambda=1.55\mu\text{m})$  vs  $t_d$  for different  
waveguide widths  $w$  (The side diffused model is assumed for  
the index profile)  
. . . . . p 79

Fig 4.12: Extinction ratio  $ER(\lambda)$  vs diffusion time deviation  
 $\Delta t_d$  (Device design parameters  $w=6.0\mu\text{m}, t_d=257\text{min}, L=3100\mu\text{m}, \alpha=0.5^\circ$ )  
TM modes . . . . . p 79

Fig 4.13: Extinction ratio  $ER(\lambda)$  vs waveguide width deviation  $\Delta(2w)$  (Device design parameters  
 $w=6.0\mu\text{m}, t_d=257\text{min}, L=3100\mu\text{m}, \alpha=0.5^\circ$ ) TM modes . . . . . p 83

Fig 4.14: Extinction ratio  $ER(\lambda)$  vs diffusion time  
deviation  $\Delta t_d$  when an error of  $-0.2\mu\text{m}$  is assumed on the central width  $2w$  (Device design  
parameters  $w=6.0\mu\text{m}, t_d=257\text{min}, L=3100\mu\text{m}, \alpha=0.5^\circ$ ) TM modes . . . . . p 83

Fig 4.15 Cascaded structure . . . . . p 84

Fig 4.16: Extinction ratio  $ER(\lambda)$  of a cascaded structure vs

central width deviation  $\Delta(2w)$  . . . . . p 84

Fig 4.17: Extinction ratio  $ER(\lambda)$  vs wavelength deviation

$\Delta\lambda$  (Device design parameters  $w=6.0\mu\text{m}, t_d=257\text{min}, L=3100\mu\text{m},$   
 $\alpha=0.5^\circ$ ) TM modes . . . . . p 85

## CHAPTER 5:

Fig 5.1: Schematic representation of the 2D FD-BPM method . . . . . p 94

Fig 5.2: Guide field propagating along a uniform two mode  
single waveguide with side diffused boundaries ( $t_d=270\text{min}, w=12.0\mu\text{m}$ , the even and odd order  
TM modes are excited with the same amplitude at the input) . . . . . p 99

Fig 5.3: Normalized power  $P_1(z)$  in region 1 ( $x>0$ ),  
( $0<z<2000\mu\text{m}$ ) ( $v=0.55$  in the BPM) . . . . . p 100

Fig 5.4:  $W(z), P_1(z), W(z)$ .  $W(z)$ (Hanning window) $=1-\cos(2\pi z/Z)$  ( $Z=50000\mu\text{m}, 0<z<Z$ ) ( $v=0.55$  in  
the BPM) . . . . . p 100

Fig 5.5: Fast fourier transform (FFT) of  $P_1(z)$  . . . . . p 100

Fig 5.6: Phase angle  $2\phi_1(\lambda)$  vs branching angle  $\alpha$  at  $\lambda=1.31\mu\text{m}, 1.55\mu\text{m}$ ,  
( $t_d=270\text{min}, w=6.0\mu\text{m}$ ) . . . . . p 101

Fig 5.7: Optical field in the tapered regions ( $w=6.0\mu\text{m}, t_d=270\text{min}$ , TM modes,  $\lambda=1.55\mu\text{m}$ ) p 101

Fig 5.8:  $L$  and  $t_d$  vs  $w$  (TE, TM modes,  $\alpha=0.5^\circ$ ) . . . . . p 104

Fig 5.9: BPM simulation of the widened X-branch demultiplexer  
 $m=10, t_d=287\text{min}, L=3370\mu\text{m}, w=6.0\mu\text{m}, \alpha=0.5^\circ$ , TM modes . . . . . p 105

Fig 5.10: BPM simulation of the widened X-branch demultiplexer  
 $m=9, t_d=257\text{min}, L=3100\mu\text{m}, w=6.0\mu\text{m}, \alpha=0.5^\circ$ , TM modes . . . . . p 106

Fig 5.11: BPM simulation of the widened X-branch demultiplexer  
 $m=8, t_d=232\text{min}, L=2830\mu\text{m}, w=6.0\mu\text{m}, \alpha=0.5^\circ$ , TM modes . . . . . p 107

Fig 5.12: BPM simulation of the widened X-branch demultiplexer  
 $m=7, t_d=209\text{min}, L=2570\mu\text{m}, w=6.0\mu\text{m}, \alpha=0.5^\circ$ , TM modes . . . . . p 108

Fig 5.13: BPM simulation of the widened X-branch demultiplexer  
 $m=10, t_d=375\text{min}, L=3140\mu\text{m}, w=6.0\mu\text{m}, \alpha=0.5^\circ$ , TE modes . . . . . p 109

Fig 5.14: BPM simulation of the widened X-branch demultiplexer  
 $m=10, t_d=227\text{min}, L=2400\mu\text{m}, w=6.0\mu\text{m}, \alpha=1.2^\circ$ , TM modes . . . . . p 110

Fig 5.15: ER vs  $\Delta(2w)$  waveguide width deviation (Device design parameters  $w=6.0\mu\text{m}, t_d=257$   
 $\text{min}, L=3100\mu\text{m}, \alpha=0.5^\circ$ , TM modes) . . . . . p 111

Fig 5.16: ER vs $\Delta(t_d)$ waveguide width deviation (Device design parameters $w=6.0\mu\text{m}, t_d=257$ min, $L=3100\mu\text{m}, \alpha=0.5^\circ$ , TM modes) . . . . .	p 111
Fig 5.17: ER vs $\Delta(t_d)$ waveguide width deviation when an error of $-0.2\mu\text{m}$ is assumed on the central width $2w$ (Device design parameters $w=6.0\mu\text{m}, t_d=257$ min, $L=3100\mu\text{m}, \alpha=0.5^\circ$ , TM modes) . . . . .	p 112
Fig 5.18: ER vs $\Delta\lambda$ wavelength deviation (Device design parameters $w=6.0\mu\text{m}, t_d=257$ min, $L=3100\mu\text{m}, \alpha=0.5^\circ$ , TM modes) . . . . .	p 112

## CHAPTER 6:

Fig 6.1: Photolithographic mask . . . . .	p 117
Fig 6.2: Resist pattern (after developing) . . . . .	p 120
Fig 6.3: Al diffusion mask pattern (after etching and resist removal) . . . . .	p 121
Fig 6.4: The waveguide width measurement set-up . . . . .	p 123
Fig 6.5: Diamond cutting of a sample . . . . .	p 125
Fig 6.6: Device fabrication process . . . . .	p 126
Fig 6.7: Measurement set-up . . . . .	p 129
Fig 6.8: Fiber butt-coupling . . . . .	p 130
Fig 6.9: Output spots at end facet . . . . .	p 131
Fig 6.10. Video signal on the oscilloscope . . . . .	p 131
Fig 6.11. Output spots at end facet . . . . .	p 131
Fig 6.12: Video signal on the oscilloscope . . . . .	p 131

## CHAPTER 7:

Fig 7.1: Multichannel wavelength demultiplexer using cascaded widened X-branch . . .	p 135
--	-------

# List of tables

## CHAPTER 1:

Table 1.1: Typical performances of different classes of wavelength multi/demultiplexers . p 3

## CHAPTER 3:

Table 3.1: A typical output of the program used to calculate the concentration profile of exchanged ions ( $T=385^\circ$ ,  $t_d=270\text{min}$ ,  $w=6.0\mu\text{m}$ ,  $D_d=1.867\times 10^{-4}\mu\text{m}^2/\text{s}$  . . . . . p 34

Table 3.2: Calculated effective index  $n_{\text{eff}}=\beta/k_0$   
(Single waveguide configuration TM modes) . . . . . p 44

## CHAPTER 4:

Table 4.1: Index  $N_p$  and normalized parameters  $V'(w)$ ,  $V'(2w)$   
vs  $t_d$  . . . . . p 61

Table 4.2: Design values  $t_d, m, L$  for TM, TE modes,  $\alpha=0.5^\circ$  or  
 $\alpha=0.8^\circ$  ( $w=6.0\mu\text{m}$ ) . . . . . p 74

## CHAPTER 5:

Table 5.1:  $ER(\lambda)$  and  $L_R(\lambda)$  vs branching angle  $\alpha$  . . . . . p 110

Table 5.2:  $ER$  vs  $\Delta(2w)$  waveguide width deviation (Device  
design parameters  $w=6.0\mu\text{m}$ ,  $t_d=257$  min,  $L=3100\mu\text{m}$ ,  $\alpha=0.5^\circ$ ,  
TM modes) . . . . . p 111

Table 5.3:  $ER$  vs  $\Delta(t_d)$  waveguide width deviation (Device  
design parameters  $w=6.0\mu\text{m}$ ,  $t_d=257$  min,  $L=3100\mu\text{m}$ ,  $\alpha=0.5^\circ$ ,  
TM modes) . . . . . p 111

Table 5.4:  $ER$  vs  $\Delta(t_d)$  waveguide width deviation when an  
error of  $-0.2\mu\text{m}$  is assumed on the central width  $2w$  (Device  
design parameters  $w=6.0\mu\text{m}$ ,  $t_d=257$  min,  $L=3100\mu\text{m}$ ,  $\alpha=0.5^\circ$ ,  
TM modes) . . . . . p 112

Table 5.5:  $ER$  vs  $\Delta\lambda$  wavelength deviation (Device design  
parameters  $w=6.0\mu\text{m}$ ,  $t_d=257$  min,  $L=3100\mu\text{m}$ ,  $\alpha=0.5^\circ$ , TM modes) . . . . . p 112

## CHAPTER 6:

Table 6.1: Measured extinction ratio (TM modes,  $\alpha=0.5^\circ$ ) . . . . . p 132

## List of symbols

In this thesis, we use the following representation for the electromagnetic fields of guiding structures:

$$\begin{aligned} \mathbf{E} &= (\mathbf{E}_1(x,y,z) + \mathbf{E}_2(x,y,z))e^{j\omega t} & \mathbf{H} &= (\mathbf{H}_1(x,y,z) + \mathbf{H}_2(x,y,z))e^{j\omega t} \\ &= (\mathbf{e}_1(x,y,z) + \mathbf{e}_2(x,y,z))e^{j(\omega t - \beta z)} & &= (\mathbf{h}_1(x,y,z) + \mathbf{h}_2(x,y,z))e^{j(\omega t - \beta z)} \end{aligned}$$

$b', b_0$ : Waveguide normalized parameter

$c_a, c_b$ : Respective potassium and sodium concentrations

$c$ : Normalized exchanged-ion (potassium) concentration

$d$ : Diffusion depth

$D_a, D_b$ : Inter diffusion constants for the potassium and sodium respectively

$D_e$ : Effective diffusion constant

ER: extinction ratio

$J_a, J_b$ : Ionic flux for the potassium and sodium respectively

$k_B$ : Boltzmann constant

$k$ : Wavevector

$L$ : Length of the central region of the widened X-branch

$l_t$ : Length of the tapered regions of the widened X-branch

$m$ : Number of coupling length

$N_p$ : Effective index of a slab waveguide exchanged for the amount of time  $t_d$

$n_b$ : Substrate index

$n_{eff}$ : Effective index of a guided mode

$N_{eff}(x)$ : Effective index in the lateral direction in the EIM

$n_s$ : Surface index

$p, s$ : Waveguide spacing ( $s=p-w$ )

$T$ : Diffusion temperature

$t_d$ : Diffusion time

$V, V_0$ : Waveguide normalized parameter

$w$ : Waveguide width

$2w_c$ : Waveguide width in the central region of the widened X-branch

$w_t$ : Waveguide width in the tapered regions of the widened X-branch

$\alpha$ : Branching angle of the widened X-branch or diffusion parameter

$\alpha$ : Normalized diffusion parameter

$\beta$ : Propagation constant of a guided mode

$\beta_s, \beta_a$ : Respective propagation constants of the symmetric, and antisymmetric modes of the widened X-branch

$\Delta\beta_c, \Delta\beta_t$ : Difference between the propagation constants of the symmetric and antisymmetric modes of the widened X-branch in the central, and tapered regions respectively

$\Delta n_s$ : Index change at the surface

$\epsilon$ : Dielectric constant

$\lambda$ : Wavelength

$\mu_0$ : Permittivity

$\phi$ : Total phase angle difference between the symmetric and antisymmetric modes at the output of the widened X-branch

$\phi_c, \phi_t$ : Phase angle due to the central and tapered regions respectively

## Acknowledgements

I would like to thank my supervisor, Dr. Gai Lam Yip for his guidance and encouragement during the course of this research work, for his thorough correction of this thesis first draft and for helping me catch the thesis submission deadline I had to respect, due to personal military obligations.

I am also very grateful to Feng Xiang and Peter Noutsios, who are currently proceeding toward a PhD degree. Their technical expertise greatly helped me to complete this work. In particular, I would like to thank Feng Xiang for his patience and availability when teaching me the experimental techniques.

Fruitful discussions with Dennis Kan presently working at Newbridge Inc. (Ottawa) and Philippe Allard presently working at BNR Canada (Montreal), are also acknowledged. I have also benefited from the assistance of Joseph Mui, electronics technician, who helped me take the pictures presented at the end of this thesis.

Finally, I would like to thank the integrated optics group as a whole. The warm welcome they gave me, made my stay in Montreal all the more enjoyable.

This research was partly supported through a grant from "Le conseil de la Region Rhône-Alpes (France)".

# CHAPTER 1

## INTRODUCTION

### 1.1 Overview of integrated optics

The term integrated optics (IO) was first used by Stewart E. Miller [1] in 1969 to describe the optics of miniaturized optical circuits in which light signals are generated, guided and processed by related effects before finally being detected. At that time thin-film and microfabrication technology were relatively new. Various thin-film waveguide device could not be implemented. During the last ten years, however, semiconductor laser diodes used as optical sources and optical fibers as optical transmission media, as well as other optical components and devices, which are waveguides necessary for optical communication systems, have been improved and are now readily available. Optical waveguide devices have come to be recognized as promising devices [2-3]. Optical integrated circuits can be divided into two groups:

-One group, a monolithic type, integrates all components, such as the source, waveguide circuits and detectors on a common III-V semiconductor substrate. The problem is that for guiding and modulating purposes semiconductor materials still have relatively low electro-optic coefficient and high losses. Great efforts have been made to improve the optical properties of semiconductors and an InP/GaInAsP rib waveguide with a loss as low as 0.18 dB/cm has been demonstrated [4].

-In the meantime, however, hybrid type circuits have also been developed. This represents the second group of devices. They are passive circuits on a dielectric substrate which are externally coupled to the source and detector. For this class of devices, glass waveguides are prime candidates because of their compatibility with optical fibers, low cost, low propagation losses, and ease of integration [2]. Because of its high electrooptic coefficient lithium niobate ( $\text{LiNbO}_3$ ) is the premier material for electro-optic components. Many high performance modulators and switches have been realized on this type of substrate [5-6].

Since integrated optics is based on a thin film technology, the implementation of the proposed

devices requires almost the same thin-film processing techniques as used in the semiconductor technology. However, main differences arise in the materials and substrates used. Using glass as a substrate, ion-exchange is the most favorable technique to form optical waveguides [7]. Sputtering, plasma etching or ion-beam milling are also applied to fabricate the ridge-type waveguides [8]. For the  $\text{LiNbO}_3$  material, the most widely employed process is the diffusion of titanium into  $\text{LiNbO}_3$  [9]. Also, a proton-exchange technique has been developed. In the case of semiconductor materials like GaAs and InP, the waveguides are formed by methods such as liquid phase epitaxy (LPE), metal organic chemical vapor deposition (MOCVD), molecular beam epitaxy (MBE) or ion implantation [10]. Although the packing density of integrated optics is still many times less than in the microelectronics, the required pattern accuracy is sometimes considerably greater [11].

### 1.2 Wavelength Division Multiplexing Technology (WDM)

WDM allows modulated radiation from several light sources of clearly distinct wavelengths to be transmitted simultaneously over a single fiber. There is a growing interest for this technology these days. Indeed, it presents numerous advantages: transmission capacity increase per fiber, system cost reduction, simultaneous transmission of signals modulated with different schemes and service channel expandability after fiber installation [12]. Spectrally selective optical multiplexers, demultiplexers or duplexers (See Fig 1.1) are needed, at the start and end of the transmission route to ensure the low-loss combination of light at the various wavelengths [13]. Multimode MUX-DEMUX's has been realized, but in actual high performance communications systems, monomode operation is preferable. The realization of single mode MUX-DEMUX's can be accomplished by using wavelength dispersive elements like optical interference filter [14], optical diffraction gratings [15] and wavelength selective coupling between two adjacent waveguides [16-17]. The important figures when these devices are used for demultiplexing are the extinction ratio, the power loss, and the channel spacing. The extinction ratio  $ER(\lambda)$  is the ratio between the power transmitted at one wavelength in its allotted channel, to the power leaked into the other channels (See Fig 1.1). The channel spacing is the smallest interval of wavelength

## Chapter 1: Introduction

that a device can separate. The power loss is the amount of power lost between the input and the output of a device because of its imperfections (part of the guided power is converted into radiated power). Of course, extinction ratios should be maximized and power losses minimized to get the optimal device characteristics. In Table 1.1 [12], typical performance characteristics of integrated optics multi/demultiplexers are listed.

**Fig 1.1: Signal powers  $P$  and crosstalk powers  $N$  at the ports of WDM devices**

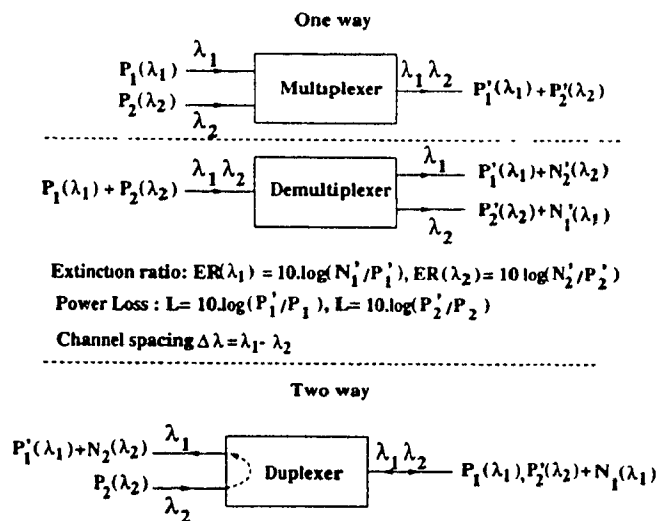


**Table 1.1: Typical performances of different classes of wavelength multi/demultiplexers**

	Interference Filter	Grating	Directional Coupler	X-branch
Number of channels	2-6	3-20	2-8	2-8
Insertion loss	0.5-5 dB	1-4 dB	0.6-2 dB	0.6-2 dB
Channel spacing	30-100 nm	1-40 nm	40-200 nm	40-200 nm
Extinction ratio	20-30 dB	20-30 dB	10-13 dB	>20 dB

## Chapter 1: Introduction

---

When a transmission system does require a great number of channels, optical interference or grating type filters are to be used. The problem is that the design and fabrication of these devices are not very simple. GRIN (graded-index) or ball lenses have to be implemented in the case of optical filters [14], and in the case of gratings [15] the control of the process is difficult. When one wants to separate only a small number of channels (2 to 10), one can consider wavelength selective coupling type multi-demultiplexers. They are simpler to design and fabricate. They can have a periodic wavelength transmission curve or exhibit a band pass behavior [18], and are well suited for bidirectional transmission: a single device connected to a single fiber can work as a demultiplexer for the incoming signals and multiplexer for the outgoing signals (duplexing). Directional couplers [17],[19], asymmetric Y-branch junction [20], X-branch [21], and widened X-branch [22], have been studied for WDM applications in numerous papers [23]. Indeed, from the considered fabrication technologies, integrated optics technology offers the greatest potential of building compact multi/demultiplexers in a stable and rugged structure with a simplified assembly.

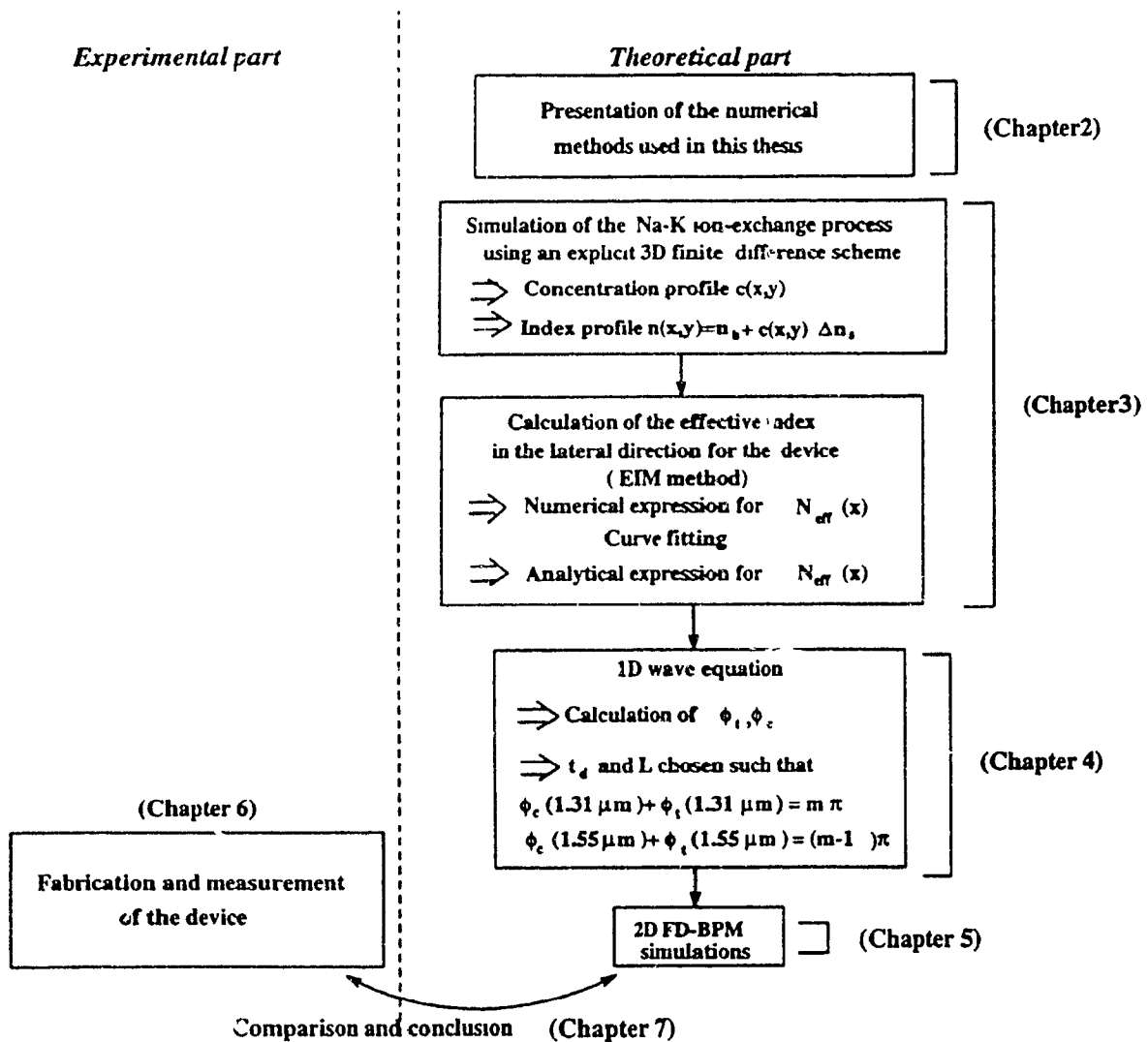
The widened X-branch demultiplexer was recently proposed [18],[22] to overcome the sensitivity of asymmetry to the individual waveguides of the directional coupler. Based on the wavelength dependence of the two-mode interference (TMI) it has been experimentally demonstrated [22]. This type of structure is more compact and fabrication tolerant so that it provides a powerful alternative to directional coupler structure especially for WDM applications. Previously most people only tried the configuration in the  $\text{LiNbO}_3$  substrate material. For the sake of lower cost, and simpler fabrication techniques it is also beneficial to apply the same configuration by the ion-exchange technique using a soda-lime glass substrate. A first theoretical study of the problem was made in our laboratory in 1991 [24], and experimentally the feasibility of such a device on a glass substrate has been demonstrated by Morasca [25]. The purpose of this thesis was to propose an optimal design procedure, build the device, and actually test the optimized design results (extinction ratio as high as possible) with the corresponding experimental results of implementing the device.

### 1.3 Chapter description

In Chapter 2, the numerical tools that we used in our design computations are presented. In order to fully characterize the index profile of the widened X-branch structure, we studied the ion exchange diffusion process in Chapter 3. In Chapter 4 the characteristics of the widened X-branch are studied. In Chapter 5 the beam propagation method (BPM) is used to simulate the device function. The experimental results are presented in Chapter 6 in comparison with theory. Chapter 7 draws some conclusions from the present work.

Fig 1.2: Plan of the thesis

Design and fabrication of a widened X-branch demultiplexer  
at 1.31 $\mu\text{m}$  and 1.55 $\mu\text{m}$  by  $\text{K}^+\text{-Na}^+$  ion exchange in glass



## References

- [1] S. E. Miller, "Integrated optics: an introduction", Bell System Tech. J., Vol 48, pp 2059-2069, 1969.
- [2] W. J. Tomlinson and C. A. Brackett, "Telecommunication applications of integrated optics and optoelectronics", Proc. IEEE, Vol 75, pp.1512-1523, 1987.
- [3] S. R. Forrest, "Optoelectronic Integrated Circuits", Proc. IEEE, Vol 75, pp.122-125, 1987.
- [4] J. H. Angenent, M. Ernam, J.M. Auger and R. Gamonal, "Extremely low loss InP/GaInAsP rib waveguides", Electron. Lett., Vol 25 pp.628-629, 1989.
- [5] F. Koyma and K. Iga, "Frequency chirping of external modulation and its reduction", Electron. Lett., Vol 21, pp.1065-1066, 1985.
- [6] P. Cranestand, B. Stolz, L. Bergvall, W. Doldissen, H. Heidrich and D. Hoffman, "Strictly non blocking 8x8 integrated optic switch matrix", Electron. Lett., Vol 22, pp.816-817, 1986.
- [7] T. Finkadly, "Glass waveguides by ion exchange: a review", Opt. Eng., Vol 24, pp.244-250, 1985.
- [8] H. Nishihara, M. Haruna and T. Suhara, "Optical integrated circuits", New York : Mc Graw Hill 1989.
- [9] E. Voges and A. Neyer, "Integrated optics device on LiNbO<sub>3</sub> for optical communication", IEEE J. of Lighthwave Tech., Vol LT-5, pp.1229-1238, 1987.
- [10] D. H. Lee, "Electromagnetic theory of integrated optics", New York, Academic Press, 1986.
- [11] F. Auracher, H. F. Mahlein and G. Winzer, "Development trends in integrated optics", Telecom Report 10 (Germany), n°4, pp.148-156, 1987.
- [12] O. E. Delange, "Wideband optical communication systems: part2-frequency division multiplexing", Proc. IEEE, Vol 58, pp.1683-1690, 1970.
- [13] G. Winzer, "Wavelength multiplexing components-A review of single mode devices and their applications ", IEEE J. of Lighthwave Tech., Vol 2, pp.369-378, August 1984.
- [14] H. Nishihara, M. Haruna and T. Suhara, "Optical integrated circuits", New York · Mc Graw Hill 1989, pp.265-273, 1989.

## Chapter 1: Introduction

---

- [15] T. Suhara and H. Nishihara, "Integrated optics components and devices using periodic structures", IEEE J. of Quantum Electron., Vol 22, pp.847-865, 1986.
- [16] M. Digonnet and H. J. Shaw, "Wavelength multiplexing in single-mode fiber couplers", Appl. Opt., Vol 22, pp.484-491, 1983.
- [17] R. C. Alferness and R. V. Schmidt, "Tunable optical waveguide directional coupler filter", Appl Phys. Lett., Vol 33, pp.161-163, 1978.
- [18] Y. Chung, J. Y. Yi, S. H. Kim and S. S. Choi, "Analysis of a tunable multichannel two mode interference wavelength division multiplexer-demultiplexer", IEEE J. of Lightwave Tech., pp.766-776, Vol LT-7, 1989.
- [19] H. C. Cheng and R. V. Ramaswamy, "A dual wavelength 1.3-1.55 $\mu$ m directional coupler wavelength multi-demultiplexer using ion exchange in glass", presented at CLEO/IQEC'90, Anaheim (Ca), Paper CThI53, 1990.
- [20] N. Goto and G. L. Yip, "Y-branch wavelength multi-demultiplexer for  $\lambda=1.30 \mu\text{m}$  and  $\lambda=1.55 \mu\text{m}$ ", Electronics letters, Vol 26, pp.102-103, 1990.
- [21] A. Neyer, "Electrooptic X-switch using single mode Ti:LiNbO<sub>3</sub> channel waveguides", Electron. Lett, pp.553-554, 1983.
- [22] F. Rottmann, A. Neyer, W. Mevenkamp and E. Voges, "Integrated-optic wavelength multiplexers on Lithium Niobate based on two mode interference", IEEE J. of Lightwave Technology, Vol 6, pp.947-952, 1988.
- [23] G. E. Betts and W. S. Chang, "Crossing channel waveguide electrooptic modulators", IEEE J. of Quantum Electron, Vol QE-22, pp. 1027-1028, 1986.
- [24] J. Y. Chen, "Design considerations of a planar cross channel optical demultiplexer", M. Eng. Thesis., Elect. Eng. Dept., Mc Gill University, December 1991.
- [25] C. De Bernardi, S. Morasca, D. Scarano, "Low loss, high performance integrated optic wavelength demultiplexers fabricated by N<sub>a</sub>-K ion exchange on glass", SPIE 1989

## CHAPTER 2

### METHODS OF ANALYSIS FOR DIFFUSED OPTICAL WAVEGUIDES

The characteristics of the propagating modes in waveguides are obtained by solving the wave equation, derived from Maxwell's equation, for the corresponding boundary value problems. Usually, the refractive index increment of a waveguide formed in the substrate by the ion-exchange technology, the fabrication technology considered in this thesis, is distributed. The fully analytical solutions for the vectorial electromagnetic fields are not obtainable for most of the practical cases. Therefore, using some approximate or numerical method applicable to the studies of optical waveguides with arbitrary index distribution is necessary for engineering device designs and fabrications.

In this Chapter, the transverse wave equation for waveguide structures under a weak guidance condition is derived (Section 2.1). The effective-index modelling EIM (2.2) [1] and Runge-Kutta method (2.3) [2-3] are introduced as two powerful tools to help solve this equation.

#### 2.1 Wave equation

For general waveguiding structures (See Fig2.1) Maxwell's equation are written as:

$$\nabla \times \vec{H} = n^2 \epsilon_0 \frac{d\vec{E}}{dt} \quad 2.1$$

$$\nabla \times \vec{E} = -\mu_0 \frac{d\vec{H}}{dt} \quad 2.2$$

$$\nabla \cdot [n^2 \epsilon_0 \vec{E}] = 0 \quad 2.3$$

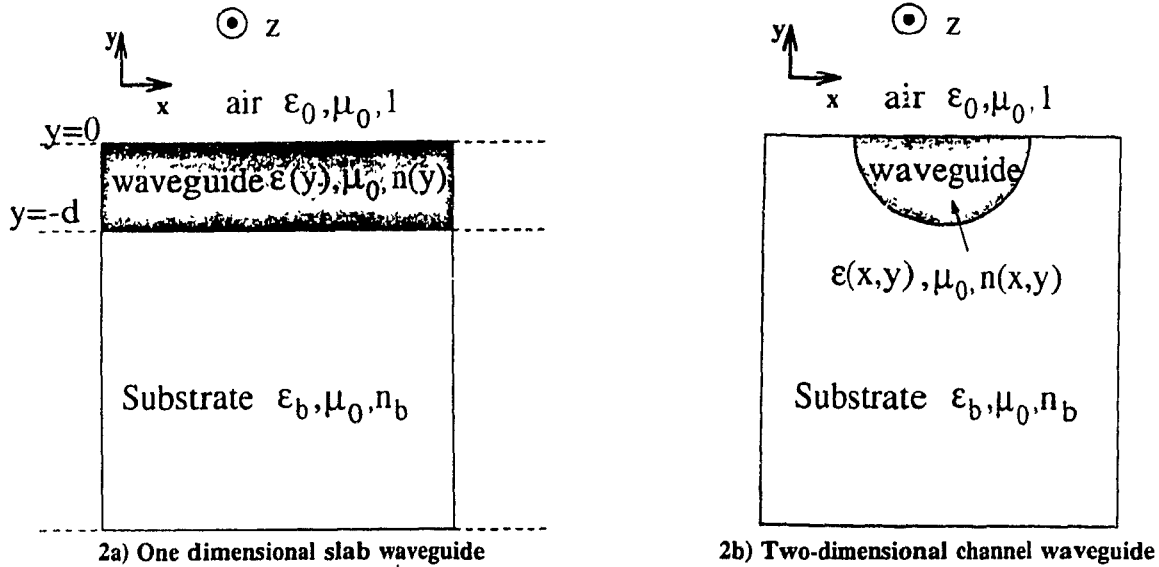
$$\nabla \cdot \vec{H} = 0 \quad 2.4$$

where  $n$  is the refractive index:  $n=1$  in the air,  $n=n_0$  in the substrate, and in general inside the

**Chapter 2: Methods of analysis for diffused optical waveguides**

waveguide  $n=n(x,y,z)$ .

**Fig 2.1: Typical waveguiding structures**



If we apply the curl operator to eqn(2.2) and use eqn(2.1) to eliminate H, we find

$$\nabla \times (\nabla \times \vec{E}) = -\mu_0 \epsilon_0 n^2 \frac{d\vec{E}}{dt} \quad 2.5$$

Using the vector identity:

$$\nabla \times (\nabla \times \vec{E}) = \nabla (\nabla \cdot \vec{E}) - \nabla^2 \vec{E} \quad 2.6$$

together with eqn(2.3), eqn(2.5) becomes:

$$\nabla^2 \vec{E} + \nabla \left[ \frac{\vec{E} \cdot \nabla (n^2)}{n^2} \right] + k_0^2 n^2 \vec{E} = 0, \quad 2.7$$

assuming the time dependence  $\exp(+j\omega t)$  and the conventional notation  $k_0^2 = \omega^2 \mu_0 \epsilon_0$ .

## Chapter 2: Methods of analysis for diffused optical waveguides

---

Similarly, the corresponding wave equation for the magnetic field can be derived from the equations (2.1) to (2.4) as:

$$\nabla^2 \vec{H} + \left[ \frac{\nabla n^2}{n^2} \times (\nabla \times \vec{H}) \right] + k_0^2 n^2 \vec{H} = 0 \quad 2.8$$

From now on, we will assume that the index does not vary along the longitudinal direction (+z direction). The vector wave equation just for the transverse field components can be separated from the equations (2.7) and (2.8) as:

$$\nabla_{\perp}^2 \vec{e}_t + \nabla_{\perp} [\vec{e}_t \cdot [\nabla_{\perp} \ln(n^2(x,y))]] + [k_0^2 n^2(x,y) - \beta^2] \vec{e}_t = 0 \quad 2.9$$

$$\nabla_{\perp}^2 \vec{h}_t + \frac{\nabla_{\perp} n^2(x,y)}{n^2(x,y)} \times (\nabla_{\perp} \times \vec{h}_t) + [k_0^2 n^2(x,y) - \beta^2] \vec{h}_t = 0 \quad 2.10$$

where a z-dependence as  $\exp(-j\beta z)$  is assumed and  $\nabla_{\perp} = \partial^2/\partial x^2 + \partial^2/\partial y^2$ .

For ion exchange diffused waveguides  $\nabla_{\perp}(n^2(x,y))$  is very small and it can be neglected. This was verified by use of the Beam Propagation Method Chapter 5. Under this approximation (the so called scalar wave approximation), any transverse component of the field satisfies the well-known relation:

$$\nabla_{\perp}^2 \psi + [k_0^2 n^2(x,y) - \beta^2] \psi = 0 \quad 2.11$$

### TE-TM modes

However, there are still polarization discrepancies between the propagating modes due to the waveguide surface step index change with polarization and the different boundary conditions which must be satisfied by the E and H fields.

The propagating modes can be distinguished as TE modes with:

$$e_y = h_x = e_z = 0; h_y = \frac{\beta}{\omega \mu_0} e_x; h_z = -\frac{j}{\omega \mu_0} \frac{\partial e_x}{\partial y} \quad 2.12$$

and TM modes with:

$$e_x = h_y = h_z = 0 ; e_y = -\frac{\beta}{\omega \epsilon_0 n^2(x,y)} h_x ; e_z = \frac{j}{\omega \epsilon_0 n^2(x,y)} \frac{\partial h_x}{\partial y} \quad 2.13$$

This formulation is rigorous for one dimensional problems.

From the above derivations we know under the weak guidance condition, that glass optical waveguide analysis is possible under certain approximations. In the following sections, two numerical method are discussed for the practical study of waveguides with an arbitrary index distribution.

## 2.2 The effective index method (EIM)

### 2.2.1 Derivation of the method

The effective index method (EIM) is an effective tool in the analysis of optical waveguides. If the cross sectional shape and the refractive index profile of the waveguide are known, the EIM can be used to find its mode dispersion characteristics. Knos and Toullos [1] first proposed the effective index method in 1970. Since then, this method has become quite popular due to its simplicity, efficiency and close agreement with exact results [4-6]. The method has been first developed for steplike index profile but its applicability to graded index structures has also been demonstrated [5-6].

Basically, the EIM is a way to solve the two dimensional wave equations by solving a set of one dimensional wave equations which are far easier to handle. In a 2D structure, oriented such that its long dimension is along x (lateral direction) and its short dimension along y (depth direction) (see Fig 2.1), quasi TE and TM modes obey the usual two dimensional wave equation, derived in the previous paragraph (See eqn 2.11):

$$\frac{\partial^2 \psi}{\partial x^2} + \frac{\partial^2 \psi}{\partial y^2} + [k_0^2 n^2(x,y) - \beta^2] \psi = 0 \quad 2.14$$

## Chapter 2: Methods of analysis for diffused optical waveguides

---

with  $\psi = e_y(x,y)$  for TE modes, and  $\psi = h_y(x,y)$  (for TM modes).

We can look for solutions of the form  $\psi(x,y) = F(x,y)G(x)$ . Using this expression, we get for eqn(2.14)[7]:

$$G \frac{\partial^2 F}{\partial x^2} + G \frac{\partial^2 F}{\partial y^2} + F \frac{\partial^2 G}{\partial x^2} + 2 \frac{\partial F}{\partial x} \frac{\partial G}{\partial x} + [k_0^2 n^2(x,y) - \beta^2] FG = 0 \quad 2.15$$

We can define an effective index in the lateral direction  $N_{eff}(x)$  such that:

$$\frac{\partial^2 G}{\partial x^2} + [k_0^2 N_{eff}^2(x) - \beta^2] G = 0 \quad 2.16$$

Then eqn(2.14) becomes:

$$G \frac{\partial^2 F}{\partial x^2} + G \frac{\partial^2 F}{\partial y^2} + 2 \frac{\partial F}{\partial x} \frac{\partial G}{\partial x} + k_0^2 [n^2(x,y) - N_{eff}^2(x)] FG = 0 \quad 2.17$$

which can be reduced to a 1D problem in  $x$  for  $F(x,y)$  (with  $x$  as a parameter) by assuming that most of the variation in  $x$  is taken up by  $G(x)$  and that the second and third terms are negligible.

Under this assumption, eqn(2.17) becomes

$$\frac{\partial^2 F}{\partial y^2} + k_0^2 [n^2(x,y) - N_{eff}^2(x)] F = 0 \quad 2.18$$

Eqn (2.16) and (2.18) are the two one-dimensional equations to be solved to find at the beginning of the derivation of the method. Solving eqn (2.18), while taking  $x$  as a parameter, we can find  $N_{eff}(x)$ . Once  $N_{eff}(x)$  is known, solving for the eigenvalues of eqn (2.16) gives the eigenvalue of the mode. The following analogy should be noted: solving eqn(2.18) for each value of  $x$ , is like solving the wave-equation for a one-dimensional waveguide extending to infinity in the  $x$  direction, with a refractive index  $n(x,y)$  in the  $y$ -direction (depth direction) Solving eqn(2.16) is like solving the wave equation for a one-dimensional waveguide extending to infinity in the  $y$  direction, with a refractive index  $N_{eff}(x)$  in the  $x$ -direction (lateral direction) (see Fig 2.2).

Keeping this analogy in mind, it should be noted that, practically, when one wants to calculate the propagation constant of a desired mode, one must be careful in selecting the correct propagating modes of the one-dimensional waveguides in the intermediate calculations. In general, to calculate  $\beta$  for the TE mode of the two-dimensional waveguide  $a$ ), we consider the TE mode for the

slab waveguides b) in Fig 2.3 with refractive index-profile  $n(x,y)$  ( $x$  taken as a parameter), and then calculate the TM mode for the slab waveguide c) in Fig 2.3, with the effective-index profile  $N_{eff}(x)$  [6] (and reciprocally for TM modes). Indeed, if we consider the TE mode for instance, the  $e_x$  component in a TE mode of the actual two-dimensional structure is the electric field for a TE mode in the first stage computation of the EIM, but becomes the  $e_y$  component of the TM mode of the equivalent slab waveguide with an effective index  $N_{eff}(x)$  but extending to infinity in the  $y$  direction in the second stage computation.

Fig 2.2: Schematic representation of the EIM

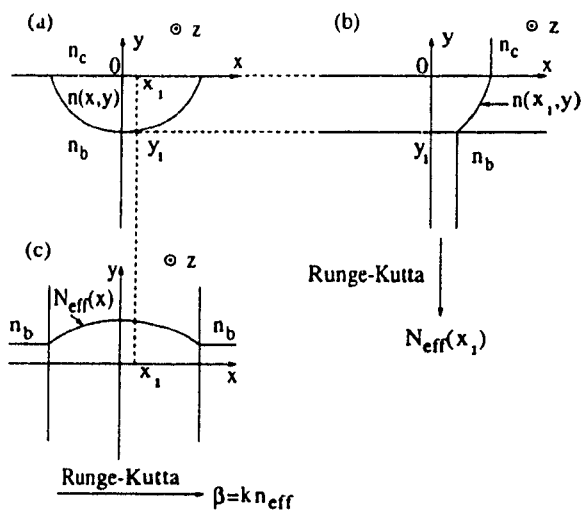
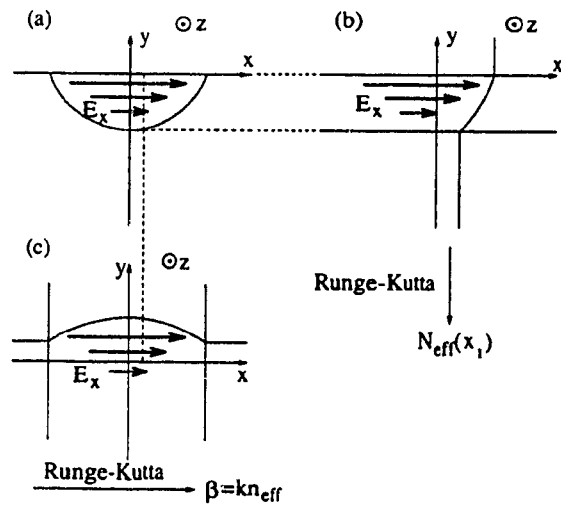


Fig 2.3: Order of the TE-TM mode calculation (example of a TE mode)



### 2.2.2 Limitations of the method

According to the assumption made in the derivation of eqn(2.16) that  $G$  varies slowly with  $x$ , the EIM method remains accurate provided  $dN_{eff}(x)/dx$  is as small as possible. The greater the aspect ratio  $r=d_x/d_y$  (long dimension/short dimension), the better this condition will be satisfied [6]. Near a cutoff, the EIM becomes less reliable:  $k_0^2 n^2(x,y) - N_{eff}^2(x)$  gets smaller over the waveguide region, and the second and third order terms are not negligible in eqn(2.17), as assumed in the derivation of the method. Outside these limits, the EIM is reliable and the first and second order

mode in a waveguide can be calculated with great precision (the error on  $\beta$  is between +0 and  $+5.10^{-5}\mu\text{m}^{-1}$ )[5].

The above considerations illustrate how the wave equation for the 2-D graded-index waveguides can be split into two 1-D wave equations under the effective-index modelling. The 1-D wave equation can be easily studied by numerical methods such as the Runge-Kutta method.

### 2.3 The Runge-Kutta method

There are various numerical methods available [8] for the analysis of waveguides with a one-dimensional arbitrary index profile (see Fig 2.1a), such as the WKB method [9], the staircase approximation [10-11], the variational method [12-13] and the Runge-Kutta method [14]. The Runge-Kutta method has been successfully applied to the study of graded-index optical fiber, earlier in [2]. In this chapter, it is applied to the study of slab waveguides such as the one shown in Fig 2.1a) with an arbitrary refractive index  $n(y)$ . The Runge-Kutta method (or equivalent transverse resonance method TRM [15]) has the advantage being more accurate than the WKB method and less complex to implement than the staircase approximation or the variational method without any loss in accuracy compared to these two methods [15].

We have from eqn(2.12) for the TE modes of our slab waveguide, with refractive index  $n(y)$ :

$$\frac{\partial e_x}{\partial y} = j\omega\mu_0 h_z \quad 2.19$$

and from Maxwell's equations (eqn (2.1)):

$$\frac{\partial h_z}{\partial y} - \frac{\partial h_y}{\partial z} = n^2(y)\epsilon_0 \frac{de_x}{dt} \quad 2.20$$

A  $(z,t)$  dependence as  $\exp(j\omega t - \beta z)$  is assumed and eqn(2.20) becomes:

$$\frac{\partial h_z}{\partial y} + j\beta h_y = j\omega\epsilon_0 n^2(y)e_x \quad 2.21$$

Using eqn (2.12) to express  $H_y$  in terms of  $E_x$ , we get:

$$\frac{\partial h_z}{\partial y} = j \frac{[k_0^2 n^2(y) - \beta^2]}{\mu_0 \omega} e_x \quad 2.22$$

Expressing the relations 2.19 and 2.22 in a matrix form, yields

$$\frac{\partial}{\partial y} \begin{bmatrix} e_x \\ h_z \end{bmatrix} = \begin{bmatrix} 0 & \mu_0 j \omega \\ \frac{j(k_0^2 n^2(y) - \beta^2)}{\mu_0 \omega} & 0 \end{bmatrix} \begin{bmatrix} e_x \\ h_z \end{bmatrix} \quad 2.23$$

In order to deal with real quantities we can set  $\hat{e}_x = j e_x$ , then rewriting eqn(2.23) we have:

$$\frac{\partial}{\partial y} \begin{bmatrix} \hat{e}_x \\ h_z \end{bmatrix} = \begin{bmatrix} 0 & -\mu_0 \omega \\ \frac{[n^2(y)k_0^2 - \beta^2]}{\mu_0 \omega} & 0 \end{bmatrix} \begin{bmatrix} \hat{e}_x \\ h_z \end{bmatrix} \quad 2.24$$

This difference equation can be approximated by  $[F_{m+1}] = [B_{m+1,m}] [F_m]$ , where  $[F_m] = [F(y_m)] = [F(-mh)] = [\hat{e}_x(-mh), h_z(-mh)]^T$  (h is the step size used ( $h=D/M$ ),  $T$  means the transposed matrix) and  $[B_{m+1,m}]$  can be computed by using a Runge-Kutta fourth order procedure [16-17] (See Appendix). By recursion, we obtain from  $y=0$  to  $y=-D$  ( $m=0$  to  $m=M$ )

$$[F_M] = \prod_{i=0}^{M-1} [B_{i+1,i}] [F_0] \quad 2.25$$

The solutions in the air and in the substrate are known to be:

In the air:  $e_x = A e^{-\delta y}$  and thus, using eqn(2.19),  $h_z = j A \delta e^{-\delta y} / \mu_0 \omega$

In the substrate:  $e_x = B e^{\gamma(y+D)}$  and thus, using eqn(2.19),  $h_z = B \gamma e^{\gamma(y+D)} / \mu_0 j \omega$

Therefore, (with also  $\hat{e}_x = j e_x$ )

$$[F_0] = \begin{bmatrix} \hat{e}_x(0) \\ h_z(0) \end{bmatrix} = \begin{bmatrix} jA \\ \frac{j\delta A}{\mu_0 \omega} \end{bmatrix} \quad 2.26$$

$$[F_M] = \begin{bmatrix} \hat{e}_x(-D) \\ h_z(-D) \end{bmatrix} = \begin{bmatrix} jB \\ \frac{-jB\gamma}{\mu_0 \omega} \end{bmatrix}$$

## Chapter 2: Methods of analysis for diffused optical waveguides

Substituting these expressions in eqn (2.22) and writing  $\Pi[B_{i,j+1}] = [\alpha]$ , we get the following system:

$$\begin{aligned} jB &= \alpha_{11}jA + \alpha_{12}\frac{\delta jA}{\mu_0\omega} \\ \frac{-jB\gamma}{\mu_0\omega} &= \alpha_{21}jA + \alpha_{22}\frac{\delta jA}{\mu_0\omega} \end{aligned} \quad 2.27$$

or

$$\begin{aligned} (\alpha_{11} + \frac{\alpha_{12}\delta}{\mu_0\omega})A - B &= 0 \\ (\alpha_{21} + \frac{\alpha_{22}\delta}{\mu_0\omega})A + \frac{\gamma B}{\mu_0\omega} &= 0 \end{aligned} \quad 2.28$$

In this system of two simultaneous linear equations, A and B have non trivial solutions if the determinant is zero, i.e.:

$$(\alpha_{11} + \frac{\alpha_{12}\delta}{\mu_0\omega})\frac{\gamma}{\mu_0\omega} + (\alpha_{21} + \frac{\alpha_{22}\delta}{\mu_0\omega}) = 0 \quad 2.29$$

This is the dispersion equation of the waveguide for TE modes (which can be solved by a classic secant method).

A similar expression can be derived for TM modes (the same relation as for the TE modes if we substitute  $\mu_0$  by  $-\omega(y)$  according to the duality principle). In this case the relation between  $h_x$  and  $e_z$  is given by:

$$\frac{\partial}{\partial y} \begin{bmatrix} H_x \\ E_z \end{bmatrix} = \begin{bmatrix} 0 & -\epsilon(y)j\omega \\ \frac{j[k_0^2 n^2(y) - \beta^2]}{-\epsilon(y)\omega} & 0 \end{bmatrix} \begin{bmatrix} H_x \\ E_z \end{bmatrix} \quad 2.30$$

The dispersion relation to be found is:

$$\left( \alpha_{11} - \frac{\alpha_{12}\delta}{\epsilon_0\omega} \right) \frac{\gamma}{-\epsilon_b\omega} + \left( \alpha_{21} - \frac{\alpha_{22}\delta}{\epsilon_0\omega} \right) = 0 \quad (2.31)$$

Using the Runge-Kutta method, the truncation error when solving for the field components is of the order of  $h^5$ . With  $h=0.1\mu\text{m}$  an error of the order of  $10^{-5} \mu\text{m}^{-1}$  is expected in the effective index. With  $h=0.005\mu\text{m}$ , the index value is expected to be correct up to the seventh digit. Numerical results show that  $h=0.1\mu\text{m}$  is an acceptable choice (error less than  $10^{-5}$ ) and indeed good agreement with the BPM was obtained (see Chapter 5). With this step-size the computations are almost instantaneous on a Sun Sparc station.

### Conclusion

The combination of the EIM and Runge-Kutta method can provide very accurate results, when one wants to study channel waveguides with arbitrary index distribution. With these techniques, under the weakly guiding conditions the analysis of glass integrated optics devices can be well performed from an engineering viewpoint.

### References

- [1] R. M. Knos and P.P. Toullos, "Integrated Circuits for the Millimeter through Optical Frequency Range", in Proceedings on Submillimeter Waves, J. Fox, Ed. (Polytechnic Press, Brooklyn, 1970), pp.497-516.
- [2] G.L. Yip and Y. H. Ahmew, "Numerical study of graded index optical fibers using vector mode analysis-An introduction", Journal of China Institute of Communications, Vol 6, pp.21-34, 1985.
- [3] G.L. Yip and Y.H. Ahmew, "Propagation characteristics of radially inhomogeneous fiber", Electron. Lett., Vol 10, pp.37-41, 1974.
- [4] K. S. Chiang, "Analysis of optical fibers by the effective-index method", App. Opt., Vol 25, pp.348-354, 1986.
- [5] G. B. Hocker and W. K. Burns, "Modes dispersion in diffused channel waveguides by the effective

## Chapter 2: Methods of analysis for diffused optical waveguides

---

index method", *App. Opt.*, Vol 16, pp.113-118, 1977.

[6] K. Van de Velde, H. Thienpont and R. Van Geen, "Extending the effective index method for arbitrarily shaped inhomogeneous optical waveguides", *IEEE J. of Lightwave Technology*, Vol 6, pp.1153-1159, 1988.

[7] J. Albert and G. L. Yip, "Wide single mode channels and directional coupler by two step ion-exchange in glass", *IEEE J. of Lightwave Technology*, Vol 6, pp.552-563, 1988.

[8] H. Ikuno, "Analysis of wave propagation in inhomogeneous dielectric slab waveguides", *IEEE Trans. Micr. Th. Tech.*, MTT 26, pp.261-267 (1977).

[9] G. B. Hocker and W.K. Burns, "Modes in diffused optical waveguides of arbitrary index profile", *IEEE J. of Quantum Electronics* QE-12, pp.270-276, 1975.

[10] M. J. Adams, "An introduction to optical waveguides", U of Southampton Ed., (Wiley New York 1980), pp.168-177.

[11] Pr J. B. Clarricoats and K.B. Chan, "Electromagnetic wave propagation along radially inhomogeneous dielectric cylinders", *Electron. Lett.*, 6, pp.694-700, 1970.

[12] H.A. Haus, W.P. Huang and N. M. Whitaker, "Optical waveguide dispersion characteristics from the scalar wave equation", *IEEE J. of Lightwave Technology*, Vol 5, pp 1748-1754, December 1987.

[13] P. K. Mishra and A. Sharma, "Analysis of single mode inhomogeneous planar waveguides", *IEEE J. of Lightwave Technology*, Vol 4, pp.205-211, 1986.

[14] A. Vigants and S.P. Schlesinger, "Surface waves on radially inhomogeneous cylinders", *IRE Trans. MTT* 10, 375 (1962).

[15] J. Y. Chen, "Design considerations of a planar cross channel optical demultiplexer", M. Eng. Thesis, Elect. Eng. Dept., pp 8-32, Mc Gill University (December 1991).

[16] A Ralston and H. S . Wilf, "Mathematical methods for digital computers- Vol 1". Wiley 11-20 (1960).

[17] S. Gill, "A process for the step by step integration of different equations in an automatic digital computing machine", *Proc. Camb. Philos. Soc.*, pp.47-49, 96 (1951).

### Appendix

The matrices B can be computed by using a Runge-Kutta fourth order procedure. Starting at  $x_0=0$  with  $D_0=1$ , the unit matrix, and  $Q_0=0$ , the null matrix, the matrix  $B_{1,0}$  can be computed employing the following sequence of operation.

$$K_1 = hA(x_0)D_0$$

$$D_1 = D_0 + (K_1 - 2Q_0)/2$$

$$Q_1 = Q_0 + 3 [ (K_1 - 2Q_0)/2 ] - K_1/2$$

$$K_2 = hA(x_0 + h/2)D_1$$

$$D_2 = D_1 + (1-(1/2)^{1/2}) (K_2 - Q_1)$$

$$Q_2 = Q_1 + 3 [ (1-(1/2)^{1/2}).(K_2 - Q_1) ] - (1-(1/2)^{1/2}).K_2$$

$$K_3 = hA(x_0 + h/2)D_2$$

$$D_3 = D_2 + ( 3 ( 1 + (1/2)^{1/2} ) ) ( K_3 - Q_2 )$$

$$Q_3 = Q_2 + 3 [ (1+(1/2)^{1/2}).(K_3 - Q_2) ] - (1+(1/2)^{1/2}).K_3$$

$$K_4 = hA(x_0 + h)D_3$$

$$D_4 = D_3 + ( K_4 - 2Q_3 ) /6$$

$$Q_4 = Q_3 + 3[ ( K_4 - 2 Q_3 )/6 ] - K_4/2$$

$$\text{and then } B_{1,0} = D_4$$

At the next step,  $Q_0$  should be set equal to  $Q_4$  and not 0 to compensate for roundoff errors. Also, one can set  $D_0$  to the previous value of  $D_4$  rather than 1, and thus obtain  $B_{2,0}$  rather than  $B_{2,1}$ . And so on for the following steps. This approach eliminates the need for a final multiplication as required in eqn(2.15).

## CHAPTER 3

# CHANNEL WAVEGUIDES BUILT BY THE ION-EXCHANGE PROCESS

Passive integrated optical components in glass (soda-lime glass in our case) are commonly fabricated by the now well established ion-exchange, and this was the technology chosen to build our widened X-branch. Prior to any actual design computation, a good understanding of this fabrication technique was necessary in order to model, with a sufficient accuracy, the refractive index profile and, therefore, the lateral effective index in the effective-index method (EIM) (See Chapter 2) of the widened X-branch. This chapter summarizes the results obtained by numerically simulating the fabrication process.

In the first section, the principle of the ion-exchange technology is presented. Then, the diffusion problem related to this fabrication technique is studied and the ion-exchange diffusion equation is derived. In Section 3, a finite-difference numerical scheme is proposed to solve this equation in the case of a single channel waveguide or two coupled channel waveguides. Indeed, theoretical considerations (See Chapter 4) show that the study of the widened X-branch can be reduced to that of these two simple structures. The results in terms of exchanged-ion concentration and refractive index profile are presented in Section 4 and 5 for the two structures. Using these data, for both cases, a new model for the effective index  $N_{eff}(x)$  in the lateral direction in the EIM, is derived, as an improvement of the more classic but rougher step-index approximation.

### 3.1 The ion-exchange technology

A typical soda-lime glass is composed of 71-75 % silicon dioxide ( $\text{SiO}_2$ ), 12-16 %, sodium oxide ( $\text{Na}_2\text{O}$ ), 5-15% calcium oxide ( $\text{CaO}$ ) and smaller amount of various oxides [1].

It was found a long time ago [2], that under certain conditions it was possible to replace some

### Chapter 3: Channel waveguides built by the ion exchange process

---

of the ions present in the glass by other ions of equal valence. Sodium ions in particular have been found to be easily displaced by ions such as  $K^+$  or  $Ag^+$ . The new ions thus introduced in the glass occupy the same sites as the ions that they replaced. Of course the properties of glass change in the regions where such exchange has taken place, and the refractive index is increased. This makes the so called "ion-exchange technology" very attractive for fabricating optical waveguides. In this thesis, we are interested in the sodium-potassium ( $Na^+ - K^+$ ) ion exchange to fabricate channel guides. Practically one way to realize this ion-exchange is to immerse completely the glass sample into a solution of the molten salt ( $KNO_3$ ) for a given diffusion time  $t_d$  (See Fig 3.1). In order to build a channel waveguide, a metallic mask blocks the diffusion process in some regions. Consequently, the diffusion problem to solve is two-dimensional (whereas for a simple slab waveguide it is one-dimensional). After  $t_d$ , the sample is withdrawn from the melt. A single-ion exchange has taken place. This is a very simple technique and the corresponding diffusion problem, that is numerically simulated in this chapter. Of course, there are alternative and more elaborate ways to carry out the  $Na^+ - K^+$  ion-exchange. For instance, one can use a two step ion-exchange with post-annealing [3-4]. In this case after the first ion-exchange, realized by total immersion, is finished, the sample is post-baked, and further thermal in-diffusion of the potassium ions can take place. Using this post-annealing technique, the resulting ion-exchanged concentration profile obtained, has smooth edges and is similar to those obtained by in-diffusion from a strip for other types of ion exchange [5-6]. In Section 3.4.1 we will compare the exchanged ion concentration profiles obtained by this post-annealing technique, to those we obtained by a single ion-exchange.

### 3.2 The ion-exchange diffusion theory

The basic theory of ion-exchange between different ionic species has been considered by Doremus and by Stewart [7-8]. These authors noted the one-to-one nature of the exchange. In a glass of mixed composition, the total ionic concentration is constant and the concentration gradients are equal but opposite (see Fig 3.2). It is, therefore, convenient to normalize the concentration profiles with respect to the total concentration. If  $c_a$  and  $c_b$  are, respectively the normalized potassium and sodium concentrations of  $K^+$  and  $Na^+$  ions exchange, we can write:

Fig 3.1: The ion exchange process to fabricate a channel waveguide

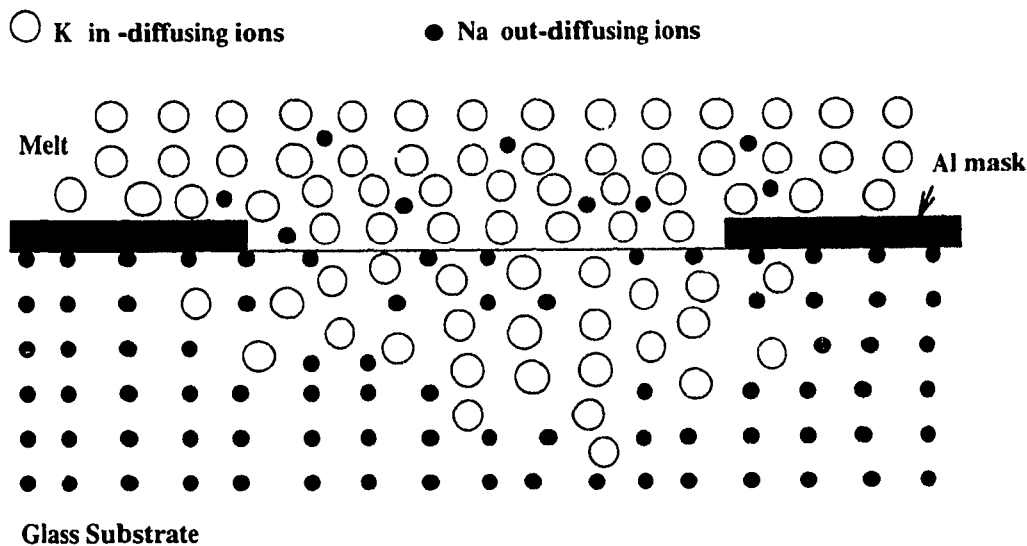
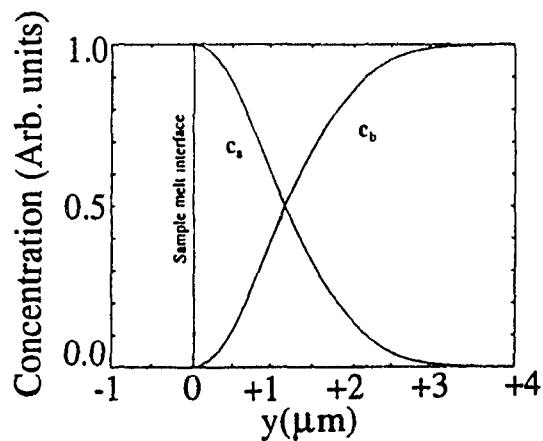


Fig 3.2: The sodium ( $c_b$ ) and potassium ( $c_a$ ) concentrations in the glass during the ion exchange



$$c_a + c_b = 1 \quad 3.1$$

Locally, however, the potassium ions have a lower mobility than the sodium ions within the glass. Their respective Fickian-type diffusion flux will differ, and one may tend to outrun the other. An electric field thus results, which has the effect of restoring neutrality by equalizing the flux of the two ion species. Therefore, the ionic flux has two components, one describing the Fickian diffusion, the other the electric drift.

$$\vec{j}_a = -D_a [\vec{\nabla}c_a - \frac{e}{k_B T} c_a \vec{E}] \quad 3.2$$

$$\vec{j}_b = -D_b [\vec{\nabla}c_b - \frac{e}{k_B T} c_b \vec{E}] \quad 3.3$$

$D_a$  and  $D_b$  are the inter-diffusion constants for the potassium and sodium, respectively.  $T$  is the temperature and  $k_B$  the Boltzmann constant. Neutrality requires that:

$$\vec{\nabla} \cdot (\vec{j}_a + \vec{j}_b) = 0 \quad 3.4$$

The Fickian diffusion constant is the same in the x and y direction as soda lime glass is an isotropic material. Expanding (3.4) using eqns(3.1), (3.2) and (3.3) to eliminate  $c_b$  yields:

$$\vec{\nabla} \cdot [\alpha \vec{\nabla}c_a + \frac{e}{k_B T} (1 - \alpha c_a) \vec{E}] = 0 \quad 3.5$$

where  $\alpha = 1 - D_a/D_b$

One possible solution for this equation is

$$\alpha \vec{\nabla}c_a + \frac{e}{k_B T} (1 - \alpha c_a) \vec{E} = \vec{0} \quad 3.6$$

which is equivalent to saying that  $j_a = -j_b$

### Chapter 3: Channel waveguides built by the ion exchange process

---

Hence, from Eq(3.2) and (3.3) we get

$$\frac{\partial c_a}{\partial t} = \frac{\partial}{\partial x} \left( \frac{D_a}{1-\alpha c_a} \frac{\partial c_a}{\partial x} \right) + \frac{\partial}{\partial y} \left( \frac{D_a}{1-\alpha c_a} \frac{\partial c_a}{\partial y} \right) \quad 3.7$$

One should notice that the assumption  $j_a = -j_b$  and hence eqn.(3.7), is valid whenever the only dielectric field present is that due to the imbalance of the Fickian flux, and  $E$  and  $\nabla c_a$  are naturally collinear. Near a conducting boundary, (like a metallic mask), tangential electric field components vanish, and the direction of  $E$  is dictated by the boundary and need bear no relation to that of  $\nabla c_a$ . Near such a boundary eqn(3.7) is not rigorously valid.

#### Normalized parameters

In the case of a uni-dimentional problem (a slab waveguide, for instance), it was observed that for the  $K^+$ - $Na^+$  exchange, the maximum concentration of exchanged ions occurring at the surface is only a fraction  $h$  (around 0.9) of the total concentration of available  $Na^+$  ions [9-10]. A classical procedure is to consider the normalized variable  $ch = c_a$  ( then  $c(y=0,t)=1$  for a uni-dimensional exchange). In eqn(3.7)  $c$  replaces  $c_a$ , with the normalized parameter  $\hat{\alpha} = h\alpha$ , and we get:

$$\frac{\partial c}{\partial t} = \frac{\partial}{\partial x} \left( \frac{D_a}{1-\hat{\alpha} c} \frac{\partial c}{\partial x} \right) + \frac{\partial}{\partial y} \left( \frac{D_a}{1-\hat{\alpha} c} \frac{\partial c}{\partial y} \right) \quad 3.8$$

It has been shown that the value of  $\hat{\alpha}$  controls the shape of the diffusion profile of the waveguide [8-9]. For  $K^+$  ion exchange  $\hat{\alpha}$  is found to be  $\hat{\alpha}=0.898$ .

A numerical solution to eqn(3.8) can be found, using a finite difference scheme [10-12].

### 3.3 Finite difference solution to the ion-exchange diffusion problem:

To standardize somewhat the numerical procedure, the following transformation is made Eqn(3.8) becomes:

$$f = \ln(1 - \hat{\alpha}c) \quad 3.9$$

$$\frac{\partial f}{\partial t} = e^{-f} D_a \left( \frac{\partial^2 f}{\partial x^2} + \frac{\partial^2 f}{\partial y^2} \right) \quad 3.10$$

To implement the finite difference method, the continuous space must be discretized into a lattice structure. In the cases we studied (single channel waveguide, coupled waveguides) an axis of symmetry could be found in the problem. For such structures a first computer time and memory saving measure consists of studying the solution in only one of the symmetric regions [12]. Then, a second measure is to consider a variable grid on which to calculate the finite differences. This new grid is obtained by mapping the semi-infinite x and y axes onto finite intervals by the following change of variables:

$$\xi = \frac{x}{x+a}, \quad \eta = \frac{y}{y+b} \quad 3.11$$

By this transformation, an evenly spaced grid in the  $(\eta, \xi)$  coordinate system corresponds to an  $(x, y)$  grid which begins very fine near  $(0, 0)$  and gradually becomes coarser away from the origin, yielding the desired high resolution in the rectangle defined by  $x=(0, a)$  and  $y=(0, b)$  and also the coverage of the region outside extending to  $\infty$  as  $x, y \rightarrow \infty$  when  $\xi, \eta \rightarrow 1$ . Eqn (3.10) then becomes:

$$\frac{\partial f}{\partial t} = D_a e^{-f} \left[ \frac{(1-\xi)^3}{a^2} \left( -2 \frac{\partial f}{\partial \xi} + (1-\xi) \frac{\partial^2 f}{\partial \xi^2} \right) + \frac{(1-\eta)^3}{b^2} \left( -2 \frac{\partial f}{\partial \eta} + (1-\eta) \frac{\partial^2 f}{\partial \eta^2} \right) \right] \quad 3.12$$

As we deal with a 3-level finite difference problem (3 variables:  $x, y, t$ ), the more efficient scheme to use, when applying the method, is the explicit scheme.

The associated finite-difference expressions, are:

$$\left( \frac{\partial f}{\partial \xi} \right)_{i,j} = \frac{f_0(i+1, j) - f_0(i-1, j)}{2\Delta \xi} \quad 3.13$$

$$\left(\frac{\partial f}{\partial \eta}\right)_{i,j} = \frac{f_0(i, j+1) - f_0(i, j-1)}{2\Delta\eta} \quad 3.14$$

$$\left(\frac{\partial^2 f}{\partial \xi^2}\right)_{i,j} = \frac{f_0(i+1, j) + f_0(i-1, j) - 2f_0(i, j)}{(\Delta\xi)^2} \quad 3.15$$

$$\left(\frac{\partial^2 f}{\partial \eta^2}\right)_{i,j} = \frac{f_0(i, j+1) + f_0(i, j-1) - 2f_0(i, j)}{(\Delta\eta)^2} \quad 3.16$$

$$\left(\frac{\partial f}{\partial t}\right)_{i,j} = \frac{f_1(i, j) - f_0(i, j)}{\Delta t} \quad 3.17$$

where  $f_0(i,j)$  is the value of  $f$  at the grid point  $i,j$  at time  $t$ , and  $f_1(i,j)$  is the value of  $f$  at the same grid point in  $t+\Delta t$ . Substituting these expressions in eqn(3.12) yields a clear recursive relation between  $f_1$  and  $f_0$ . A stability criterion for the method can be derived as

$$\Delta t < \frac{((\Delta x)^2 + (\Delta y)^2)(1 - \alpha c)}{8D_a} \quad 3.18$$

For instance, if the minimum step size for  $\Delta x$  and  $\Delta y$  is  $0.1\mu\text{m}$ , with  $D_a \approx 1.95 \times 10^{-4} \mu\text{m}^2/\text{s}$  (from slab waveguide characterization) and  $(1 - \alpha c) < 1$ , the time step size  $\Delta t$  must be less than 1 second. Using this finite difference scheme we could simulate the fabrication process of our widened X-branch.

### 3.4 Numerical results for the exchanged ion concentration:

When we carried out our simulations, we considered different diffusion times  $t_d$  (in the range 200-300 minutes), waveguide widths  $w$  (in the range  $6-12\mu\text{m}$ ) and a diffusion temperature of  $385^\circ\text{C}$ .

## Chapter 3: Channel waveguides built by the ion exchange process

---

For the diffusion constant  $D_a$  (and, therefore, the effective diffusion constant  $D_e$  defined later), we used values obtained from the planar waveguide characterization given by Yip and al. in [13] and the two following problems were taken into account:

- a) When one considers the mode propagation, the relative dimensions of the same index profiles are not exactly the same depending on the wavelength of the propagating wave exciting the guide.
- b) There is a stress-induced birefringence of the waveguides after the ion exchange ( $K^+$  and  $Na^+$  are ions with much different radii and the crystal lattice is affected when one replaces the other) [14-16].

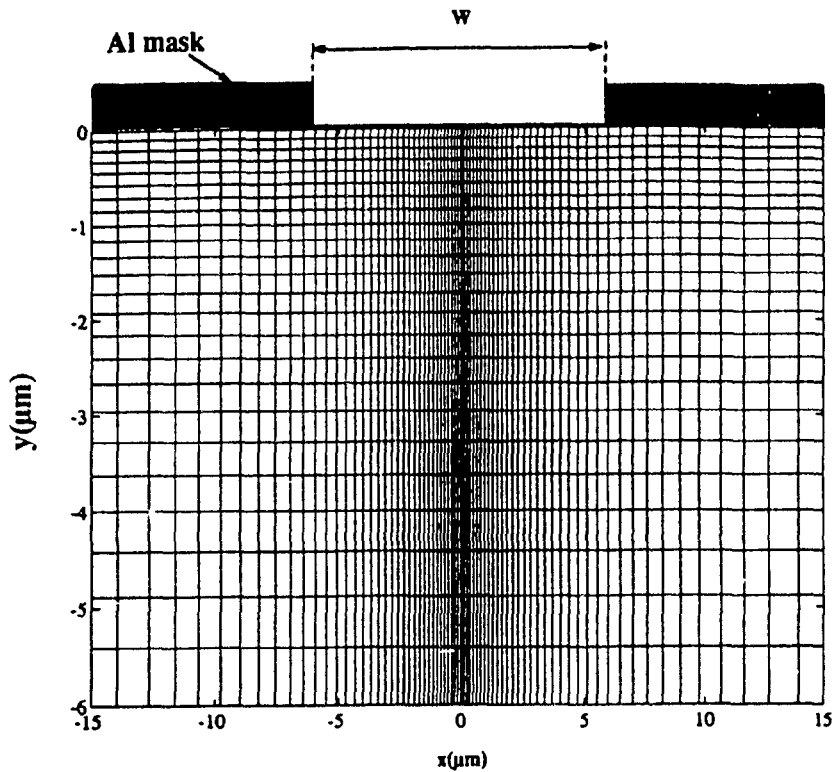
### 3.4.1 The single channel waveguide case:

This is the problem we have to deal with in the central region of our X-branch. The diffusion problem is symmetric about the center. To define the mesh, one can choose the scaling parameter  $a$  in eqn(3.11) of the order of the diffusion length. The diffusion depth is defined as  $d=(D_e t_d)^{1/2}$  where  $t_d$  is the diffusion time and  $D_e$  is the effective diffusion constant defined as  $D_e=4.\delta^2 D_a$  with  $\delta=1.17$  [9-10]. We can choose  $b=d$  i.e. With  $t_d$  in the range  $220 < t_d < 300$  min at  $385^\circ C$ , this means  $b=d=D_e t_d^{1/2} \approx (4 \times (1.17)^2 \times (1.867 \times 10^{-4}) \times 270)^{1/2} \approx 4 \mu m$ . A good value for  $a$  is  $a=w/2$  (end of the diffusion mask opening). The value of the step-size  $\Delta x(0)$  and  $\Delta y(0)$  near the origin, where the grid is more refined, can be chosen around  $0.1 \mu m$ . A typical calculation grid is shown Fig 3.3

The boundary conditions are deduced from the ion-exchange conditions:

- (a) At  $t=0$ , the sample is immersed in the molten salt of  $KNO_3$ , and the exchange starts, from  $c=0$  everywhere, except under the mask opening at the melt-glass interface.
- (b) For  $t>0$ , the glass substrate is completely immersed in an infinite reservoir of melt and the mobility of the ions in the melt is sufficient to maintain a homogeneous and constant supply of new ions, in spite of the temporary presence of the outdiffusing ions. Therefore, under the mask opening, at the interface between the melt and the glass the concentration of exchanged ions is constant:  $c=1$ .
- (c) Under the mask the field induced by the metallic mask is assumed negligible although it is not exactly true [11] and the concentration gradient is zero:  $grad(c)=0$ .
- (d) Along the symmetry wall chosen ( $x=0$ ),  $grad(c)$  is zero as well.
- (e) At  $x,y=\infty$ ,  $c$  is zero.

Fig 3.3: Calculation grid for the solution of the exchange diffusion equations



Typical numerical results for the concentration profile  $c(x,y)$  are given Table 3.1: for different values of  $x$  ( $x=0.000\mu\text{m}$ ,  $x=1.0256\mu\text{m}$ ,  $x=2.105\mu\text{m}$ , ...,  $x=226.66\mu\text{m}$ ,  $x=+\infty$ ), the values of  $c(x,y)$  are given for the 41 values of  $y$  listed at the beginning of the Table ( $y=0.000\mu\text{m}$ ,  $y=0.0769\mu\text{m}$ ,  $y=0.1579\mu\text{m}$ , ...,  $y=117.0\mu\text{m}$ ,  $y=+\infty$ )).

A 3-D plot of  $c(x,y)$  is given Fig 3.4. The concentration contours obtained are of the form shown in Fig 3.5a,b. This solution for the concentration profile  $c(x,y)$ , obtained by numerical simulation of a single ion-exchange, is compared in Fig 3.6 to the concentration profile to be found when

### Chapter 3: Channel waveguides built by the ion exchange process

---

fabrication techniques using post-baking such as the one mentioned in Section 3.2 [3-4] are used. When the post baking technique is used, the diffusion problem is an analog to the diffusion from a thin film [5-6], and from diffusion theory [17] the concentration profile  $c(x,y)$  can be derived analytically to be [18-19]:

$$c(x,y) = c(0,0)\exp\left(-\frac{y^2}{d^2}\right)\left[\operatorname{erf}\left(\frac{w/2+x}{d}\right) + \operatorname{erf}\left(\frac{w/2-x}{d}\right)\right] \quad 3.19$$

where  $d$  is the diffusion length ( $d=(D_e t_d)^{1/2}$ ),  $t_d$  is the total time of the two-step diffusion process, and  $w$  the waveguide width.

Qualitatively, the solutions obtained for  $c(x,y)$  for a single ion-exchange and a double ion-exchange with post-annealing techniques are alike, but when the total immersion technique is used the diffusion effects are less serious and the edges of the diffusion profile are sharper. When light propagation is considered, we can expect structures built by the total immersion technique to yield more scattering loss [20]. This point is considered again in Chapter 7.

**Table 3.1: A typical output of the program used to calculate the concentration profile of exchanged ions  
( $T=385^\circ\text{C}$ ,  $t_d=270\text{min}$ ,  $w=6.0\mu\text{m}$ ,  $D_a=1.867 \times 10^{-4}\mu\text{m}^2/\text{s}$ )**

$y=\{$						
0.0000	0.0769	0.1579	0.2432	0.3333	0.4286	0.5294
0.6364	0.7500	0.8710	1.0000	1.1379	1.2857	1.4444
1.6154	1.8000	2.0000	2.2174	2.4545	2.7143	3.0000
3.3158	3.6667	4.0588	4.5000	5.0000	5.5714	6.2308
7.0000	7.9091	9.0000	10.3333	12.0000	14.1429	17.0000
21.0000	27.0000	37.0000	57.0000	117.0000		Inf]

### Chapter 3: Channel waveguides built by the ion exchange process

$c(x, y)$

$i=$  1  $x=$  0.000000000000000e+00  
 1.000000000000000e+01 1.000000000000000e+01 1.000000000000000e+01  
 1.000000000000000e+01 1.000000000000000e+01 1.000000000000000e+01 1.000000000000000e+01  
 1.000000000000000e+01 1.000000000000000e+01 1.000000000000000e+01 1.000000000000000e+01  
 1.000000000000000e+01 1.000000000000000e+01 1.000000000000000e+01 8.42443587090548e+00  
 6.84075480966445e+00 5.03570154066918e+00 3.09409313042314e+00 1.38807115503594e+00  
 3.82615881146207e-01 5.50375772258648e-02 3.53819026536351e-03 8.51062833878838e-05  
 6.01650432023855e-07 8.28618292516031e-10 8.40703403947780e-14 0.000000000000000e+00

$i=$  2  $x=$  1.02564102564103e-01  
 9.92708216492933e+00 9.92703910927531e+00 9.92688679764484e+00  
 9.92659353627627e+00 9.92611475101662e+00 9.92538571996882e+00 9.92430874155594e+00  
 9.92272900515419e+00 9.92038544550274e+00 9.91679955402450e+00 9.91098448814597e+00  
 9.90050112926736e+00 9.87710715464447e+00 9.78944510211292e+00 8.40048014706547e+00  
 6.83209060373163e+00 5.03064150703210e+00 3.09114338419362e+00 1.38674933728885e+00  
 3.82256165616571e-01 5.49872952902995e-02 3.53504294083062e-03 8.50319991120486e-05  
 6.01132111176094e-07 8.27911112593886e-10 8.40703403947780e-14 0.000000000000000e+00

$i=$  3  $x=$  2.10526315789474e-01  
 9.84535276288997e+00 9.84525894877279e+00 9.84492706335596e+00  
 9.84428799627441e+00 9.84324449418351e+00 9.84165525405591e+00 9.83930682835277e+00  
 9.83586080102672e+00 9.83074630690320e+00 9.82291760922016e+00 9.81022509829710e+00  
 9.78742153695350e+00 9.73763071658885e+00 9.57472367660257e+00 8.33763786747875e+00  
 6.80391964643981e+00 5.01389804271991e+00 3.08136233513314e+00 1.38236486172081e+00  
 3.81062886233917e-01 5.48204808828056e-02 3.52460065474135e-03 8.47855245056719e-05  
 5.99412276804667e-07 8.25564561034044e-10 8.40703403947780e-14 0.000000000000000e+00

$i=$  4  $x=$  3.24324324324324e-01  
 9.75343396207704e+00 9.75328073899599e+00 9.75273867928181e+00  
 9.75169490224640e+00 9.74999056823143e+00 9.74739493425607e+00 9.74355960086457e+00  
 9.73793271667261e+00 9.72958523723790e+00 9.71682248055444e+00 9.69619364088602e+00  
 9.65946788809693e+00 9.58177189068129e+00 9.35610737897324e+00 8.24180188233434e+00  
 6.75456628876901e+00 4.98384124475037e+00 3.06372890872303e+00 1.37445452586396e+00  
 3.7890576028248e-01 5.45193983030234e-02 3.50575026926583e-03 8.43405407861637e-05  
 5.96307080674744e-07 8.21327663143854e-10 8.40703403947780e-14 0.000000000000000e+00

$i=$  5  $x=$  4.44444444444444e-01  
 9.64969793234348e+00 9.64947571377292e+00 9.64868959122451e+00  
 9.64717597901950e+00 9.64470486258190e+00 9.64094246791298e+00 9.63538565796005e+00  
 9.62723956620678e+00 9.61517187689557e+00 9.59677110971398e+00 9.56719912029637e+00  
 9.51526407645491e+00 9.40935409404039e+00 9.13259233813528e+00 8.11676576684764e+00  
 6.68266779611503e+00 4.93879261123001e+00 3.03713661571023e+00 1.36251140890148e+00  
 3.75657432695244e-01 5.40645237732076e-02 3.47726340650973e-03 8.36679580765184e-05  
 5.91613112125085e-07 8.14922245002893e-10 8.28340118595607e-14 0.000000000000000e+00

....

$i=$  10  $x=$  1.16129032258065e+00  
 8.87243866345102e+00 8.87170480915842e+00 8.86911076593429e+00  
 8.86412583992995e+00 8.85601557002112e+00 8.84373579178321e+00 8.82575483498469e+00  
 8.79974189191965e+00 8.76199314425494e+00 8.70631433751925e+00 8.62170841000835e+00  
 8.48729273920364e+00 8.26066413349021e+00 7.85261742700282e+00 7.09854723130539e+00  
 5.94311485524262e+00 4.42810707957640e+00 2.72657635149619e+00 1.22214591138920e+00  
 3.37354149355805e-01 4.86935351792221e-02 3.14018087724114e-03 7.56981460081159e-05  
 5.35941019354098e-07 7.38909057672126e-10 7.54160406482567e-14 0.000000000000000e+00

### Chapter 3: Channel waveguides built by the ion exchange process

---

....

```
i=      15      x=  2.15384615384615e+00
7.30464221553419e+00 7.30319252092336e+00 7.29807671929720e+00
7.28828524091031e+00 7.27246622423019e+00 7.24877504635801e+00 7.21464125349517e+00
7.16639870097545e+00 7.09868439898567e+00 7.00344046616318e+00 6.86823529347821e+00
6.67346102615762e+00 6.38793817465399e+00 5.96351191428752e+00 5.33481339686098e+00
4.44467232084278e+00 3.29466825905046e+00 2.01371886959379e+00 8.98032153530049e-01
2.48548199010188e-01 3.61450287271856e-02 2.34718966167567e-03 5.68618374348236e-05
4.03960622685674e-07 5.58323493847073e-10 5.68711126199969e-14 0.00000000000000e+00
```

....

```
i=      20      x=  3.61904761904762e+00
4.21150509865806e+00 4.20985484746430e+00 4.20404204870771e+00
4.19296477928842e+00 4.17520172889695e+00 4.14890164432660e+00 4.11162821854945e+00
4.06014113199123e+00 3.99008678968702e+00 3.89556595634526e+00 3.76854850865162e+00
3.59814472388668e+00 3.36989329635521e+00 3.06567664970913e+00 2.66599379886630e+00
2.15837856552746e+00 1.55692159580567e+00 9.30743152784679e-01 4.11188353428539e-01
1.14664171019905e-01 1.69423297613565e-02 1.11625782401390e-03 2.73290942079044e-05
1.95623856139020e-07 2.71887189822318e-10 2.84355563099984e-14 0.00000000000000e+00
```

....

```
i=      25      x=  6.00000000000000e+00
6.53893690111207e-01 6.53506562964708e-01 6.52144707139258e-01
6.49557209748103e-01 6.45429170157713e-01 6.39364465631740e-01 6.30864067864329e-01
6.19299343940900e-01 6.03880531396166e-01 5.83622612485160e-01 5.57315641709115e-01
5.23517261825001e-01 4.80607442642784e-01 4.26988717136272e-01 3.61588394185912e-01
2.84905247584593e-01 2.00801585008904e-01 1.18578618888748e-01 5.27047146831854e-02
1.50504407201900e-02 2.29041261010514e-03 1.54778278566730e-04 3.86279014590155e-06
2.80508133424959e-08 3.94203353454044e-11 3.70898560565197e-15 0.00000000000000e+00
```

....

```
i=      30      x=  1.05454545454545e+01
1.69454752025939e-03 1.69348271853450e-03 1.68973791334596e-03
1.68262733016332e-03 1.67129541102605e-03 1.65467413603000e-03 1.63143104319849e-03
1.59990796364351e-03 1.55805316553928e-03 1.50335563896317e-03 1.43280301748490e-03
1.34291038630773e-03 1.22991677025649e-03 1.09033495057685e-03 9.22179119437875e-04
7.27341116306120e-04 5.15475411217438e-04 3.08485468957377e-04 1.40444365822777e-04
4.14404286894290e-05 6.52458399730716e-06 4.54172882178276e-07 1.16113960812099e-08
8.59730500104775e-11 1.22396524986515e-13 0.00000000000000e+00 0.00000000000000e+00
```

....

```
i=      35      x=  2.26666666666667e+01
1.90682658972173e-10 1.90562735104257e-10 1.90142383402283e-10
1.89343715168533e-10 1.88071533105794e-10 1.86204677017616e-10 1.83596023808308e-10
1.80058887869051e-10 1.75363312092296e-10 1.69231122557618e-10 1.61324801574903e-10
1.51258614641163e-10 1.38614682711496e-10 1.23003562297307e-10 1.04203950590792e-10
8.24124238290516e-11 5.86761522814142e-11 3.53837226779198e-11 1.63034643939108e-11
4.88967935678451e-12 7.83832291327783e-13 5.56347840847796e-14 1.23632853521732e-15
0.00000000000000e+00 0.00000000000000e+00 0.00000000000000e+00 0.00000000000000e+00
```

....

i=	41	x=	Infinity	
0.00000000000000e+00	0.00000000000000e+00	0.00000000000000e+00	0.00000000000000e+00	
0.00000000000000e+00	0.00000000000000e+00	0.00000000000000e+00	0.00000000000000e+00	0.00000000000000e+00
0.00000000000000e+00	0.00000000000000e+00	0.00000000000000e+00	0.00000000000000e+00	0.00000000000000e+00
0.00000000000000e+00	0.00000000000000e+00	0.00000000000000e+00	0.00000000000000e+00	0.00000000000000e+00
0.00000000000000e+00	0.00000000000000e+00	0.00000000000000e+00	0.00000000000000e+00	0.00000000000000e+00
0.00000000000000e+00	0.00000000000000e+00	0.00000000000000e+00	0.00000000000000e+00	0.00000000000000e+00
0.00000000000000e+00	0.00000000000000e+00	0.00000000000000e+00	0.00000000000000e+00	0.00000000000000e+00
0.00000000000000e+00	0.00000000000000e+00	0.00000000000000e+00	0.00000000000000e+00	0.00000000000000e+00

Fig 3.4: A 3-D plot of the concentration profile resulting from a single ion exchange  
 (T=385°C, t<sub>d</sub>=270min, w=6.0μm, D<sub>a</sub>=1.867.10<sup>-4</sup> μm<sup>2</sup>/s)

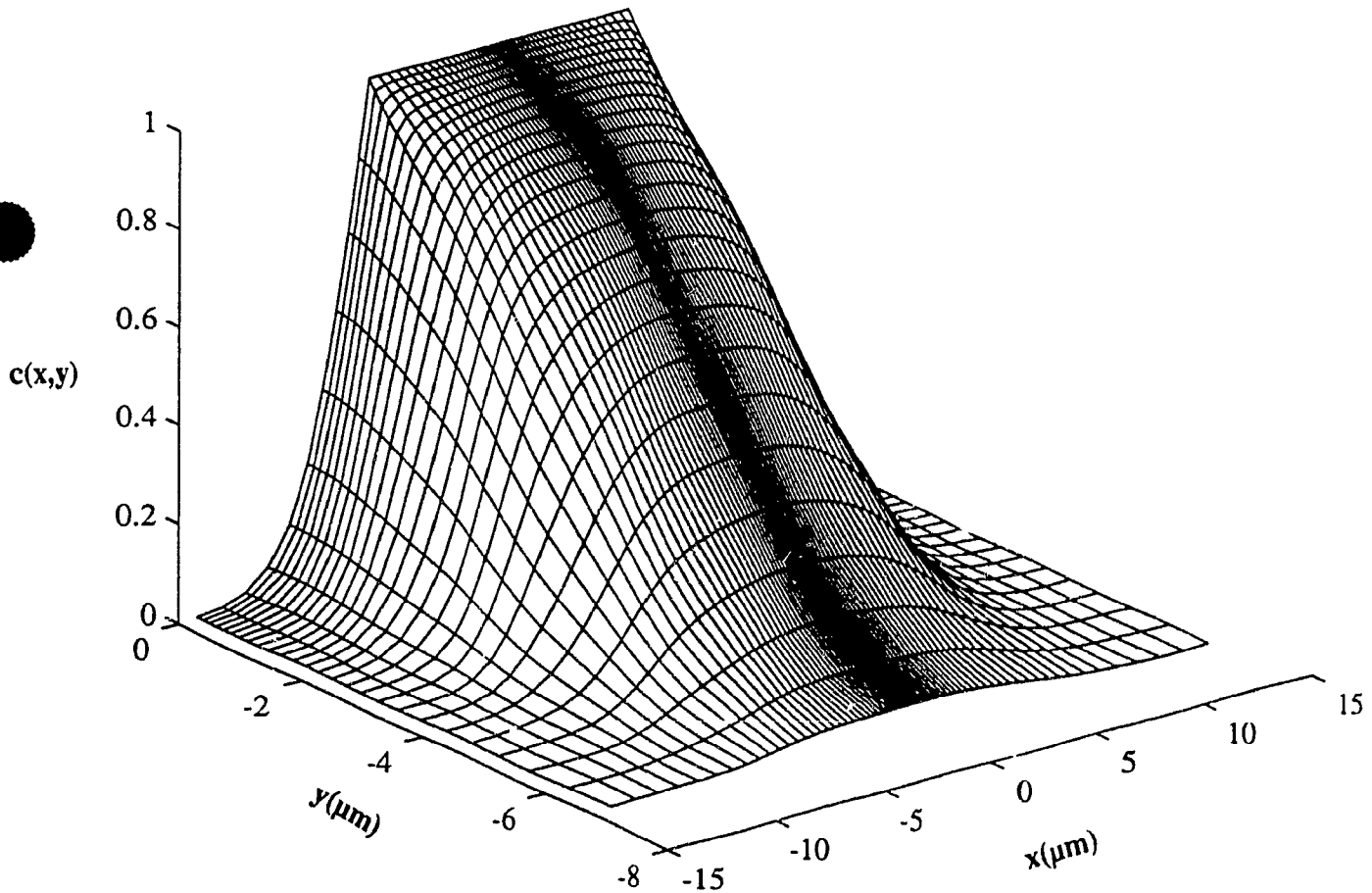
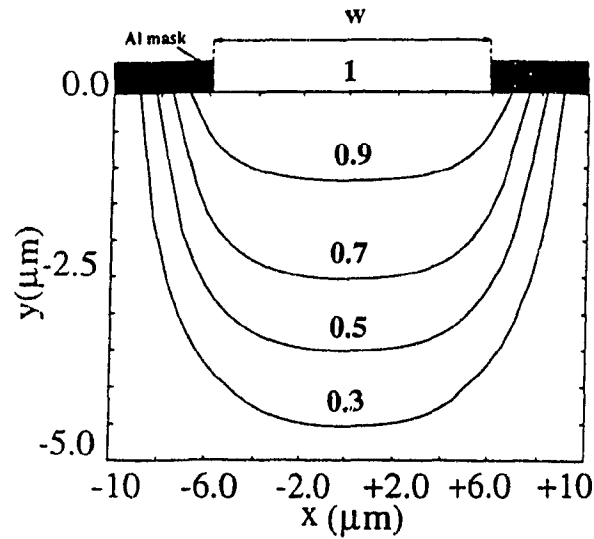
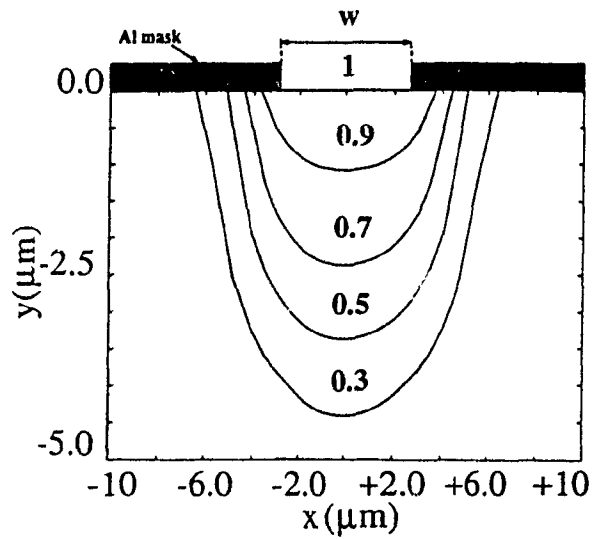


Fig 3.5a,b: Constant concentration contours produced by a single ion exchange  
( $T=385^{\circ}\text{C}$ ,  $t_d=270\text{min}$ ,  $D_a=1.867\times 10^{-4}\mu\text{m}^2/\text{s}$ ). (Single waveguide case)



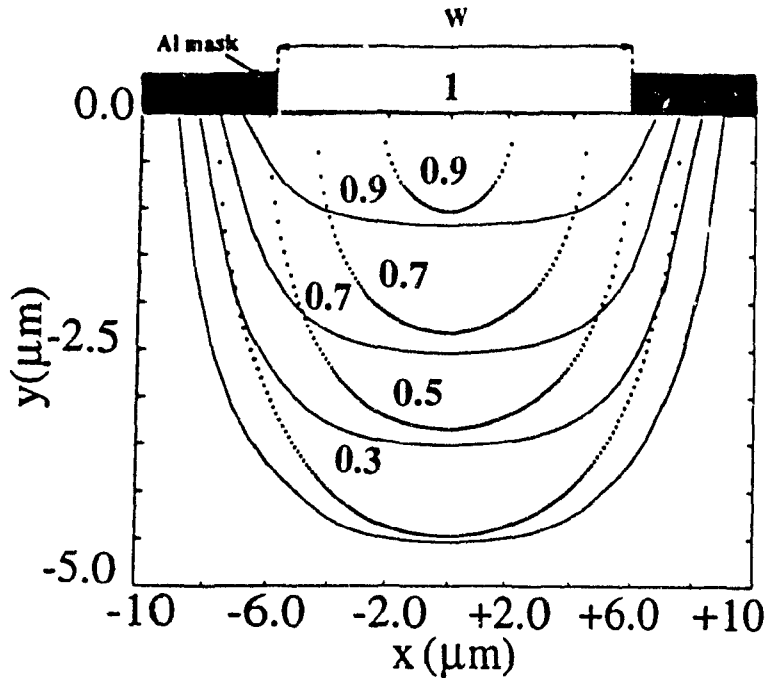
3.5a)  $w=12.0\mu\text{m}$



3.5b)  $w=6.0\mu\text{m}$

Fig 3.6: Compared constant concentrations contours produced by an ion-exchange ( $T=385^{\circ}\text{C}, t_d=270\text{min}, D_a=1.867\times 10^{-4}\mu\text{m}^2/\text{s}, w=12\mu\text{m}$ ). (Single waveguide case).

— Single exchange (total immersion technique) ... With post-annealing



### 3.4.2 Coupled waveguides configuration:

For a more accurate design of the X-branch, the tapered region of the device, involving two channel guides, need also to be studied. The diffusion problem for two coupled waveguides was also simulated for different waveguide spacing  $s$  and  $p$  ( $p$  is the distance between the centres of the two waveguides, and  $s=p-w$ ). The axis of symmetry is at the mid-point between the two waveguides. The same values for  $b, \Delta x(0), \Delta y(0)$  as in the previous case and the same type of boundary conditions

should be chosen. In the lateral direction  $a=(w+s)/2$  is a good choice. Results for the concentration contours obtained are given in Fig 3.7. As the spacing goes from large values ( $s \gg w$ ) to zero, the concentration of the exchanged ions in the middle  $c(0,y)$  increases gradually. As expected, the change in this value becomes noticeable when  $s$  is of the order of the diffusion depth  $s \approx d$ . For  $t_d=270$  min,  $d=(D_c t_d)^{1/2} \approx 4 \mu\text{m}$

### 3.5 Numerical results for the index profile

The refractive index profile can be deduced from the concentration profile as:  $n(x,y)=n_b+\Delta n_s c(x,y)$  [10] if  $n_b$  is the substrate index and  $\Delta n_s=n(0,0)-n_b$  is the surface index change induced by the ion exchange which can be determined from the experiment characterizations ( $n(0,0)=n_s$  is the surface index). Once again, using for  $\Delta n_s$  the data given in [13] allows to take into account birifringence problems as discussed Section 3.4. Even in the simple case of a single waveguide, the expression for  $n(x,y)$  is not rigorously separable. A classical approximation, in order to simplify the problem is the step-index approximation. Under this approximation, side diffusion effects are neglected. For a single channel waveguide of width  $w$ , we can write for the concentration profile and, therefore, the refractive index profile:

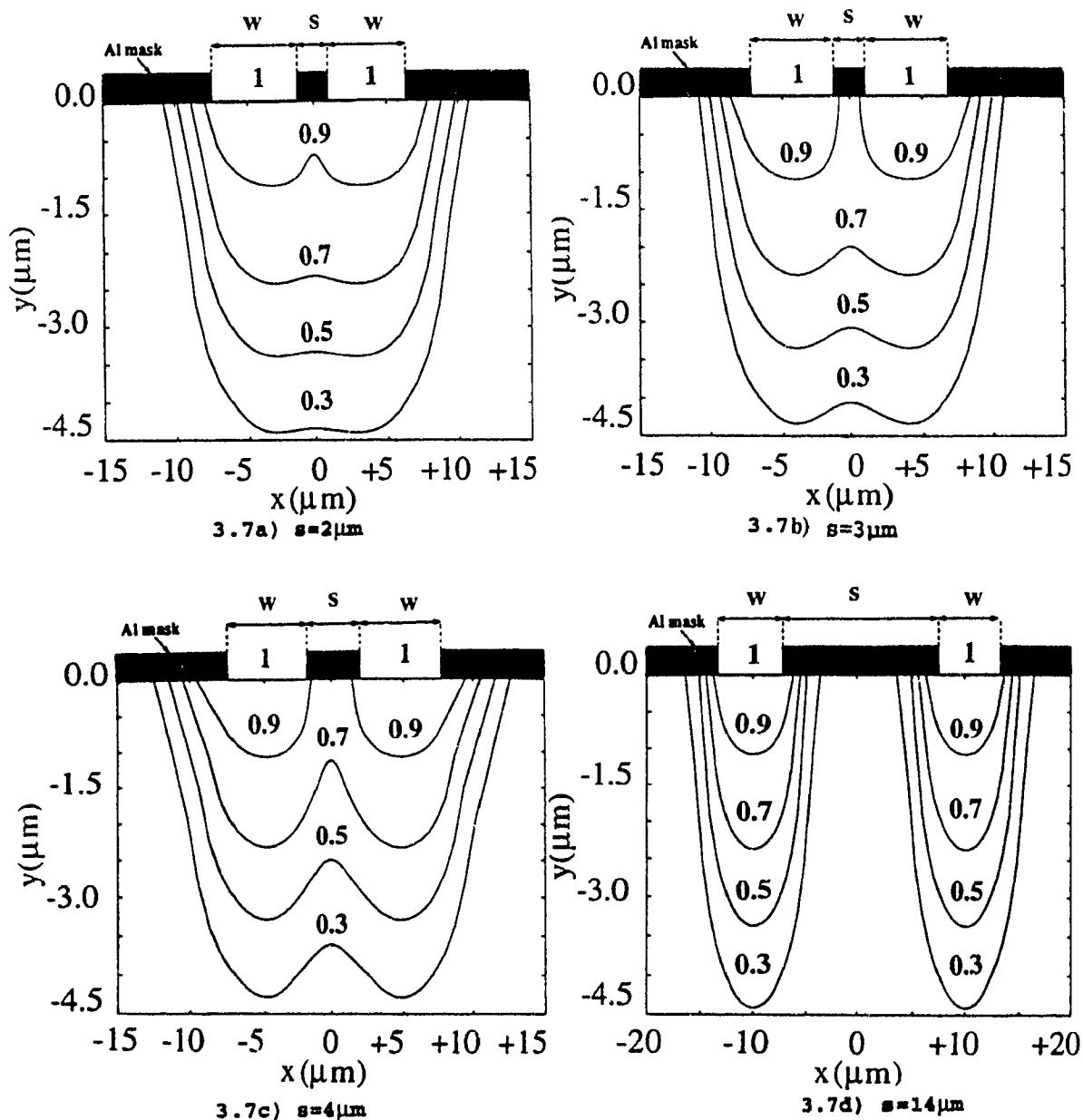
$$\begin{aligned} \text{If } -w/2 < x < w/2, \quad c(x,y) \approx c(0,y), \quad \text{then } n(x,y) \approx n(0,y) \\ \text{If } x > w/2, \quad x < -w/2, \quad c(x,y) \approx 0, \quad \text{then } n(x,y) \approx n_b \end{aligned} \quad 3.20$$

In the case of two coupled waveguides, of width  $w$ , separated by a distance  $s$ , we get

$$\begin{aligned} \text{if } w < |x| < w + \frac{s}{2}, \quad c(x,y) \approx c(\pm \frac{w+s}{2}, y) \quad \text{then } n(x,y) \approx n(\pm \frac{w+s}{2}, y) \\ \text{if } |x| > w + \frac{s}{2}, \quad |x| < \frac{s}{2}, \quad c(x,y) \approx 0 \quad \text{then } n(x,y) \approx n_b \end{aligned} \quad 3.21$$

The step-index approximation is very often used. Indeed it allows a very simple expression for the effective index in the lateral direction, to be found (See Chapter 2). For modelling, it is a very effective tool. However, its accuracy must be examined when accurate design parameters are to be calculated. This point is elaborated on in the following section.

Fig 3.7a,b,c,d): Constant concentration contours resulting from a single exchange  
 ( $T=385^{\circ}\text{C}$ ,  $t_d=270\text{min}$ ,  $D_a=1.867\times 10^{-4}\mu\text{m}^2/\text{s}$ ). (Directional coupler configuration)



### 3.6 Effective index modelling (EIM)

The EIM was presented Chapter 2 as a powerful tool to calculate the propagation constants of the guided modes in two-dimensional waveguiding structures of an arbitrary refractive index profile  $n(x,y)$ . This method requires to calculate an effective index in the lateral direction  $N_{eff}(x)$  which can be determined by finding the eigenvalues of the following equation (with  $x$  as a parameter):

$$\frac{\partial^2 F}{\partial y^2} + k_o^2(n^2(x,y) - N_{eff}^2(x))F = 0 \quad 3.22$$

Once  $N_{eff}(x)$  is known, the propagation constants of the guided modes can be found by solving for the eigenvalues of the following equation

$$\frac{\partial^2 G}{\partial x^2} + k_o^2(N_{eff}^2(x) - \beta^2)G = 0 \quad 3.23$$

In the next Sections (3.6.1 to 3.6.2), expressions for  $N_{eff}(x)$ , in the case of a single waveguide and for two coupled waveguides are derived, using for  $n(x,y)$  the data obtained in the previous Sections by numerically solving the diffusion equation.

#### 3.6.1 The single waveguide case

##### 3.6.1.1 The solution by step-index approximation:

Under the classic step index approximation, the side diffusion effects are neglected, as mentioned in the previous Section, and one gets a simplified expression for  $n(x,y)$  (see eqns(3.20) and (3.21)). Solving (3.22) with this expression for  $n(x,y)$ ,  $N_{eff}(x)$  for a channel waveguide of width  $w$ , can be found as:

$$\begin{aligned} N_{eff}(x) &\approx N(0) \approx N_p \quad \text{if } -w/2 < x < w/2 \\ N_{eff}(x) &\approx n_b \quad \text{if } x < -w/2, x > w/2 \end{aligned} \quad 3.24$$

where  $N_p$  is the effective index of a planar waveguide exchanged for the same amount of time

## Chapter 3: Channel waveguides built by the ion exchange process

---

(and  $n_b$  is the substrate index). This expression has the advantage to be very simple.

### 3.6.1.2 The semi analytical solution

If we consider the exact solution of the diffusion equation as derived by the finite-difference scheme, then  $n(x,y)$  is known only at the discrete points of the computation mesh used to solve the diffusion equation. At each grid-step  $x$ , if we want to solve equation (3.22) and find  $N_{eff}(x)$ , we have to interpolate  $n(x,y)$  along the grid steps  $y$  by a polynomial fit. For the interpolation of the index profile, we considered the  $n$ th first significant points, (usually  $n=10$ ), and used a  $n$ th order linear interpolation which proved to be a very accurate approximation (see Fig 3.8).  $N_{eff}(x)$  was calculated for different diffusion times, mask widths, for both wavelength 1.31 and 1.55  $\mu\text{m}$  and for both TE and TM modes, using the Runge-Kutta method described in the previous chapter. Like Albert and Yip [20], from these calculations we tried to find a fit for the effective index-profile. Indeed, it is the only practical way to run the extensive numerical simulations needed for the design of our widened X-branch. We found (using the least square method) that the following formula was a good approximation to the lateral effective index profile of channel waveguide of width  $w$  (See Fig 3.9, in the example of TM modes):

$$N_{eff}(x) = n_b + \left(\frac{N_p - n_b}{2}\right) \left[ \operatorname{erf}\left(\frac{x + \frac{w}{2}}{h}\right) - \operatorname{erf}\left(\frac{x - \frac{w}{2}}{h}\right) \right] \quad 3.25$$

where:  $n_b$  is the substrate index,

$N_p$  is the effective index of a planar guide exchanged for the amount of time  $t_d$

$h=0.7(D_e t_d)^{1/2}$  is a fitting parameter (in Albert's case he found  $h=(D_e t_d)^{1/2}$ , as he used a different fabrication process)

A very important point with this erf model is that it can be completely determined from measurements on planar waveguides (ie  $N_p$  and  $D_e$ ) as discussed in [21].

The exact numerical solution of eqn(3.22) for  $N_{eff}(x)$ , the erf fit and the solution derived under the step-index approximation are compared in Fig 3.9 in the example of TM modes. The erf fit is very good for the middle region of the waveguide. At the very edge, the agreement is not so close, but this small region is of less importance when computing the propagation constants. The

### Chapter 3: Channel waveguides built by the ion exchange process

errors in  $\beta$  are of the order of  $8 \times 10^{-5}$ . Overall, the erf fit chosen is still a good approximation. The step-index model looks like a much poorer model, especially for narrow waveguides. For any value of the channel width, the step-index model predicts that  $N_{\text{eff}}(x=0) = N_p$ , which is not the case. The erf fit model gives a good fit for  $N_{\text{eff}}(x)$  for  $x=0$ , and predicts  $N_{\text{eff}}(0) = N_p \text{erf}(w/2h) = N_p \text{erf}(w/(1.4 \times d))$ . For  $w/4d \gg 1$  one can say that  $N_{\text{eff}}(0) \approx N_p$  with a very good approximation. For narrower waveguide this is not the case and the effective index in the middle is significantly less than the one obtained for a slab waveguide exchanged for the same time. In Table 3.2a,b,c,d) effective index ( $n_{\text{eff}} = \beta/k$ ) of the first and second order mode for some typical waveguides, are calculated by the EIM, using the erf and step index model for the lateral effective index  $N_{\text{eff}}(x)$ . They are compared with the exact results obtained by considering the numerical solution. The erf model can be seen to give closer results (the errors on  $\beta$  for this model are of the order of  $8 \times 10^{-5}$ ).

#### 3.6.1.3 Dispersion curves

Using eqns(3.24) or (3.25) (step-index model or 'erf fit') we can run extensive effective index computations ( $n_{\text{eff}} = \beta/k_0$ ), using the EIM, and plot the dispersion curves for waveguides, built by a single  $K^+$ - $Na^+$  ion-exchange.

Four normalized parameters ( $V'$ ,  $b'$ ,  $b_0$ ,  $V_0$ ) were introduced for side diffused waveguides, by Hocker and Burns. They are defined by:

$$\begin{aligned}
 b' &= \frac{\left(\left(\frac{\beta}{k_0}\right)^2 - n_b^2\right)}{(N_p^2 - n_b^2)} \\
 b_0 &= \frac{N_p^2 - n_b^2}{(n_s^2 - n_b^2)} \\
 V' &= k_0 w \sqrt{(N_p^2 - n_b^2)} = V_0 b_0^{\frac{1}{2}} \frac{w}{d} \\
 V_0 &= k_0 d \sqrt{(n_s^2 - n_b^2)}
 \end{aligned} \tag{3.26}$$

Theory shows that the dispersion characteristics of any channel waveguide can be deduced if three of the four parameters are given [22-23]. One notes that  $V_0$  and  $b_0$  are the usual normalized parameters

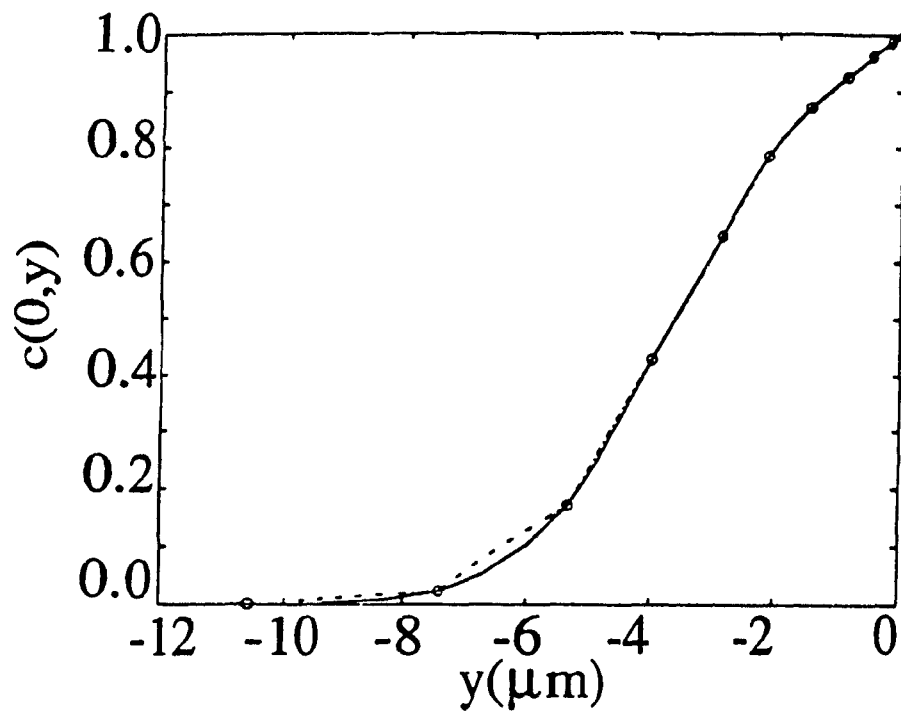
### Chapter 3: Channel waveguides built by the ion exchange process

---

used for slab waveguides [24]. (only two universal parameters are needed in this case). The dispersion curves  $V'$  vs  $b'$  for various  $b_0$  for channel waveguides built by a single  $K^+$ - $Na^+$  ion-exchange, are plotted Fig 3.10. For  $K^+$ - $Na^+$  ion exchanged waveguides  $n_p \approx n_s$  (weakly guiding case). Under this approximation, the curves  $V', b'$  are roughly the same for both polarizations. Yet, channel waveguides are still polarization dependent since for the same diffusion time  $V'(t_d)$  is different for the TE and TM polarization ( $N_p$  is different [9]). When the step-index model is used the curves  $V'$  vs  $b'$  have the same shape for all  $b_0$ . This is not the case when the erf fit model is used. for a given value of  $b'$ , the value of  $V'$  is a function of  $b_0$ . It should be noted that, as  $b_0$  gets smaller ( $b_0 \approx 0.1$ ), the curves  $V'$  vs  $b'$  obtained for the different values of  $b_0$ , using the erf fit model (side-diffused waveguides) are getting closer to the single curve  $V'$  vs  $b'$  for a guide with no side-diffusion (step-index model). This is expected. Indeed,  $b_0$  is an increasing function of  $N_p$  and therefore of  $t_d$ . A smaller  $b_0$  means a smaller  $t_d$ . The side-diffusion effects are limited for smaller diffusion times, and taking them into account does not make much difference, in the EIM, when calculating the propagation constants. However, in this thesis, we are looking for single or dual mode operation of the waveguides. The corresponding diffusion time range is between 200-300 min for TE modes, 250-450 min for TM modes (See Chapter 4), which gives for both polarizations  $b_0 \approx 0.3$ . For this value of  $b_0$ , we can see from Fig 3.10, that taking into account the side-diffusion effects definitely makes a difference when calculating the propagation constants of the mode. This point is verified in Chapter 4.

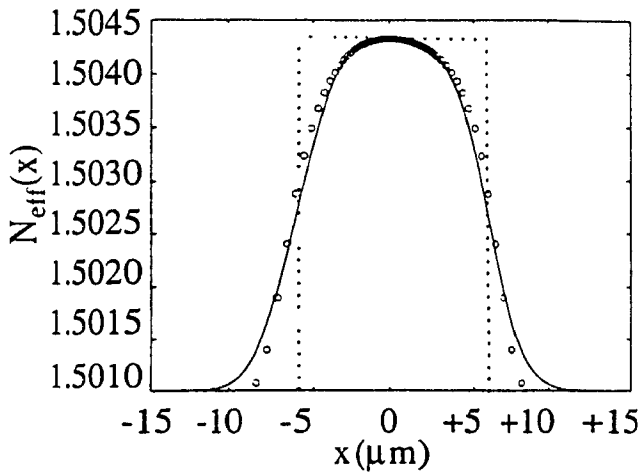
Fig 3.8: Justification for using a linear interpolation between the discrete values of  $n(x,y)$  (in this example  $x=0$ )

○—○ Numerical solution    — Linear interpolation

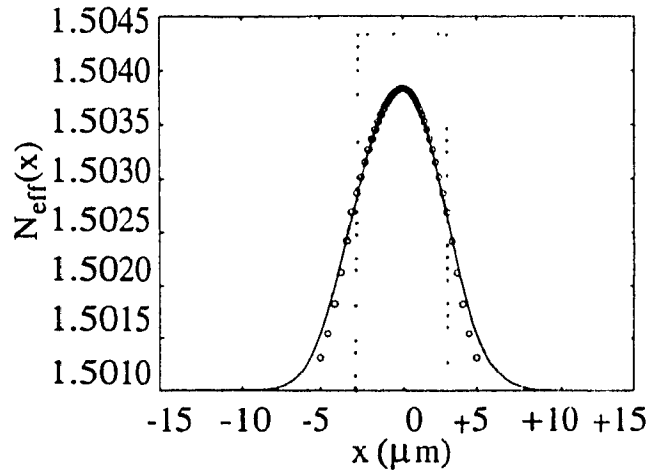


Chapter 3: Channel waveguides built by the ion exchange process

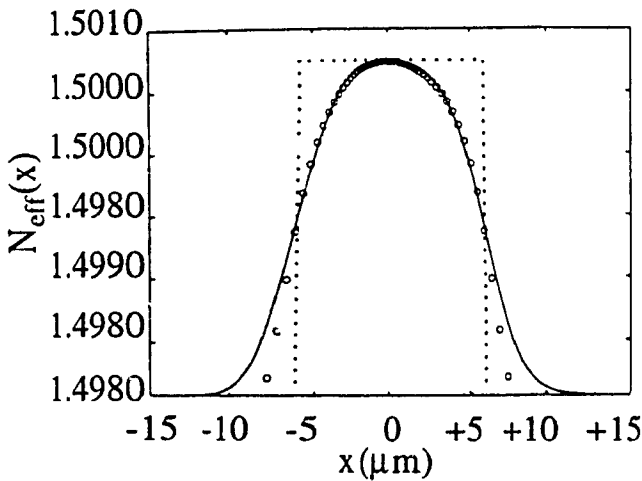
Fig 3.9 a,b,c,d): Discrete values of the local effective index  $N_{\text{eff}}(x)$  along with erf fit and step-index model. (Ion-exchange parameters:  $T=385^\circ\text{C}$ ,  $t_d=270\text{min}$ ). (single waveguide case, TM modes).  $\circ\circ\circ$  Numerical solution — Erf fit ... Step-index model



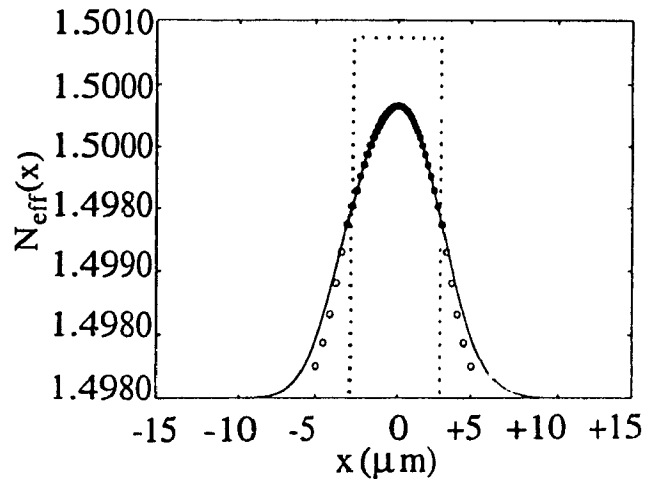
3.9a)  $\lambda=1.31\mu\text{m}$ ,  $w=12.0\mu\text{m}$



3.9b)  $\lambda=1.31\mu\text{m}$ ,  $w=6.0\mu\text{m}$



3.9c)  $\lambda=1.55\mu\text{m}$ ,  $w=12.0\mu\text{m}$



3.9d)  $\lambda=1.55\mu\text{m}$ ,  $w=6.0\mu\text{m}$

**Table 3.2a,b,c,d: Calculated effective index  $n_{\text{eff}}=\beta/k$   
(Single waveguide configuration, TM modes)**

	Numerical solution	'erf fit'		step-index model	
		$n_{\text{eff}}$	error ( $\times 10^{-5}$ )	$n_{\text{eff}}$	error ( $\times 10^{-5}$ )
1 <sup>st</sup> order mode	1.503608	1.503666	+5.8	1.503800	+19.2
2 <sup>nd</sup> order mode	1.502075	1.502148	+7.3	1.502309	+23.4

Tab 3.2a)  $w=12.0\mu\text{m}, t_d=270\text{min}, \lambda=1.31\mu\text{m}, \text{TM modes}$

	Numerical solution	'erf fit'		step-index model	
		$n_{\text{eff}}$	error ( $\times 10^{-5}$ )	$n_{\text{eff}}$	error ( $\times 10^{-5}$ )
1 <sup>st</sup> order mode	1.499946	1.499955	+4.9	1.500110	+16.4
2 <sup>nd</sup> order mode	1.498351	1.498441	+9.0	1.498486	+13.5

Tab 3.2b)  $w=12.0\mu\text{m}, t_d=270\text{min}, \lambda=1.55\mu\text{m}, \text{TM modes}$

### Chapter 3: Channel waveguides built by the ion exchange process

---

	Numerical solution	'erf fit'		step-index model	
		$n_{\text{eff}}$	error ( $\times 10^{-5}$ )	$n_{\text{eff}}$	error ( $\times 10^{-5}$ )
1 <sup>st</sup> order mode	1.502705	1.502611	-9.4	1.503043	+43.2

Tab 3.2c)  $w=6.0\mu\text{m}, t_s=270\text{min}, \lambda=1.31\mu\text{m}$ , TM modes

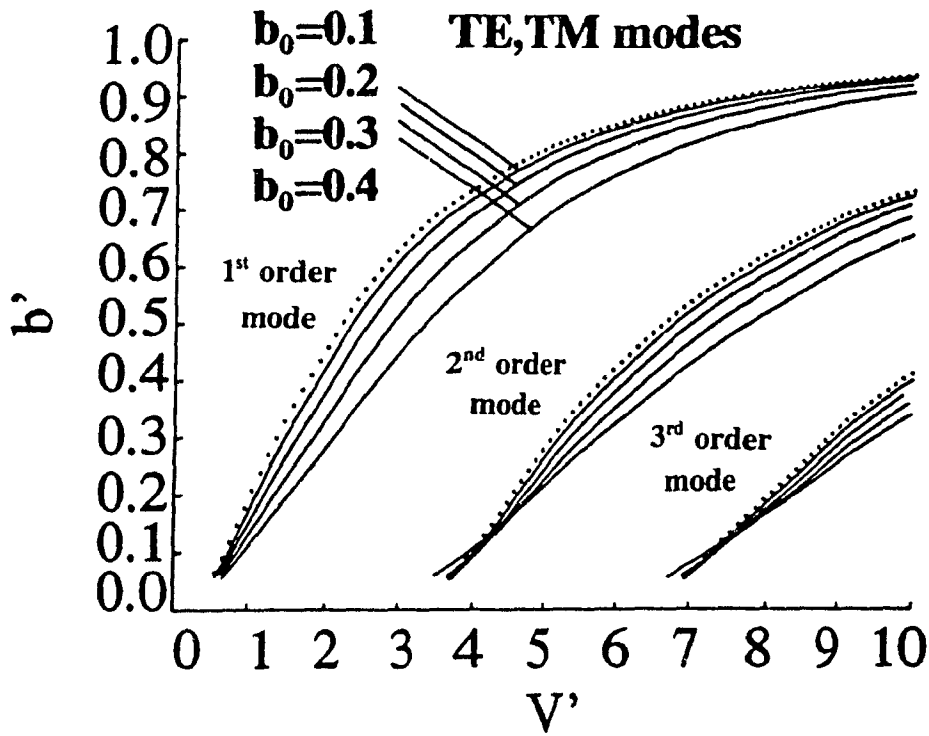
	Numerical solution	'erf fit'		step-index model	
		$n_{\text{eff}}$	error ( $\times 10^{-5}$ )	$n_{\text{eff}}$	error ( $\times 10^{-5}$ )
1 <sup>st</sup> order mode	1.499008	1.499107	+9.9	1.499361	+35.2

Tab 3.2d)  $w=6.0\mu\text{m}, t_s=270\text{min}, \lambda=1.55\mu\text{m}$ , TM modes

Fig 3.10: Normalized dispersion curve  $V'$  vs  $b'$  (normalized parameters)

(as  $n_s \approx n_b$ , the curves  $V'$  vs  $b'$  are the same for both polarizations)

— Side diffused model . . . Step index model



### 3.6.2 Coupled waveguides

#### 3.6.2.1: The solution by the step-index approximation

Under the step-index approximation the lateral effective index in the case of two coupled waveguides of width  $w$ , separated by a distance  $s$ , can be found to be (using eqn(3.21) for  $n(x,y)$  to solve eqn(3.22)):

$$\begin{aligned} \text{if } \frac{s}{2} < |x| < w + \frac{s}{2}, \quad N_{\text{eff}}(x) &= N_p \\ \text{if } |x| > w + \frac{s}{2}, \quad |x| < \frac{s}{2}, \quad N_{\text{eff}}(x) &= n_b \end{aligned} \quad 3.27$$

#### 3.6.2.2 semi analytical solution

In the case of two coupled waveguides, we found it difficult to derive a general fit to the numerical solution obtained for  $N_{\text{eff}}(x)$ , when solving eqn(3.22), using the exact expression for  $n(x,y)$ . For large waveguide separations  $s \gg d$  (where  $d$  is the diffusion depth defined previously in Section 3.4.1, and for our simulations we had  $d \approx 4\mu\text{m}$ ), adding the effective-index profile of the separate single waveguides to find the effective index of the whole structure is a good approximation [20] (See Fig 3.11a)), in the example of TM modes), and one gets

$$N_{\text{eff}}(x) = N(x+s/2) + N(x-s/2) - n_b \quad 3.28$$

where  $N(x)$  is the effective-index profile of a single waveguide as given by eqn(3.25). However, when the spacing between the two waveguides is of the order of the diffusion depth  $s \approx d$  ( $\approx 4\mu\text{m}$ ), this is not quite true anymore (see Fig 3.11b),c),d)). As  $s \rightarrow 0$ , eqn(3.8) is valid again (See Fig 3.11e)). Even so, for the design of our widened X-branch, when we needed to study the problem of two coupled waveguides in the tapered regions (See Chapter 4), we assumed that the effective index was given by eq(3.28) for any value of  $s$ . In spite of its limitations we can expect this model to be better than the step index model, since it is obtained by taking into account the side-diffusion effects.

### 3.7 Conclusion

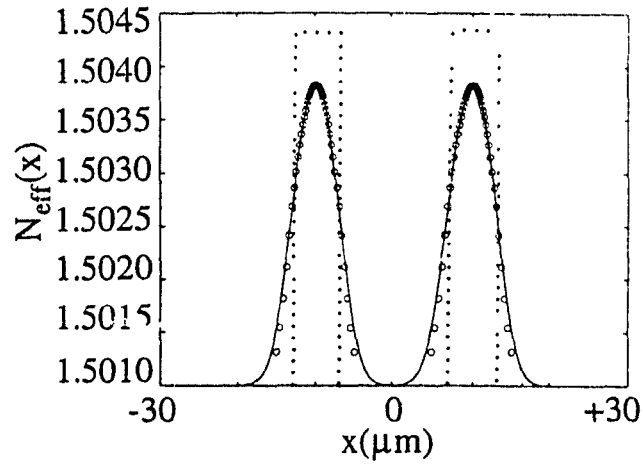
In this chapter the single  $K^+$ - $Na^+$  ion-exchange process, which we used in the experimental part of our work to fabricate our widened X-branch demultiplexer, was simulated by use of a finite-difference method. A practical analytical model for the lateral effective-index profile in the EIM, of the widened X-branch for the tapered and central regions, was deduced from these computations. This model is more sophisticated than the simple step-index approximation, and yet in an analytical form that allows us to perform the numerical simulations needed for the design of a widened X-branch demultiplexer.

Physically, it is expected to be closer to the true solution for the effective index. It should be noted that we neglected the charge effects due to the presence of metallic-mask, when simulating the diffusion process for the channel waveguide. In the case of silver ion exchange this would be questionable [24], and we could expect the side diffusion effects to be reduced. But for potassium ion-exchange, recent experimental characterization of the refractive index profile tend to prove that this assumption is correct [25].

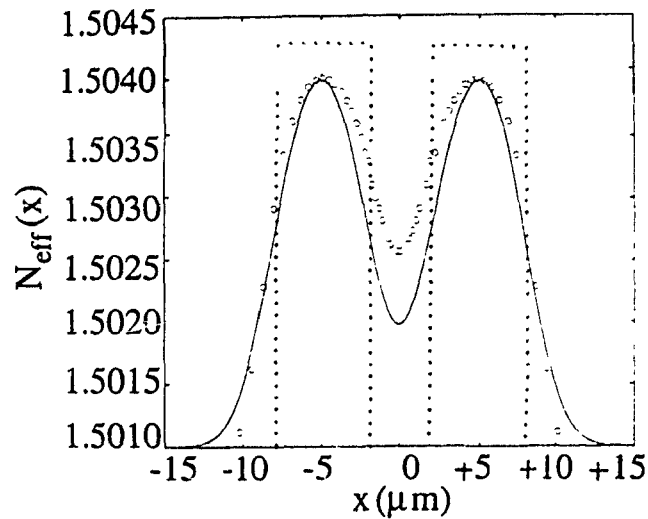
Fig 3.11a,b,c,d,e: Discrete values of the local effective index  $N_{\text{eff}}(x)$  along with erf fit and step-index model.(Directional coupler configuration)

(Ion exchange parameter:  $T=385^\circ\text{C}, t_i=270\text{min}, w=6.0\mu\text{m}$ )

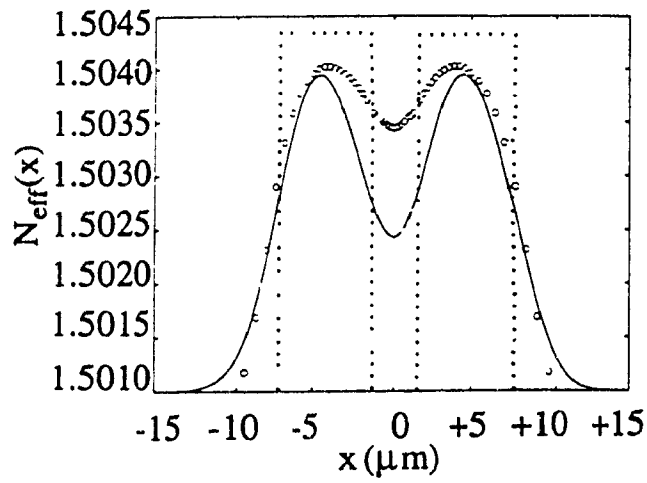
○○○ Numerical solution — Erf fit ... Step index model



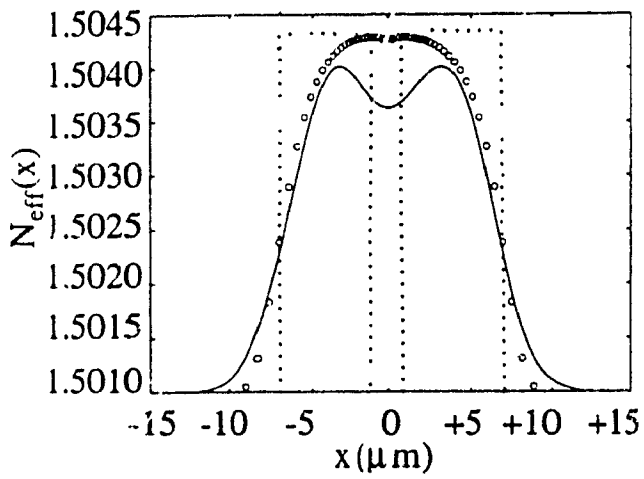
3.11a)  $s=20\mu\text{m}$



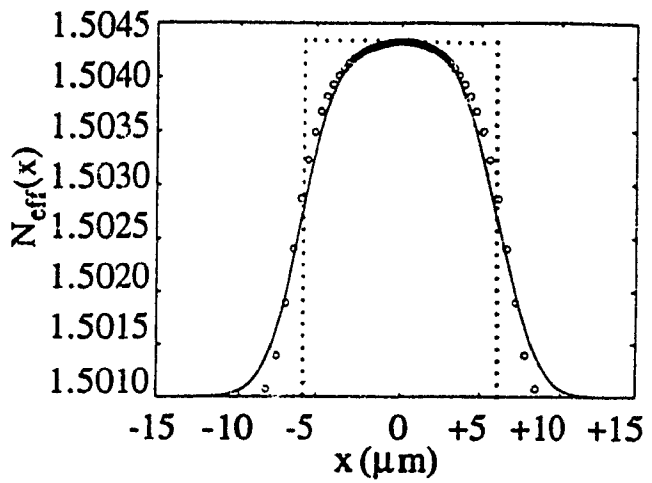
3.11b)  $s=4\mu\text{m}$



3.11c)  $s = 3 \mu\text{m}$



3.11d)  $s = 2 \mu\text{m}$



3.11e)  $s = 0 \mu\text{m}$

### Chapter 3: Channel waveguides built by the ion exchange process

---

#### References:

- [1] R. H. Doremus, "Glass Science" (Wiley, New York 1973).
- [2] Shulzen G, "Versuche uber die Diffusion von Silber in Glass", Ann. Physik 40, pp 335-367 (1913).
- [3] H. Zhenguang, R. Srivastava, R. V. Ramaswamy, "Low-loss small mode passive waveguides and near adiabatic tapers in BK7 glass", IEEE J. of Lighthwave Technology, Vol 7, n°10, pp 1590-1595, 1989.
- [4] H. C. Cheng, H. Zhenguang, A. Miliou, R. Srivastava and R. V. Ramaswamy, "Fiber compatible K<sup>+</sup>-Na<sup>+</sup> ion exchanged channel waveguides: Fabrication and characterization", IEEE J. of Quantum Electronics, Vol 25, n°8 , pp 1889-1897, 1989.
- [5] S. Honkanen and A. Tevonen, "Experimental Analysis of Ag<sup>+</sup>-Na<sup>+</sup> exchange with Ag film ion sources for planar optical waveguide fabrication", J. of Appl. Phys., Vol 63, n°1, pp 634-639, 1988.
- [6] W. K. Burns, P. H. Klein and E. J. West, "Ti diffusion in Ti:LiNbO<sub>3</sub> planar and channel optical waveguides", J. Appl. Physics, Vol 50, n°10, pp 6714-6720, 1979.
- [7] R. H. Doremus, "Ion exchange in glasses", in Ion Exchange Vol 2, J. A. Mrinsky, Ed (Dekker, New York, 1969).
- [8] G. Stewart, C. A. Millar, P. J. R. Laybourn, C. D. Wilkinson and R. M. De la Rue, "Fabrication of ion-exchanged optical waveguides from dilute silver nitrate melts", IEEE J. of Quantum Electronics, Vol 13, n°2 pp 930-934, 1977
- [9] G. L. Yip and J. Albert, "Characterization of planar optical waveguides by K<sup>+</sup> ion-exchange in glass", Opt. Lett., Vol 10, n°3, pp 151-154, 1985
- [10] J. Albert and G. L. Yip, "Refractive-index profiles of planar waveguides made by ion-exchange in glass", App. Opt., Vol 24, n°11, pp 3692-3693, 1985.
- [11] H. C. Cheng and R. V. Ramaswamy, "Simulation of tapered transitions in ion-exchanged channel waveguides", App. Opt., Vol 29, n°3 March 1990.
- [12] J. Albert, "Characterization and design of planar optical waveguides and directional couplers by two-step K<sup>+</sup>-Na<sup>+</sup> ion exchange in glass", PhD Thesis, Mc Gill Univ., El. Eng. Dept., pp 11-43, 1987.

### Chapter 3: Channel waveguides built by the ion exchange process

---

- [13] G. L. Yip, K. Kishioka, F. Xiang, J. Y. Chen, "Characterization of planar optical waveguides by K<sup>+</sup>-Na<sup>+</sup> ion exchange in glass at 1.152  $\mu\text{m}$  and 1.523  $\mu\text{m}$ ", SPIE Proc., Vol 1583, pp 40-44, Boston 1991
- [14] S. S. Kistler, "Stresses in glass produced by nonuniform exchange of monovalent ions", J. of Am. Ceram. Soc., Vol 45, pp 59-68, (1962)
- [15] J. Albert and G. L. Yip, "Stress induced index change for K<sup>+</sup>-Na<sup>+</sup> ion exchange in glass", Electron. Lett., Vol 23, n°14, pp737-738, 1987
- [16] C. B. Shand, "Glass Engineering Handbook", (Mc Graw Hill New York 1958)
- [17] P. G. Shewmon, "Diffusion in Solids", pp 7-12, (Mc Graw Hill, New York, 1963).
- [18] G. B. Hocker and W. K. Burns, "Mode dispersion in diffused channel waveguides by the effective index method", App. Opt., Vol 16, n°1, pp 113-118, 1977.
- [19] D. P. Kennedy and D. C. Murley, "Calculation of impurity atom diffusion through a narrow diffusion mask opening.", IBM Journal, Vol 10, pp 6-12, 1966
- [20] R.G. Walker, C.D. Wilkinson and J.A.H Wilkinson, "Integrated optical waveguiding structures made by silver ion-exchange in glass", App. Opt., Vol 22, n°6, pp 1923-1928, 1983.
- [21] J. Albert and G. L. Yip, "Wide single mode channels and directional coupler by two-step ion exchange in glass ", IEEE J. of Lightwave Technology, Vol 6, n°4, pp 552-563, 1988.
- [22] G. B. Hocker and W. K. Burns, "Modes in diffused optical waveguides of arbitrary index profile", IEEE J. of Quantum Electronics, Vol 12, n°6, pp 270-276, 1975
- [23] H. Kogelnik and V. Ramaswamy, "Scaling rule for thin film optical waveguides", App. Optics., Vol 13, n°6, pp 1857-1862, 1974.
- [24] A. Sharma, E. Sharma, J. C. Goyal, A. K. Ghatak, "Variational analysis of directional couplers with graded index profile", Optics Communications, Vol 34, n°7, pp 39-42, 1980.
- [25] R.A. Betts, F. Lui and T.W. Whitbread, "Nondestructive two-dimensional refractive-index profiling of integrated optical waveguides by an interferometric method", App. Opt., Vol 30, n°10, pp 4384-4389, 1991.

## CHAPTER 4

# DESIGNS OF A WIDENED X-BRANCH DEMULTIPLEXER

### 4.1 Introduction

Since first proposed as a TIR device in 1978 [1], the X-branch waveguides, either symmetric or asymmetric have been extensively studied [2-3]. In single-mode integrated optics, the X-branch has become a competitive structure with the directional coupler in many device designs. Most of these devices offer important advantages such as a low insertion loss, high extinction ratio, smaller device dimension, bidirectionality. Therefore, it has led to the possibility of more truly integrated optical circuits [4-5].

The widened X-branch offers the additional advantage of a simpler fabrication process as there is only one step involved in the ion exchange. However, in the commonest two-mode interference region, the requirements on the design parameters are tight [6] when one wants to achieve wavelength demultiplexing, especially in a glass substrate, which allows little possibilities of electrooptic tuning. Therefore, much care is needed in the design effort.

In this chapter, the widened X-branch waveguide structure to be designed will be used in a single-mode dual-channel integrated optical multi/demultiplexer at wavelengths  $1.31\mu\text{m}$  and  $1.55\mu\text{m}$ , to be fabricated by  $\text{K}^+$  ion exchange in a soda lime glass substrate [7]. The theoretical background of the device will be introduced in Section 4.2. The conditions for demultiplexing will be investigated in 4.3 using a reduced parameter  $R$  [8]. The dispersion equation for studying the X-branch will be solved in 4.4. The effective-index method will be applied and two cases will be considered for the shapes of the refractive index in the lateral direction, the step-index, and side-diffused, using the theory developed previously (See Chapters 2 and 3). The sensitivities of the device to the design parameter variations will be discussed in 4.5.

## 4.2 The device operation principle

The single-mode input and output waveguides are coupled adiabatically to the two-mode waveguide of length  $L$  by the tapered directional couplers of length  $l_1$  (see Fig 4.1). The two input and output waveguides of the tapered regions are identical. They have the same width  $w$ . The width of the waveguide in the central region ( $-L/2 < z < L/2$ ) is  $w+w=2w$ . In this Chapter, the radiation modes are not taken into account. The waveguide system is treated as one structure where only two normal modes propagate [9]: one symmetric  $\psi_s$ , one antisymmetric  $\psi_a$  as sketched Fig 2.

The total field of the structure is:

$$\psi(x,y,z) = \alpha_s \psi_s(x,y,z) + \alpha_a \psi_a(x,y,z) \quad 4.1$$

where  $\alpha_s$  is the relative excitation amplitude of the symmetric mode (even mode), and  $\alpha_a$  is that of the anti-symmetric mode (odd mode) ( $\alpha_s^2 + \alpha_a^2 = 1$ ).

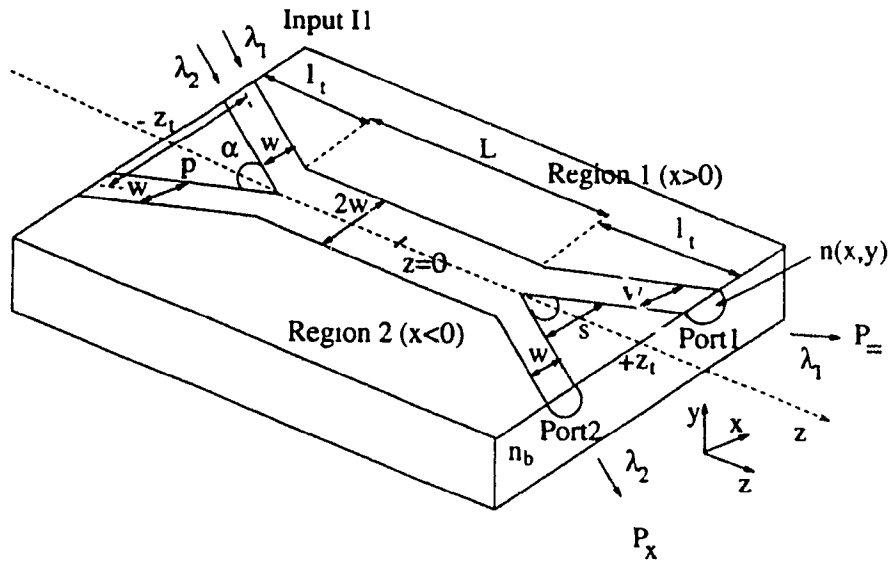
In the tapered regions ( $z < -L/2$  or  $z > L/2$ ), the symmetric and anti-symmetric modes can be viewed as two different combinations of the fundamental modes of the two input waveguides taken separately [9] (See Fig 4.2). In these regions, we can write:

$$\begin{aligned} \psi_s(x,y,z) &= ( a_1(x,y) + a_2(x,y) ) e^{-j\beta_s z} \\ \psi_a(x,y,z) &= ( a_1(x,y) - a_2(x,y) ) e^{-j\beta_a z} \end{aligned} \quad 4.2$$

here  $a_1(x,y)=a(x-p/2,y)$ ,  $a_2(x,y)=a(x+p/2,y)$ , and  $a(x,y)$  is the first-order mode of a single waveguide of width  $w$  centered at  $x=0$ . It should be noted that, in the tapered regions,  $\beta_s$  and  $\beta_a$ , the propagation constants of the symmetric and antisymmetric modes, depend on the spacing  $s$  between the two input waveguide [9] and, therefore, on  $z$ .

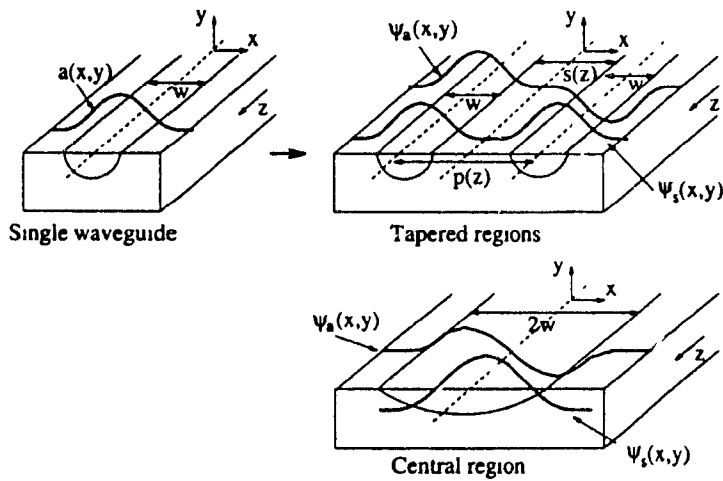
In the central region,  $\psi_s$  is the first-order mode of the waveguide (even mode), and  $\psi_a$  the second-order mode (odd),  $\beta_s$  and  $\beta_a$  are constant, equal to the propagation constants of the first and second order mode of the waveguide with a width  $2w$ .

Fig 4.1: Widened X-branch (Perspective view)



1a) Perspective view

Fig 4.2: The symmetric and antisymmetric modes in the central and tapered regions



## Chapter 4: Designs of a widened X-branch demultiplexer

According to the orthogonality principle,  $\psi_s$  and  $\psi_a$  do not exchange energy along the device.

$$\iint \psi_s(x,y,z) \psi_a^*(x,y,z) dx dy = 0 \quad 4.3$$

(\* = the complex conjugate) However, the propagation constants  $\beta_s(z)$  and  $\beta_a(z)$  of the two modes  $\psi_s$  and  $\psi_a$  are different. Therefore, the two modes accumulate a relative phase difference  $\phi = \int (\beta_s - \beta_a) dz$  along the whole structure length. Combining eqns (4.1) with (4.2), the total output field can be written as

$$\begin{aligned} \psi(x,y,z_{output}=z_1) &= \alpha_a \psi_a(x,y,z_1) + \alpha_s \psi_s(x,y,z_1) \\ &= [a_1(x,y)(\alpha_s + \alpha_a e^{j\phi}) + a_2(x,y)(\alpha_s - \alpha_a e^{j\phi})] e^{-j \int \beta dz} \end{aligned} \quad 4.4$$

$a_2(x,y) \approx 0$  if  $x > 0$ ,  $a_1(x,y) \approx 0$  if  $x < 0$  and the fields in region 1 and 2 are almost exactly:

$$\begin{aligned} \psi(x,y,z_{output}=z_1) &= a_1(x,y)(\alpha_s + \alpha_a e^{j\phi}) e^{-j \int \beta_s(z) dz} \quad \text{if } x > 0 \\ \psi(x,y,z_{output}=z_1) &= a_2(x,y)(\alpha_s - \alpha_a e^{j\phi}) e^{-j \int \beta_s(z) dz} \quad \text{if } x < 0 \end{aligned} \quad 4.5$$

The power in each output port 1 and 2 can be calculated as:

$$\begin{aligned} \text{Branch 1 (} x > 0 \text{): } P_x &= \int_{-\infty}^{+\infty} \int_{-\infty}^{+\infty} \psi(x,y,z_{output}) \cdot \psi^*(x,y,z_{output}) dx dy \\ \text{Branch 2 (} x < 0 \text{): } P_x &= \int_{-\infty}^{+\infty} \int_{-\infty}^{+\infty} \psi(x,y,z_{output}) \cdot \psi^*(x,y,z_{output}) dx dy \end{aligned} \quad 4.6$$

$\int a_{1,2}(x,y) \cdot a_{1,2}^*(x,y) dx dy = 1$  (normal modes) and the power in each output port 1 and 2 is [10]:

$$\begin{aligned} \text{Branch 1 (} x > 0 \text{): } P_x &= P_{inp} \cdot [2\alpha_s \alpha_a \cos^2(\phi/2) + (\alpha_s - \alpha_a)^2] \\ \text{Branch 2 (} x < 0 \text{): } P_x &= P_{inp} \cdot [2\alpha_s \alpha_a \sin^2(\phi/2) + (\alpha_s - \alpha_a)^2] \end{aligned} \quad 4.7$$

$P_{inp}$  = input power

## Chapter 4: Designs of a widened X-branch demultiplexer

If we assume that the symmetric and anti-symmetric modes are excited with the same amplitude at the input of the device ( $\alpha_s = \alpha_a = (1/2)^{1/2}$ ) we get for eqn(4.7):

$$\begin{aligned} \text{Branch1 } (x > 0) : P_x &= P_{inp} \cos^2(\phi/2) \\ \text{Branch2 } (x < 0) : P_x &= P_{inp} \sin^2(\phi/2) \end{aligned} \quad 4.8$$

The accumulated propagation phase difference  $\phi$ , at a given wavelength  $\lambda$ , is the sum of that in the tapered and in the central regions. We note  $\Delta\beta_t$  and  $\Delta\beta_c$  the differences between the propagation constants  $\beta_s$  and  $\beta_a$ , in the tapered and centre regions, respectively. At the wavelength  $\lambda$ , we have:

$$\phi(\lambda) = \int_{-L/2}^{-L/4} \Delta\beta_t(z, \lambda) dz + \int_{-L/4}^{L/4} \Delta\beta_c(z, \lambda) dz + \int_{L/4}^{L/2} \Delta\beta_t(z, \lambda) dz \quad 4.9$$

$$\phi(\lambda) = \phi_c(\lambda) + 2\phi_t(\lambda) = \Delta\beta_c \cdot L + 2 \int_{-L/4}^{L/4} \Delta\beta_t(\lambda, z) dz \quad 4.10$$

as  $\Delta\beta_c$  is a constant in the central region, and the two tapered regions are identical.

If we excite the device's port II, with the light at  $\lambda_1$  ( $=1.31 \mu\text{m}$ ) and  $\lambda_2$  ( $=1.55 \mu\text{m}$ ) together ( $\lambda_1 < \lambda_2$ ), the operating condition for demultiplexing is, that:

$$\Delta\beta_c(\lambda_1) \cdot L + 2\phi_t(\lambda_1) = m\pi \quad 4.11$$

$$\Delta\beta_c(\lambda_2) \cdot L + 2\phi_t(\lambda_2) = (m-1)\pi \quad 4.12$$

where  $m$  is an integer.

Indeed, under these conditions if  $m$  is even ( $m=2n$ ), in eqn(4.8) we have:

$$\begin{aligned} P_-(\lambda_1) &= \cos^2(n\pi) = 1, & P_x(\lambda_1) &= \sin^2(n\pi) = 0 \\ P_+(\lambda_2) &= \cos^2((n-\frac{1}{2})\pi) = 0, & P_x(\lambda_2) &= \sin^2((n-\frac{1}{2})\pi) = 1 \end{aligned} \quad 4.13$$

The light at  $\lambda_1$  is retrieved at the output port 1, and  $\lambda_2$  at the output port 2. If  $m$  is odd ( $m=2n-1$ ) the situation is reversed: the signal  $\lambda_1$  is retrieved at the output port 2, and  $\lambda_2$  at the output port 1.

We can calculate the extinction ratios  $ER(\lambda)$  at both wavelengths as:

$$ER(\lambda) = 10 \left| \log\left(\frac{P_x(\lambda)}{P_-}\right) \right| = 10 \left| \log \text{tg}^2(\phi/2) \right| \quad 4.14$$

Theoretically,  $ER(\lambda_1)=ER(\lambda_2)=-\infty$  since  $\text{tg}(\phi(\lambda))=0$  when  $\phi=2n\pi$  or  $(2n+1)\pi$ . Any change in  $\phi$ , i.e.  $\Delta\phi$  due to waveguide parameter errors, caused by fabrication, or an error in the designed  $L$  due to computations errors would result in a seriously degraded extinction ratio:

$$\begin{aligned} \Delta ER(\lambda) \neq -\infty, \quad \Delta ER(\lambda) &= 10 \log(\text{tg}^2(\Delta\phi(\lambda))) \\ &\approx 20 \log |\Delta\phi(\lambda)| \end{aligned} \quad 4.15$$

if  $\Delta\phi$  is small. For a small error in the phase angle of  $\approx 0.1$  rad ( $6^\circ$ ), the degraded extinction can be calculated using eqn(4.15) to be  $\Delta ER \approx 20 \log(0.1) \approx -20$  dB.

### 4.3 R parameter

Like Cheng and Ramaswamy [8], we introduce a reduced parameter  $R$  to solve the design problem. We start from the demultiplexing condition given by eqn(4.11) and eqn(4.12). This is a linear system of two equations in  $L$ . There is a solution for  $L$ , if the following condition is fulfilled:

$$\frac{m\pi - 2\phi_t(\lambda_1)}{(m-1)\pi - 2\phi_t(\lambda_2)} = \frac{\Delta\beta_c(\lambda_1)}{\Delta\beta_c(\lambda_2)} = R \quad 4.16$$

$$\begin{array}{ccc} & \uparrow & \uparrow \\ & R_1^m & R_2 \end{array}$$

## Chapter 4: Designs of a widened X-branch demultiplexer

---

The propagation constant difference  $\Delta\beta_c$  depends on the wavelength  $\lambda$ , the waveguide width  $w$ , the waveguide diffusion depth  $d$  or diffusion time  $t_d$  of the ion-exchange process ( $d = (D_e t_d)^{1/2}$  where  $D_e$  is the effective diffusion constant (See chapter 3).  $\phi_i$  depends on these parameters as well and also on the branching angle  $\alpha$ . Consequently, the condition stated in eqn(4.16)  $R_1^m = R_2 = R$  can be rewritten in full notation as:

$$R = \frac{m\pi - 2\phi_i(\lambda_1, w, t_d, \alpha)}{(m-1)\pi - 2\phi_i(\lambda_2, w, t_d, \alpha)} = \frac{\Delta\beta_c(\lambda_1, w, t_d)}{\Delta\beta_c(\lambda_2, w, t_d)} \quad 4.17$$

$\lambda_1$  and  $\lambda_2$  are, respectively,  $1.31\mu\text{m}$  and  $1.55\mu\text{m}$ . If we fix  $w$  and  $m$  and  $\alpha$ ,  $t_d$  must be found such that eqn(4.17) is verified. This condition can also be written as:

$$R_1^m(t_d) - R_2(t_d) = 0 \quad 4.18$$

The actual design problem is to solve this equation. In section 4.4.5 we will show on an example how this equation can be solved in practice. Once eqn(4.18) is solved and  $t_d$  known,  $L$  can be deduced by inverting either eqn(4.11) or eqn(4.12).

$$\begin{aligned} L &= \frac{m\pi - 2\phi_i(\lambda_1 = 1.31\mu\text{m}, \alpha, w, t_d)}{\Delta\beta_c(\lambda_1 = 1.31\mu\text{m}, w, t_d)} \\ &= \frac{(m-1)\pi - 2\phi_i(\lambda_2 = 1.55\mu\text{m}, \alpha, w, t_d)}{\Delta\beta_c(\lambda_2 = 1.55\mu\text{m}, w, t_d)} \end{aligned} \quad 4.19$$

### 4.4 Dispersion relation

The calculation of the ratios  $R_1^m$  and  $R_2$  versus various values of the design parameters is equivalent to solving the dispersion relation. To conduct our numerical simulations, we can use the data available in the literature for waveguides in glass by  $\text{K}^+ - \text{Na}^+$  ion-exchange at wavelength  $\lambda = 1.31\mu\text{m}$  and  $\lambda = 1.55\mu\text{m}$  [11]. The surface index obtained with  $\text{K}^+ - \text{Na}^+$  ion exchange changes with polarization and thus the widened X-branch, built using this technique, is polarization dependent [12]. The cases for TE and TM modes will be studied separately.

#### 4.4.1 The effective -index method

The effective-index method (EIM) is normally used in this Chapter, to reduce a three-dimensional problem to a two-dimensional one, thereby simplifying the problem. According to the results derived in Chapter 3, the first step of the EIM when studying channel waveguides and, therefore our X-branch, is to calculate the effective-index  $N_p$  of an equivalent slab waveguide for the same diffusion time  $t_d$ . The index change along the depth direction for a slab waveguide in glass by  $K^+$ - $Na^+$  ion exchange is known to be Gaussian [7]:  $\Delta n_y(y) = \Delta n_s \exp(-(y/d)^2)$ , where  $\Delta n_s = n_s - n_b$  ( $n_s$  is the surface index and  $n_b$  is the bulk index) and  $d = (D_e t_d)^{1/2}$  ( $D_e$  is the effective diffusion constant for the diffusion process as defined in Chapter 3)  $N_p$  can be calculated using the Runge-Kutta method described in Chapter 2. When calculating  $N_p$ , we must remember that we look for single mode operation of the individual waveguides in the tapered regions and dual mode operation in the central region. If we look at the the normalized parameter  $V'$  defined for channel waveguides in Chapter 3 as  $V' = (2\pi w/\lambda)(N_p^2 - n_b^2)^{1/2}$ , the rules for single-and dual-mode operation are roughly: (from Fig 3.10, Chapter 3)

$$\begin{aligned} \text{Single mode operation (tapered regions): } & 0.5 < V'(w) < 3.5 & 4.20 \\ \text{Dual mode operation (central regions): } & 3.5 < V'(2w) < 6.5 \end{aligned}$$

Numerical calculations (see Table 4.1) show that, in the range of values chosen for  $w$ :  $5.6 < w < 6.4 \mu\text{m}$  (waveguide width compatible for coupling with a monomode fiber),  $t_d$  must be chosen in the range [240-440] min for the TE modes and [200-320] min for the TM modes to satisfy eqn(4.20). If  $t_d$  is chosen above this range, a third order mode can be guided at  $\lambda = 1.31 \mu\text{m}$  in the central region. Below this range, the second order mode cannot be excited as a guided mode at  $\lambda = 1.55 \mu\text{m}$  in the central region. The discrepancies found in the diffusion time range allowed for the TE and TM modes are due to the polarization dependence of the surface index difference  $\Delta n_s = n_s - n_b$  and effective diffusion constant  $D_e$ . These two parameters determine the value of  $N_p$ . For these values of the diffusion time, the diffusion depth is around  $4 \mu\text{m}$  for both the TE and TM modes. The ratio of the long dimension over the short dimension  $2w/d$  is of the order of  $6 \mu\text{m}$  and the EIM can be applied with great accuracy away from the cutoff frequency of the modes (see Chapter 2).

After calculating  $N_p$  in the lateral direction, we can consider two models for the effective-index profile, in reference to the results obtained in studying the diffusion equation (See Chapter 3):

## Chapter 4: Designs of a widened X-branch demultiplexer

- the classic step-index model
- and the improved side-diffused model, including side diffusion (graded-index 'erf type' profile) (see Fig 4.3a,b).

When using the EIM, it should be remembered that the  $E_x$  component in a TE mode of the device structure becomes the E-component of the TE mode in the equivalent slab waveguide. (See Fig 2.3 Chapter 2).

**Table 4.1a,b,c,d: Index  $N_p$  and normalized parameters  $V'(w), V'(2w)$  vs  $t_d$**

$t_d$ (min)	$N_p$	$V'(w)$ Taper region	$V'(2w)$ Central region
<b>316</b>	1.504664	3.003	<b>6.006</b>
306	1.504583	2.969	5.939
296	1.504499	2.934	5.868
286	1.504412	2.896	5.793
276	1.504320	2.857	5.714
266	1.504225	2.815	5.630
256	1.504126	2.771	5.542
246	1.504023	2.724	5.448
236	1.503859	2.674	5.348
226	1.503801	2.621	5.242
216	1.503683	2.564	5.128
206	1.503558	2.503	5.006

$t_d$ (min)	$N_p$	$V'(w)$ Taper region	$V'(2w)$ Central region
316	1.501112	2.325	4.650
306	1.501027	2.292	4.585
296	1.500939	2.258	4.516
286	1.500847	2.221	4.443
276	1.500752	2.183	4.366
266	1.500653	2.143	4.285
256	1.500551	2.099	4.199
246	1.500444	2.054	4.108
236	1.500333	2.005	4.011
226	1.500218	1.954	3.908
216	1.500097	1.898	3.797
<b>206</b>	1.499977	1.839	<b>3.678</b>

**Tab 4.1 a) TM modes,  $\lambda=1.31 \mu\text{m}$**   
**For  $t_d \approx 316$  min,  $V'(2w)$  is close to 6.5.**  
**( $V'_{\text{cutoff}}$  for the third order mode)**

**Tab 4.1 b) TM modes,  $\lambda=1.55 \mu\text{m}$**   
**For  $t_d \approx 206$  min,  $V'(2w)$  is close to 3.5**  
**( $V'_{\text{cutoff}}$  for the second order mode)**

Chapter 4: Designs of a widened X-branch demultiplexer

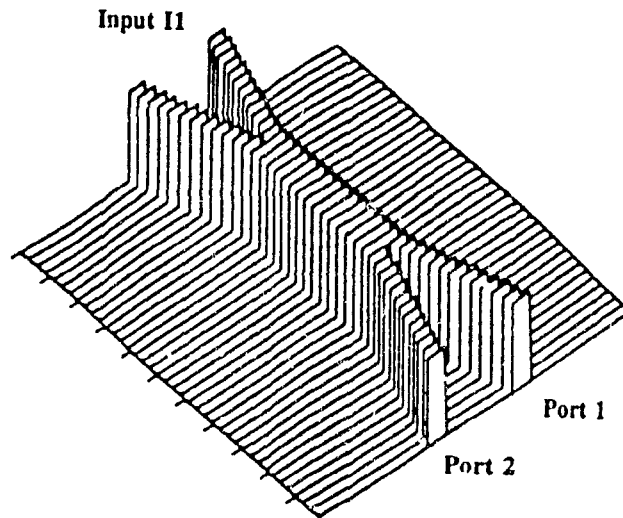
$t_d$ (min)	$N_p$	$V'(w)$ Taper region	$V'(2w)$ Central region
436	1.504570	2.964	<b>5.928</b>
426	1.504524	2.944	5.888
416	1.504476	2.924	5.848
406	1.504427	2.903	5.806
396	1.504376	2.881	5.763
386	1.504324	2.858	5.717
376	1.504270	2.835	5.670
366	1.504215	2.810	5.621
356	1.504158	2.785	5.570
346	1.504098	2.758	5.517
336	1.504037	2.730	5.461
326	1.503973	2.701	5.403
316	1.503909	2.671	5.342
306	1.503834	2.639	5.278
296	1.503769	2.605	5.210
286	1.503695	2.570	5.140
276	1.503657	2.533	5.066
266	1.503579	2.493	4.987
256	1.503457	2.452	4.904
246	1.503371	2.407	4.815

Tab 4.1c) TE modes,  $\lambda=1.31 \mu\text{m}$   
 For  $t_d=436$  min,  $V'(2w)$  is close to 6.5  
 ( $V'$  cutoff for the third order mode)

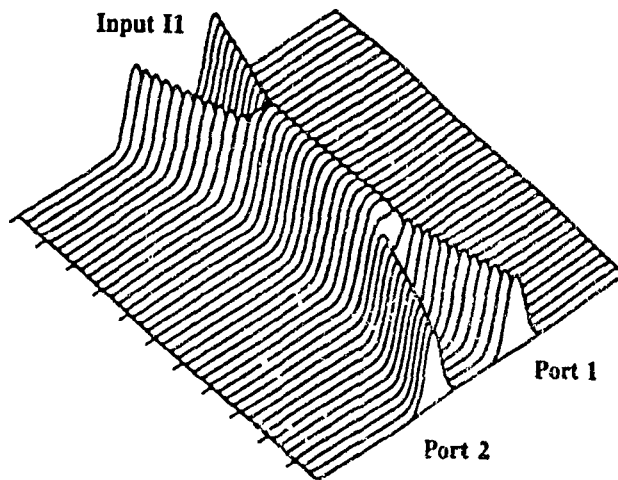
$t_d$ (min)	$N_p$	$V'(w)$ Taper region	$V'(2w)$ Central region
436	1.501044	2.299	4.600
426	1.500995	2.279	4.560
416	1.500945	2.260	4.520
406	1.500893	2.240	4.480
396	1.500840	2.218	4.438
386	1.500786	2.197	4.394
376	1.500730	2.174	4.348
366	1.500672	2.150	4.300
356	1.500612	2.125	4.251
346	1.500551	2.099	4.199
336	1.500487	2.073	4.145
326	1.500421	2.044	4.089
316	1.500354	2.015	4.030
306	1.500284	1.984	3.968
296	1.500211	1.951	3.902
286	1.500137	1.917	3.833
276	1.500059	1.880	3.761
266	1.499978	1.842	3.684
256	1.499895	1.801	3.603
<b>246</b>	1.499809	1.758	<b>3.517</b>

Tab 4.1d) TE modes,  $\lambda=1.55 \mu\text{m}$   
 For  $t_d=246$  min,  $V'(2w)$  is close to 3.5  
 ( $V'$  cutoff for the second order mode)

Fig 4.3a,b: Lateral effective index for the widened X-branch



4.3a) The step-index model



4.3b) The side-diffused model



## Chapter 4: Designs of a widened X-branch demultiplexer

-The Tapered regions.

Calculation of  $\Delta\beta_i$

In the case of the five-layer waveguide system, the electromagnetic fields in the different regions 1,2,3,4,5 (see Fig 4.4) can be expressed as [13]:

For TE modes:

$$E_y = \begin{aligned} & E_1^+ \exp(k_1 x) \\ & E_2^+ \exp(k_2 x) + E_2^- \exp(-k_2 x) \\ & E_3^+ \exp(k_3 x) + E_3^- \exp(-k_3 x) \\ & E_4^+ \exp(k_4 x) + E_4^- \exp(-k_4 x) \\ & E_5^+ \exp(-k_5 x) \end{aligned}$$

$$\text{where } k_i = \sqrt{\beta^2 - (k_0 n_i)^2} \quad i=1,2,3,4,5 \quad 4.21$$

$$\begin{aligned} \text{In our case: } n_1=n_3=n_5=n_b, \text{ hence } k_1=k_3=k_5=k_b \\ n_2=n_4=N_{\text{eff}}, \text{ hence } k_2=k_4=k_{\text{eff}} \end{aligned}$$

Matching the field at the boundaries, one obtain the eigenvalue equation for the TE modes [13]:

$$\begin{aligned} (2k_s k_{\text{eff}} + (k_s^2 - k_{\text{eff}}^2) \tan(k_{\text{eff}} w))^2 \\ - \exp(-2k_{\text{eff}} D) ((k_s^2 + k_{\text{eff}}^2) + \tan(k_{\text{eff}} w))^2 = 0 \end{aligned} \quad 4.22$$

A similar approach can be used in the case of the TM mode propagation. The eigenvalue equation is given by [13]:

$$\begin{aligned} (2A_{\text{eff}} A_s + (A_s^2 - A_{\text{eff}}^2) \tan(k_{\text{eff}} w))^2 \\ - \exp(-2k_{\text{eff}} D) ((A_{\text{eff}}^2 + A_s^2) \tan(k_{\text{eff}} w))^2 = 0 \end{aligned} \quad 4.23$$

where  $A_{\text{eff}} = k_{\text{eff}} n_{\text{eff}}^2 / k_0^2$

Solving numerically the dispersion relations, we can calculate the propagation constant of the symmetric and anti-symmetric modes  $\beta_s$  and  $\beta_a$  in the tapered regions, and, hence,  $\Delta\beta_i = \beta_s - \beta_a$ . Fig 4.6 and Fig 4.7 show  $\beta_s, \beta_a$  and  $\Delta\beta_i = \beta_s - \beta_a$  as a function of  $s(z)$  the spacing between the input or output branches. For the sake of brevity in this section, the results for  $\beta_s, \beta_a, \Delta\beta_i$ , and

## Chapter 4: Designs of a widened X-branch demultiplexer

$\phi_i$  in Fig 4.5, 4.6, 4.7 are plotted for TE and TM modes assuming  $w=6.0\mu\text{m}$ , and  $t_d=270$  min for the TM modes, and  $t_d=375$ min for the TE modes. These two different values for the diffusion time are approximately at the middle of the diffusion time range, allowed for the device operation at each polarization when a waveguide width around  $6.0\mu\text{m}$  is chosen (see Table 4.1). From Table 4.1 we can verify that  $N_p$  (TM modes,  $t_d=270$  min)  $\approx N_p$  (TE modes,  $t_d=375$  min) Therefore the results found for  $\beta_s$ ,  $\beta_a$ ,  $\Delta\beta_i$  and  $\phi_i$  for TE and TM modes, are close. From Fig 4.7 there is a clear exponential relationship for  $\Delta\beta_i$  as a function of the spacing length  $s=p-w$ .

$$\Delta\beta_i = \Delta\beta_0(\lambda) \exp\left(\frac{-(p(z)-w)}{c}\right) \quad 4.24$$

where  $\Delta\beta_0$  is the difference between the propagation constant of the symmetric and anti-symmetric modes if  $s(z)=0$ . In fact by continuity we can identify  $\Delta\beta_0=\Delta\beta_c$ . The characteristic spacing distance  $c$  can be calculated from Fig 4.7 to be around  $\approx 4\mu\text{m}$ .

The phase angle  $\phi_i$  is given by: (if we consider the first tapered region)

$$\phi_i = \int_{-z_i}^{-L/2} \Delta\beta_i(\lambda, z) dz \quad 4.25$$

The total phase angle due to the identical input and output tapered regions is, therefore,  $2\phi_i$ . We can calculate  $2\phi_i$  (see Fig 4.8) by direct numerical integration of  $\Delta\beta_i(s(z))$ , but we can also derive an analytical expression for it using the fitting formula given in eqn (4.24) for  $\Delta\beta_i(s(z))$ , in the integral expression (4.25). We can note that in the tapered region of our X-branch,  $s(z)=p(z)-w$  is given by  $s(z)=2 \cdot (z+L/2) \text{tg}(\alpha/2) \approx (z+L/2) \cdot \alpha$ , for small branching angles  $\alpha$ . The location of the device input  $-z_i$  is defined such that  $s(-z_i)=p(-z_i)-w=21\mu\text{m}$ , a spacing distance for which there is negligible coupling between the two input branches. The symmetric and anti-symmetric modes of the structure at this point are almost degenerate, and we have  $\exp(-s(z_i)/c) \approx \exp(-21/4) \approx 0$ , ( $\Delta\beta_i \approx 0$ ). Therefore, integrating eqn(4.25) yields:

$$\phi_i = \frac{c\Delta\beta_c(\lambda)}{\alpha} \quad 4.26$$

This relation is almost an exact fit to the curves plotted in Fig 4.8.  $\phi_i$  depends strongly on  $\alpha$ . Every time we double the branching angle, we halve  $\phi_i$  (see Fig 4.8).

## Chapter 4: Designs of a widened X-branch demultiplexer

An important point is that the variations of  $2\phi_c$ , with  $\lambda$  are significantly smaller than the same variations in  $\phi_c$ . For instance, from Fig 4.8a), we can calculate:  $2\phi_c(1.31\mu\text{m}) - 2\phi_c(1.55\mu\text{m}) \approx -1.4\text{rad}$  for  $w=6.0\mu\text{m}$ ,  $t_d=270\text{nm}$ ,  $\alpha=0.5^\circ$ , TM modes. From Fig 4.5a,b) we have for the same design parameters  $\Delta\beta_c(1.31\mu\text{m}) - \Delta\beta_c(1.55\mu\text{m}) = (7.09 - 6.48) \cdot 10^{-3} \approx 0.60 \cdot 10^{-3} \mu\text{m}^{-1}$ . Using the step index model, a length  $L$  about  $6000\mu\text{m}$  are predicted (see next Section) and we get:  $\phi_c(1.31\mu\text{m}) - \phi_c(1.55\mu\text{m}) = L \cdot (\Delta\beta_c(1.31\mu\text{m}) - \Delta\beta_c(1.55\mu\text{m})) \approx 6000 \times (0.61 \cdot 10^{-3}) = 4\text{rad} > |2\phi_c(1.31\mu\text{m}) - 2\phi_c(1.55\mu\text{m})| = 1.4\text{rad}$ .

### 4.4.3 The side-diffused model

When the side-diffused model is used,  $N_{\text{eff}}(x)$  is given by the following expressions (see Chapter 3 eqns(3.25) and (3.28)

In the central region:

$$N_{\text{eff}}(x) = N(x) = n_b + \frac{(N_p - n_b)}{2} \left( \text{erf}\left(\frac{x+w/2}{h}\right) - \text{erf}\left(\frac{x-w/2}{h}\right) \right) \quad 4.27$$

$$\text{where } h = 0.7 \cdot \sqrt{D_e t_d}$$

and in the tapered regions:

$$N_{\text{eff}}(x) = N(x+p/2) + N(x-p/2) - n_b \quad 4.28$$

The Yajima's method, good for the step index model, is not applicable in this case and we use the Runge-Kutta method also in the lateral direction. The results obtained for  $\beta_s$ ,  $\beta_a$ ,  $\Delta\beta_c$ ,  $\Delta\beta_t$  and  $\phi_c$  are shown Figs 4.5, 4.6, 4.7, 4.8. in comparison to those obtained, assuming a step-index profile for the effective index in the lateral direction. For the side diffused model we can calculate for  $w=6.0\mu\text{m}$ ,  $t_d=270\text{nm}$ ,  $\alpha=0.5^\circ$ , TM modes: from Fig 4.8a),  $2\phi_c(1.31\mu\text{m}) - 2\phi_c(1.55\mu\text{m}) \approx -0.7\text{rad}$ , and from Fig 4.5a,b)  $\Delta\beta_c(1.31\mu\text{m}) - \Delta\beta_c(1.55\mu\text{m}) = (7.26 - 6.06) \cdot 10^{-3} \approx 1.2 \times 10^{-3} \mu\text{m}^{-1}$ . As the side diffused model predicts a length  $L$  about  $3000\mu\text{m}$  (See next Section), we get  $\phi_c(1.31\mu\text{m}) - \phi_c(1.55\mu\text{m}) = L \cdot (\Delta\beta_c(1.31\mu\text{m}) - \Delta\beta_c(1.55\mu\text{m})) \approx 3000 \times (1.2 \times 10^{-3}) \approx 4\text{rad} >> |2\phi_c(1.55\mu\text{m}) - 2\phi_c(1.31\mu\text{m})| = 0.7\text{rad}$ . Qualitatively, the variations of  $\Delta\beta_c$  and  $\phi_c$  predicted by the step index or the side diffused model are similar.

Fig 4.5a,b,c,d:  $\Delta\beta_c(\lambda)$  vs  $t_d$  for different waveguide widths  $w$  at  $\lambda=1.31, 1.55\mu\text{m}$

— Step-index model — With side diffusion

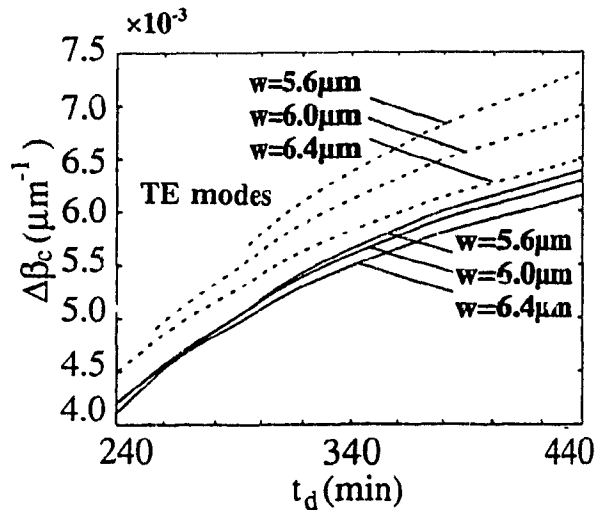
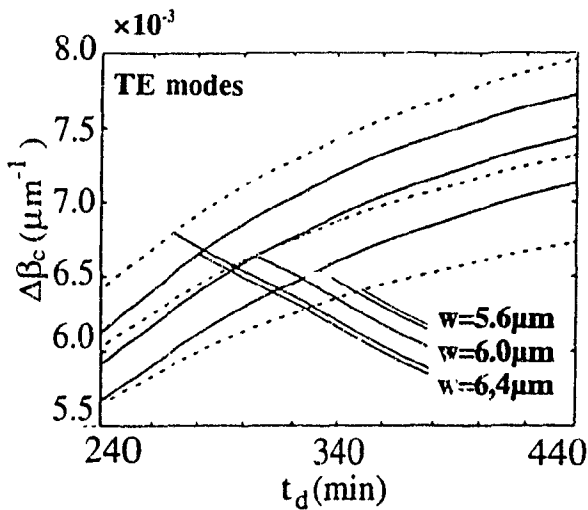
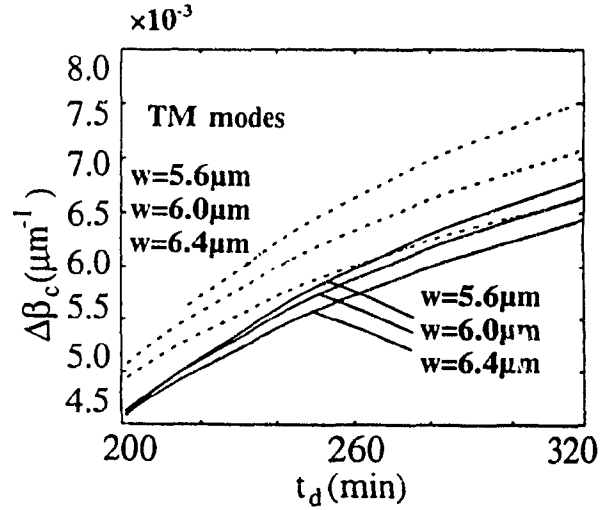
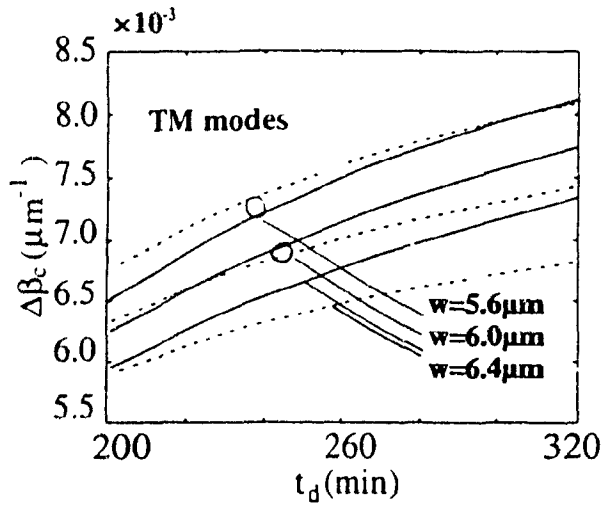
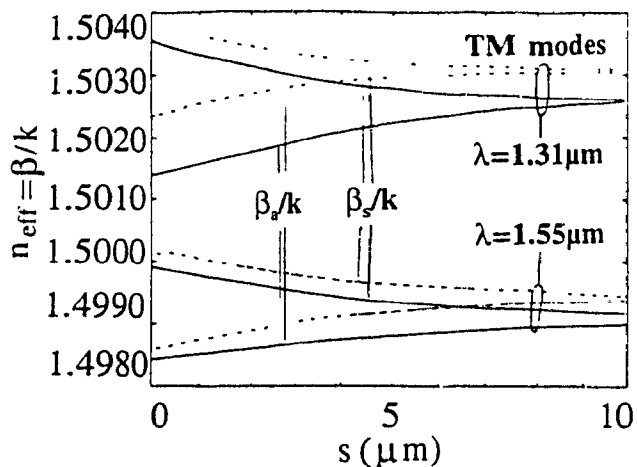
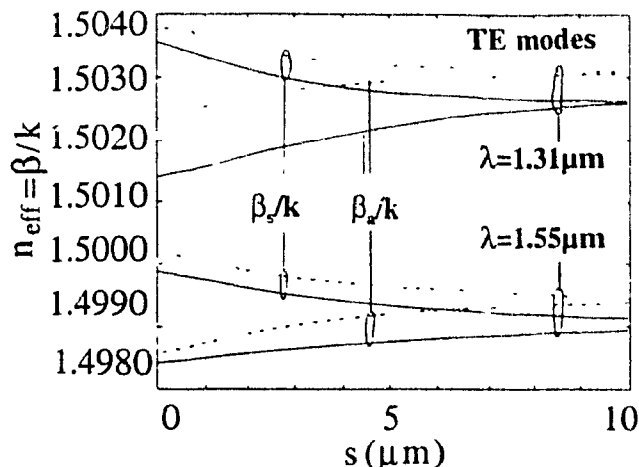


Fig 4.6a,b:  $\beta_s(\lambda), \beta_s(\lambda)$  vs  $s$  at  $\lambda=1.31\mu\text{m}, 1.55\mu\text{m}$  ( $w=6.0\mu\text{m}$ )

— Step-index model — With side-diffusion



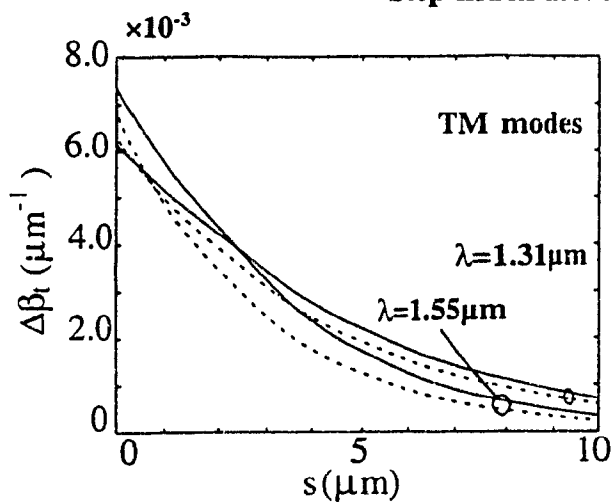
4.6 a) TM modes,  $t_d=270\text{min}$



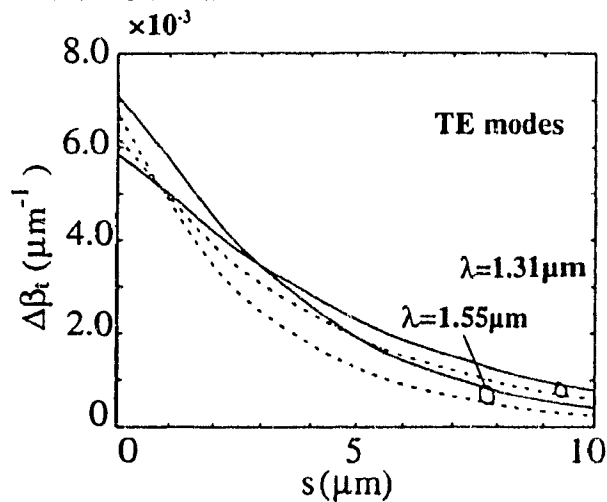
4.6b) TE modes,  $t_d=375\text{min}$

Fig 4.7a,b:  $\Delta\beta_t(\lambda)$  vs  $s$  at  $\lambda=1.31\mu\text{m}, 1.55\mu\text{m}$  ( $w=6.0\mu\text{m}$ )

— Step-index model — With side-diffusion



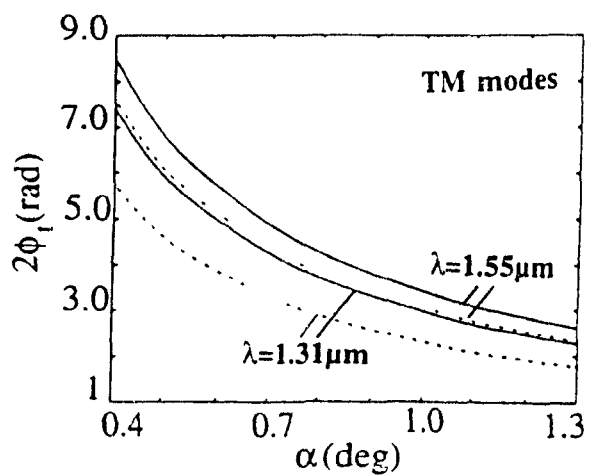
4.7a) TM modes,  $\lambda=1.31, 1.55\mu\text{m}, t_d=270\text{min}$



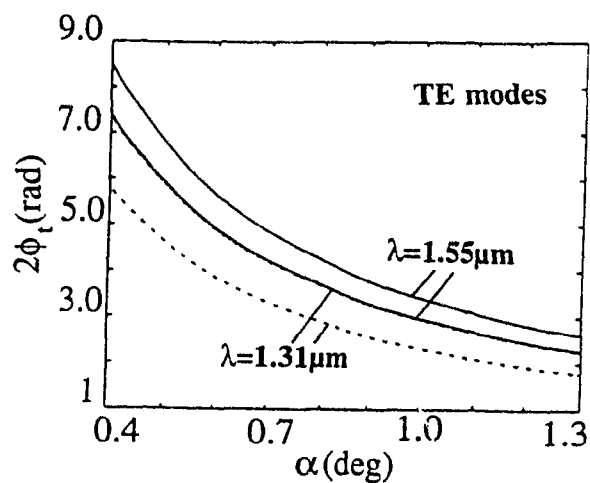
4.7b) TE modes,  $\lambda=1.31, 1.55\mu\text{m}, t_d=375\text{min}$

Fig 4.8a,b:  $\phi_t(\lambda)$  vs  $\alpha$  at  $\lambda=1.31,1.55\mu\text{m}$  ( $w=6.0\mu\text{m}$ )

----- Step-index model      ——— With side-diffusion



4.8a) TM modes,  $\lambda=1.31,1.55\mu\text{m}$ ,  $t_d=270\text{min}$



4.8b) TE modes,  $\lambda=1.31,1.55\mu\text{m}$ ,  $t_d=375\text{min}$

#### 4.4.4 Design example

For a fixed width  $w$  and branching angle  $\alpha$ , the variations of  $\beta_c$  and  $\phi_i$  with  $t_d$  being known, one can calculate separately  $R_1^m(t_d)$  and  $R_2(t_d)$  (as given by eqn (4.16), and then, solve the design characteristic equations  $R_1^m(t_d)=R_2(t_d)=R$  as in eqn (4.17) or  $R_1^m(t_d)-R_2(t_d)=0$  eqn(4.18), taking  $m$  as a parameter. Graphically, it corresponds to finding the point where the two representative curves of  $R_1^m(t_d)$  and  $R_2(t_d)$  intersect (see Fig 4.9). Once  $t_d$  is found,  $L$  is deduced from eqn(4.19) as stated in Section 4.3. Design values for  $L$ ,  $m$  and  $t_d$  are listed in Table 4.2 using the step-index model and our side-diffused model for the lateral effective index. From Tables 4.2a and 4.2c, 4.2b and 4.2d; 4.2e and 4.2g; 4.2f and 4.2h, we can see that the values of  $m, L$  found for TE, TM modes, for the same index models are close, but the corresponding diffusion time  $t_d$  are quite different. This polarization effect is due to the change of surface index with polarization as discussed in section 4.4.1. When we compare the results predicted by the step-index model and the side-diffused model, we can see that they are very different. For about the same diffusion time  $t_d$  the step-index model predicts much larger values for  $m$  and  $L$ , This point is discussed further in the next section.

We have described above a rigorous way to find the design parameters  $t_d$  and  $L$  for an optimized design. In fact, the order of magnitude for  $L$  can be evaluated in a simpler manner. We know, from the previous section, that, the wavelength dispersion of  $\phi_i$  is much smaller than the wavelength dispersion of  $\phi_c$ . Most of the phase shift needed for demultiplexing operation is gained in the central region and we can expect  $L$  to depend strongly on the properties of the symmetric and antisymmetric fields in this region. If we subtract eqn(4.11) from eqn(4.12) we can express the length  $L$  of the central region as

$$L = \frac{\pi + (2\phi_i(1.31\mu m) - 2\phi_i(1.55\mu m))}{\Delta\beta_c(1.31\mu m) - \Delta\beta_c(1.55\mu m)} \quad 4.29$$

From Fig 4.8 we have  $2\phi_i(1.55\mu m) - 2\phi_i(1.31\mu m) = 0.7\text{rad} < \pi$  (when the side-diffused model is used). Eqn(4.29) can be approximated by

$$L \approx \frac{\pi}{\Delta\beta_c(1.31\mu m) - \Delta\beta_c(1.55\mu m)} \quad 4.30$$

The order of magnitude of  $L$ , as given by this ratio, depends only on the difference  $\Delta\beta_c(1.31\mu m) - \Delta\beta_c(1.55\mu m)$ . For instance, for the side-diffused model, for  $w=6.0\mu m$ ,  $\alpha=0.5^\circ$ ,  $t_d$  about 250 min,

## Chapter 4: Designs of a widened X-branch demultiplexer

---

we find (from Fig 4.5):  $\Delta\beta_c(1.31\mu\text{m}) - \Delta\beta_c(1.55\mu\text{m}) \approx 7.0 - 5.7 \times 10^{-3} = 1.3 \times 10^{-3} \mu\text{m}^{-1}$ . Eqn(4.30) gives an approximate value for L of  $2500\mu\text{m}$ . This is comparable to the exact values listed Table 4.2a (error around  $500\mu\text{m} = 20\%$ )

### 4.4.5 Comparison between the step-index model and the side-diffused model

Typical field patterns along the widened X-branch structure are plotted in Fig 4.10, (the example of TM modes is taken), assuming the step-index model or the side-diffused model for the lateral effective index. The calculated fields are much different. For instance, one can notice that, in the tapered regions, the symmetric and anti-symmetric fields are much less confined into the individual guides when the diffused boundaries are assumed than when the step-index model is used.

If we look at the calculated propagation constants related to each field, the results obtained for the propagation constants of the symmetric and anti-symmetric modes along the structure ( $\beta_s$  and  $\beta_a$ , respectively (see Fig 4.6)) and, therefore,  $\Delta\beta_s$  and  $\phi_s$  and especially  $\Delta\beta_c$  (See Figs 4.7, 4.8 and 4.5) considering either the step-index or the side-diffused model for the lateral effective index are markedly different. When solving the design characteristic equations, as done in the previous section, the values calculated for  $R_1^m$  by the two models are still relatively close, but values for  $R_2$  ( $R_2 = \Delta\beta_c(1.31\mu\text{m})$ ,  $\Delta\beta_c(1.55\mu\text{m})$ ) are quite different and for about the same diffusion time, the design value L, m predicted by one model or the other are very different (of the order of thousands microns!, See Table 4.2). In terms of numerical accuracy, the step-index and side-diffused models are not consistent.

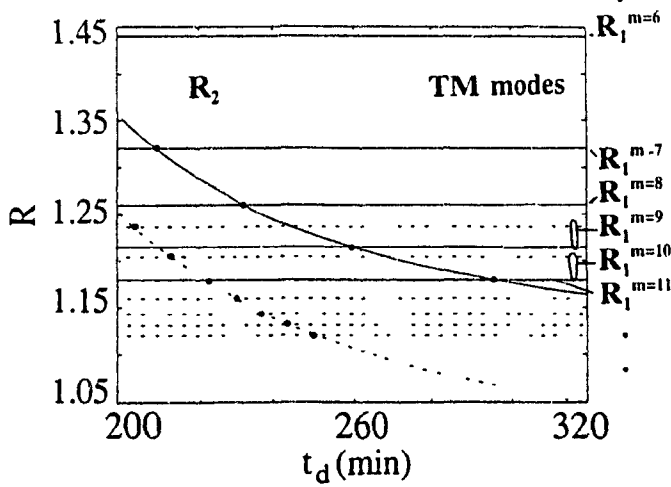
In Chapter 3, the side-diffused model using an erf fit was introduced as a better model than the step-index model. Indeed, it takes into account side diffusion and these effects are believed to be extensive when one wants to build channel guides in glass by  $\text{K}^+ - \text{Na}^+$  ion exchange. The propagation constant calculated by the side diffused model (erf fit) are believed to be closer to the exact values (see Table 3.2 Chapter 3). From now on the model we will consider in the rest of the theoretical study (the following Sections and Chapter 5) is the 'erf fit' side diffused model we presented Chapter 3. As for the step index model, we believe that when a TMI device such as our X-branch is considered, it is a good model if one only wants to predict the general behavior of the device and get a quick understanding of its physical principle. However, it fails to give results accurate enough for design purposes.

Chapter 4: Designs of a widened X-branch demultiplexer

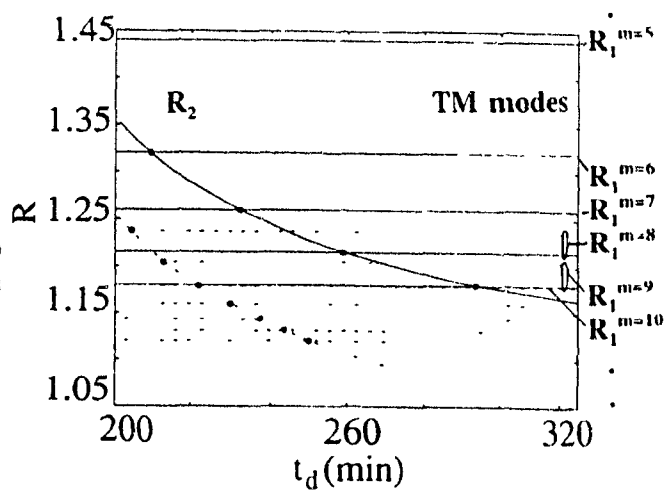
Fig 4.9:  $R_1^m$  and  $R_2$  vs  $t_d$  ( $w=6.0\mu\text{m}$ ) — Step-index model — Side diffused model

For sake of clarity  $R_1^m$  is not plotted for all the possible values of  $m$

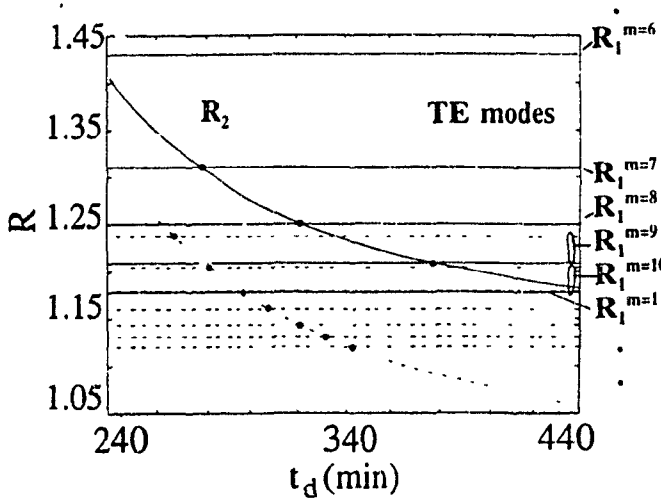
for both models



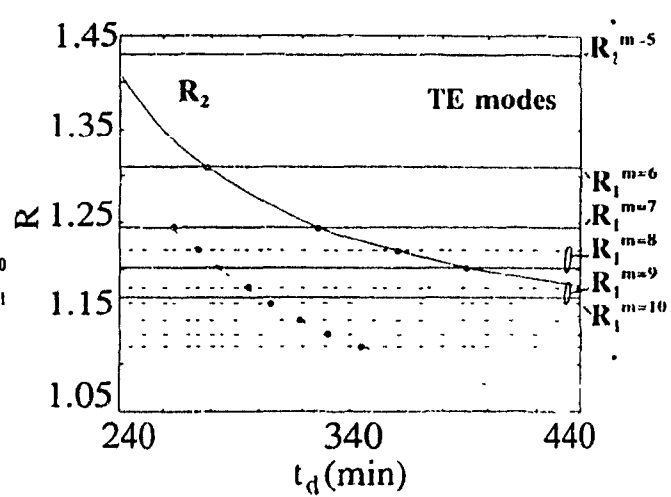
4.9a) TM modes,  $\alpha=0.5^\circ$



4.9b) TM modes,  $\alpha=0.8^\circ$



4.9c) TE modes,  $\alpha=0.5^\circ$



4.9d) TE modes,  $\alpha=0.8^\circ$

Chapter 4: Designs of a widened X-branch demultiplexer

Table 4.2 a-h): Design values  $t_d, m, L$  for TM, TE modes,  $\alpha=0.5^\circ$  or  $0.8^\circ$  ( $w=6.0\mu\text{m}$ )

$t_d$ (min)	m	R	L ( $\mu\text{m}$ )
257	9	1.216	3120
230	8	1.260	2830
205	7	1.327	2520

4.2a) Side diffused model, TM modes,  $\alpha=0.5^\circ$

$t_d$ (min)	m	R	L ( $\mu\text{m}$ )
251	15	1.201	6160
244	14	1.131	5770
237	13	1.144	4960

4.2b) Step index model, TM modes,  $\alpha=0.5^\circ$

$t_d$ (min)	m	R	L ( $\mu\text{m}$ )
375	9	1.237	3110
320	8	1.284	2820
265	7	1.352	2510

4.2c) Side diffused model, TE modes,  $\alpha=0.5^\circ$

$t_d$ (min)	m	R	L ( $\mu\text{m}$ )
257	15	1.201	6190
230	14	1.131	5790
205	13	1.438	5390

4.2d) Step index model, TE modes,  $\alpha=0.5^\circ$

$t_d$ (min)	m	R	L ( $\mu\text{m}$ )
266	8	1.207	2975
236	7	1.252	2680
209	6	1.321	2370

4.2e) Side diffused model, TM modes,  $\alpha=0.8^\circ$

$t_d$ (min)	m	R	L ( $\mu\text{m}$ )
228	12	1.301	5090
236	11	1.145	4690
244	10	1.164	4290

4.2f) Step index model, TM modes,  $\alpha=0.8^\circ$

$t_d$ (min)	m	R	L ( $\mu\text{m}$ )
375	8	1.202	2960
320	7	1.245	2680
265	6	1.312	2370

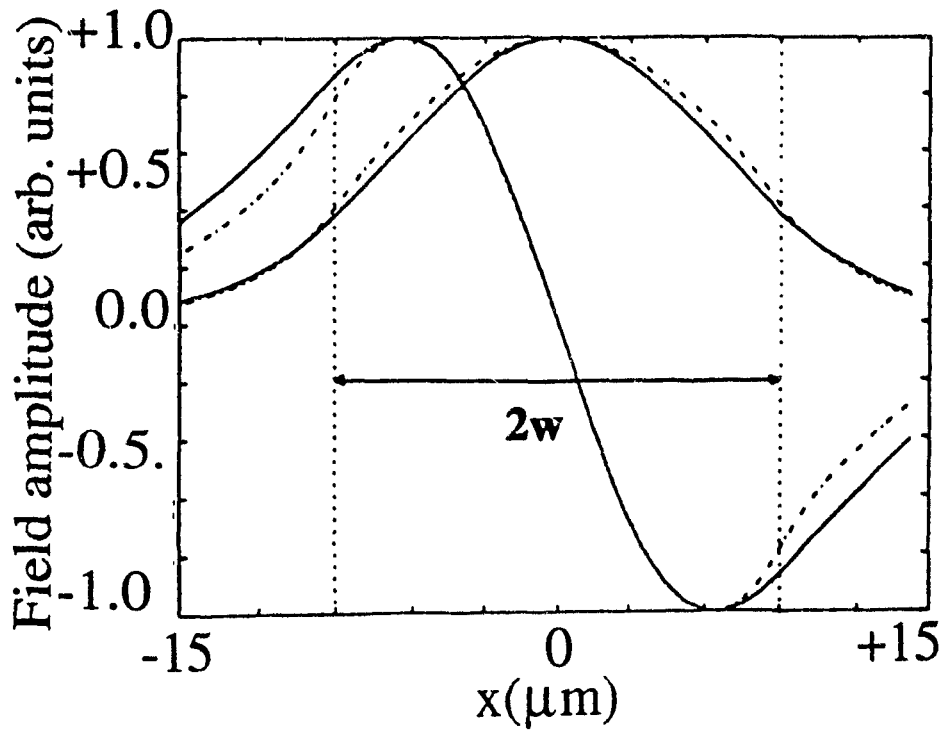
4.2g) Side diffused model, TE modes,  $\alpha=0.8^\circ$

$t_d$ (min)	m	R	L ( $\mu\text{m}$ )
257	12	1.301	5120
230	11	1.145	4720
205	10	1.164	4310

4.2h) Step index model, TE modes,  $\alpha=0.8^\circ$

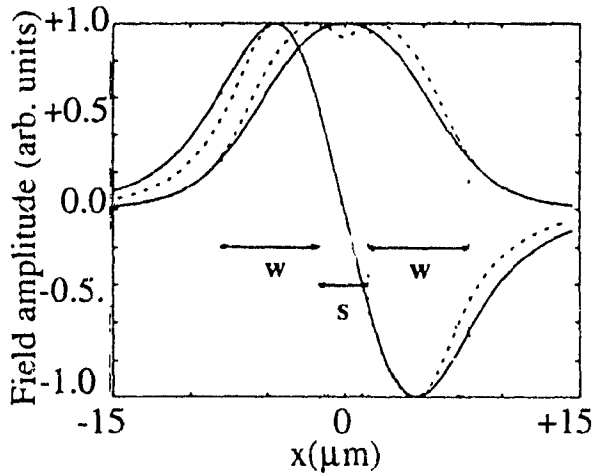
Fig 4.10a,b,c,d,e: Field plots for the TM modes in the widened X-branch ( $E_y$ )  
(lateral dependence in the central and tapered regions)

( $w=6.0\mu\text{m}, t_d=270\text{min}, \alpha=0.5^\circ$ ) —·— Step-index model — With side diffusion

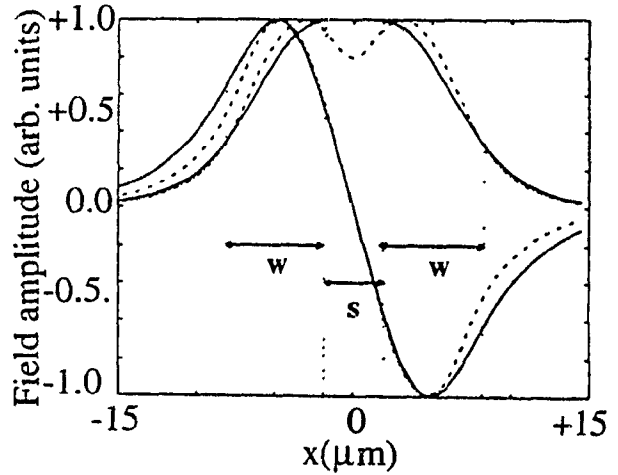


4.10a) In the central region

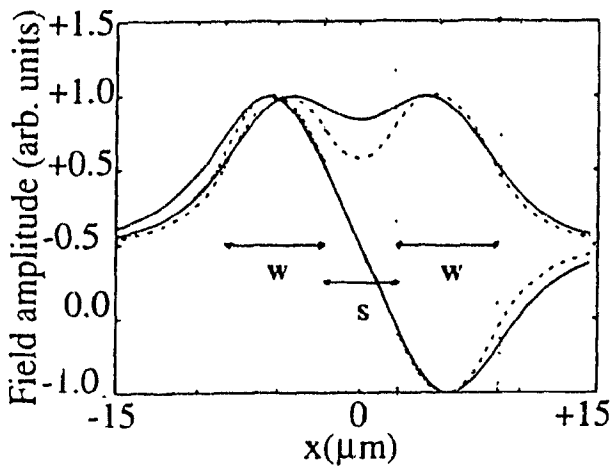
Chapter 4: Designs of a widened X-branch demultiplexer



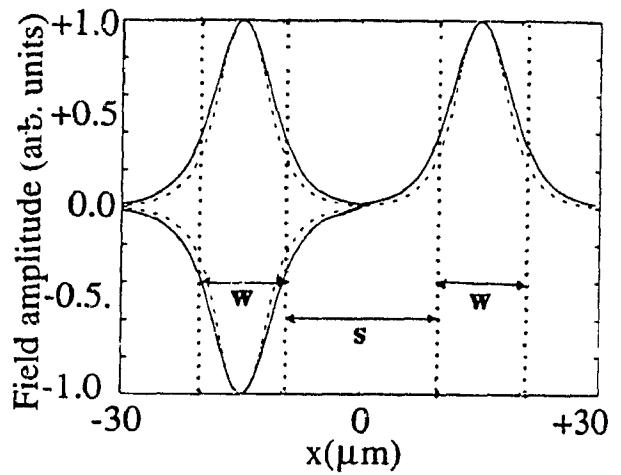
4.10b) In the tapered regions ( $s=1\mu\text{m}$ )



4.10c) In the tapered regions ( $s=2\mu\text{m}$ )



4.10d) In the tapered regions ( $s=4\mu\text{m}$ )



4.10e) In the tapered regions ( $s=14\mu\text{m}$ )

### 4.5 Design considerations

#### 4.5.1 Device length

For the obvious purpose of large integration, and the elimination of the difficulty to maintain the uniformity of the photolithographic process over a long distance, the length of the structure should be minimized. The length of the structure is the sum of the lengths in the tapered regions  $l_t$  and that in the centre region  $L$ , that is:  $L_{\text{Total}} = 2l_t + L$ .  $l_t$  is given by  $l_t = s(z_t)/(\tan(\alpha/2))$  (with  $s(z_t)=20\mu\text{m}$ ) and depends solely on the branching angle  $\alpha$ . Eqn(4.31) already derived in Section 4.4.4 gives a rough evaluation of the length  $L$  of the central region:

$$L \approx \frac{\pi}{\Delta\beta_c(1.31\mu\text{m}, w, t_d) - \Delta\beta_c(1.55\mu\text{m}, w, t_d)} \quad 4.31$$

As given by this equation,  $L$  depends almost only on the other design parameters ( $w$  and  $t_d$ ). Each length  $L$  and  $l_t$  can be minimized independently. This aspect is studied in the next section.

#### 4.5.2 Effect of the taper branch angle

The length of the tapered region  $l_t$  is proportional to  $1/\tan(\alpha/2)$  as we just stated. From this point of view, in order to minimize  $l_t$  and therefore the overall device length, one should choose as large an angle as possible. This is counting on no radiation modes, according to the approximation we made in Section 4.1. In reality, since  $\text{K}^+ \text{-Na}^+$  ion exchange surface waveguides are weakly guiding, too large a branching angle will generate the radiation fields through scattering and the values we can choose for  $\alpha$  are limited. A fuller investigation of this problem is done Chapter 5, by using the Beam Propagation Method. A branching angle  $\alpha$  of  $0.5^\circ$  is a good tradeoff.

#### 4.5.3 Waveguide width $w$ and diffusion time $t_d$

a) From the curves shown Fig 4.11, we can find that, the propagation constant difference,  $\Delta\beta_c(1.31\mu\text{m}) - \Delta\beta_c(1.55\mu\text{m})$ , is increased as the waveguide width or diffusion time  $t_d$  are decreased. From eqn(4.31), this means that narrower and shallower waveguides are to be preferred when looking for a shorter  $L$  (and consequently shorter overall dimensions). For instance, looking at Table 4.2, we can verify that  $L$  is a decreasing function of  $t_d$  (shallower

## Chapter 4: Designs of a widened X-branch demultiplexer

waveguides). Again, there is a tradeoff here good confinement of the modes should be insured if we want to avoid radiation modes that are not taken into account by the EIM but are revealed by the BPM in Chapter 5.

b) In c) and d) we study the tolerances on the design parameters  $w$  and  $t_d$  to keep, for an optimized device, an extinction ratio under -20 dB at both wavelength 1.31  $\mu\text{m}$  and 1.55  $\mu\text{m}$ . Deviations in the two parameters  $w$  and  $t_d$  cause deviations in  $\phi_{c,t}$  and therefore  $\phi$ . Overall, this yields a degraded extinction ratio  $\Delta ER(\lambda) = 20 \log[\Delta \phi(\lambda)]$  as given by eqn (4.15) where  $\Delta \phi$  is given by  $\Delta \phi = \Delta \phi_c + 2\Delta \phi_t$ . One notes that  $\phi_t$  is given by  $\phi_t = \Delta \beta_c \cdot c/\alpha$  and  $\phi_c$  by  $\phi_c = \Delta \beta_c \cdot L$ . Using these two relations to rewrite  $\Delta \phi_{c,t} = (d\phi_{c,t}/dt_d)\Delta t_d$  or  $\Delta \phi_{c,t} = (d\phi_{c,t}/dw)\Delta w$ , we can express the variations of the optimal extinction ratio with  $t_d$  or  $w$  as

$$\begin{aligned} \Delta ER(\lambda) &\approx 20 \log \left( L \frac{d(\Delta \beta_c(\lambda))}{dt_d} + 2 \frac{d(c\Delta \beta_c(\lambda))}{dt_d} \right) \cdot \Delta t_d \\ \Delta ER(\lambda) &\approx 20 \log \left( L \frac{d(\Delta \beta_c(\lambda))}{dw} + 2 \frac{d(c\Delta \beta_c(\lambda))}{dw} \right) \cdot \Delta w \end{aligned} \quad 4.32$$

Obviously, the sensitivity of the extinction ratio to variations in  $t_d$  or  $w$ , is directly related to the sensitivity of  $\Delta \beta_c$  to these two parameters. We use this relation in our tolerance study. The numerical results for the study are presented only for a device optimized for TM mode operation with  $t_d = 257$  min,  $w = 6.0 \mu\text{m}$ ,  $L = 3100 \mu\text{m}$ ,  $\alpha = 0.5^\circ$  (See Table 4.2a). The extensive calculations we performed show that we would get approximately the same results for devices with different design values  $w, t_d$  optimized for either TM or TE polarization.

c) For a given width  $w$ , the  $\Delta \beta_c$  vs  $t_d$  curves (Fig 4.5) are slightly flatter at shorter wavelengths than at longer wavelengths. In Fig 4.5, for  $w = 6.0 \mu\text{m}$ , the slope of the two curves can be calculated to be  $d(\Delta \beta_c)/dt_d = 1.256 \times 10^{-5} \mu\text{m}^{-1}/\text{min}$  if  $\lambda = 1.31 \mu\text{m}$  and  $d(\Delta \beta_c)/dt_d = 1.735 \times 10^{-5} \mu\text{m}^{-1}/\text{min}$  if  $\lambda = 1.55 \mu\text{m}$ , at the same corresponding  $t_d = 257$  min.  $\Delta \beta_c$  is more sensitive to the variations in  $t_d$  at longer wavelength than at shorter wavelength. Hence (see eqn 4.32) the output of the device is more sensitive to the diffusion time deviations at 1.55  $\mu\text{m}$  than at 1.31  $\mu\text{m}$ . The tolerance on  $t_d$ , to keep an extinction ratio under -20 dB, is around:  $\Delta t_d = \pm 5$  minutes at  $\lambda = 1.31 \mu\text{m}$  and  $\Delta t_d = \pm 4$  minutes at  $\lambda = 1.55 \mu\text{m}$  (see Fig 4.12). These tolerances are tight but not critical as  $t_d$  can be tightly controlled experimentally with a simple timer (the ion exchange is supposed to start almost as soon as the sample is dipped into the melt and stop as soon as it is withdrawn).

Fig 4.11:  $\Delta\beta_c(\lambda=1.31\mu\text{m})-\Delta\beta_c(\lambda=1.55\mu\text{m})$  vs  $t_d$  for different waveguide width,  $w$   
 (The side-diffused model is assumed for the index profile)

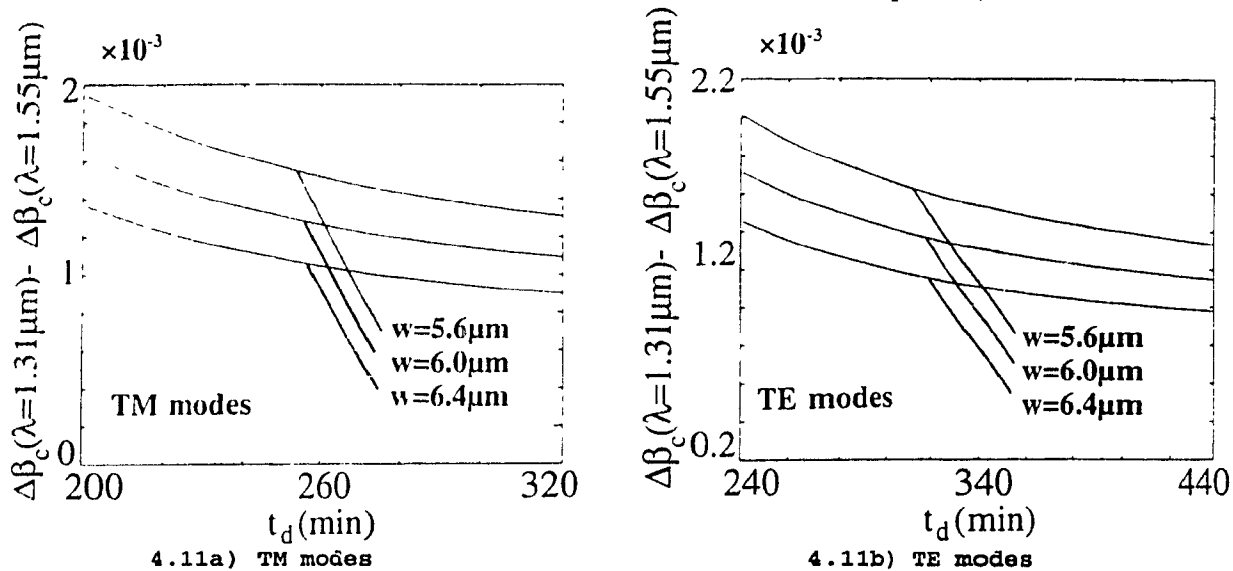
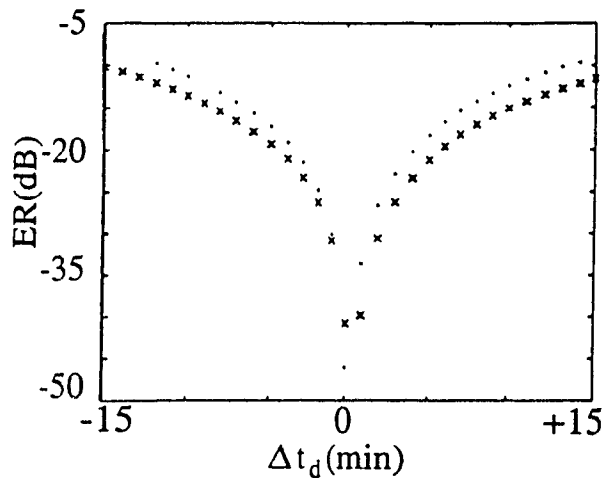


Fig 4.12: Extinction ratio  $ER(\lambda)$  vs diffusion time deviation  $\Delta t_d$   
 (Device design parameters  $w=6.0\mu\text{m}, t_d=257 \text{ min}, L=3100\mu\text{m}, \alpha=0.5^\circ$ ) TM modes  
 x x x  $\lambda=1.31\mu\text{m}$  . . .  $\lambda=1.55\mu\text{m}$



d) Due to the difficulty to control the photolithographic process used to fabricate the widened X-branch, errors in the waveguide width can be expected when fabricating the device. We can expect the error to be about the same in the tapered and central region  $\Delta(w)=\Delta(2w)$ . If  $w_c$  and  $w_t$  are the channel guide widths in the central and tapered regions, we have

$$\begin{aligned}\Delta(w) &= \Delta(2w) \\ w_c &= 2w + \Delta(2w) \\ w_t &= w + \Delta(w) \neq \frac{w_c}{2}\end{aligned}\tag{4.33}$$

The tolerance study is carried out under this assumption.

In Fig 4.5 for a given  $t_d$ ,  $\Delta\beta_c$  curves for varying  $w$  values at  $1.31\mu\text{m}$  and  $1.55\mu\text{m}$  are seen to be wider apart than those at  $1.55\mu\text{m}$ , indicating that  $\Delta\beta_c$  is more sensitive to the width variation at  $1.31\mu\text{m}$  than at  $1.55\mu\text{m}$ . Hence, (see eqn 4.32) the output of the device is more sensitive to the width deviation  $w$  at  $1.31\mu\text{m}$  than at  $1.55\mu\text{m}$  (see Fig 4.13). The tolerance on  $2w$  (width in the central region) to keep an extinction ratio under  $-20\text{ dB}$  is around:  $\Delta(2w)=\pm 0.15\mu\text{m}$  at  $\lambda=1.31\mu\text{m}$  and  $\Delta(2w)=\pm 0.6\mu\text{m}$  at  $\lambda=1.55\mu\text{m}$  for both TE and TM modes. Any width deviation is more critical at a shorter wavelength, since the photolithographic process cannot be controlled to give an error  $\Delta w$  below  $\pm 0.4\mu\text{m}$ .

When the deviations in width are small, it is always possible to adjust the diffusion time in order to obtain the highest possible extinction ratio at both wavelengths, even though the device will no longer be optimized at either wavelength. Fig 4.14 illustrates such considerations when an error of  $-0.2\mu\text{m}$  is assumed in the width  $2w$  for both TE and TM modes.

To compensate for larger positive error in  $w$ , one can think of depositing a dielectric cladding of a given thickness  $t$ , on the two-mode region of the waveguide as proposed by Chen in his thesis [6]. Principally, a cladding can increase the effective index of a waveguide, hence increasing the propagation constant difference between the symmetric and antisymmetric modes in the waveguides. Because positive width deviations reduce that difference (see Fig 4.5) the cladding compensation method can be applied to offset the effects. It was shown [15], however, that it was difficult to use a compensation method to improve the properties of a single device, at the two wavelength  $1.31\mu\text{m}$  and  $1.55\mu\text{m}$ , at the same time. When one wants to use the cladding

## Chapter 4: Designs of a widened X-branch demultiplexer

compensation method, it is more efficient to design not a single structure, but a cascaded structure [15-16] such as the one in Fig 4.15. The two wavelengths  $\lambda_1$  and  $\lambda_2$  are first separated by the device A, and then their extinction ratio shifts are compensated separately in the couplers B and C, respectively, by sputtering two dielectric layers of different thicknesses  $t(\lambda_1)$  and  $t(\lambda_2)$ . Improved extinction ratios versus width deviation characteristics have been theoretically calculated using the cladding compensation method for cascaded structures (see Fig 4.16 [6]). Cascaded structure have also the advantage of having higher extinction ratio since the outputs are described by

$$\frac{P_2}{P_{inp}} = \frac{P_z^C}{P_z^A} \times \frac{P_x^A}{P_{inp}} = \cos^4(\phi/2)$$
$$\frac{P_4}{P_{inp}} = \frac{P_x^B}{P_x^A} \times \frac{P_x^A}{P_{inp}} = \sin^4(\phi/2)$$
4.34

and the extinctions ratios at both wavelength  $\lambda_1=1.31\mu\text{m}, 1.55\mu\text{m}$  are

$$ER(\lambda) = 20|\log(\text{tg}^2(\phi/2))|$$
4.35

the extinction ratios are doubled compared to single structures (See eqn(4.14))

However, from the fabrication point of view the compensation method using cascaded structure, complicates the fabrication process since it involves two sputtering processes.

### 4.5.4 Bandwidth

The bandwidth of the device is very sharp as shown Fig 4.17 ( $\pm 0.02\mu\text{m}$ ). It is of the order of the error in the central wavelength of the laser diodes ( $\pm 0.03\mu\text{m}$ ) [17]. Unfortunately, this limitation is common to most of the TMI devices.

### 4.5.5 Limitations of the design method

To simplify the design calculations, in this thesis, we use the effective index method (EIM). Already by using this method we tend to overestimate the value of the calculated effective index of the modes by 0 to  $+5 \times 10^{-5}$  in the worst case (see Chapter 2, where the limits of the EIM have

been studied). Moreover when applying the EIM, we use an erf fit for  $N_{\text{eff}}(x)$  and not the exact expression of  $N_{\text{eff}}(x)$ . Limitations of this erf fit model have already been pointed out especially in the tapered regions of the waveguide (see Section 3.6.2) and can be expected to yield some error in computations. When designing our X-branch, what we consider is the difference  $\Delta n_{\text{eff}}$  between the effective indices of the symmetric and antisymmetric modes of the structure, and we can expect the same error made in each of the two effective indices to cancel each other. However, even for small discrepancies of the order of  $\delta(\Delta n_{\text{eff}}) \approx 5 \times 10^{-5}$ , we get an error in  $\beta_c$  of  $\delta(\Delta\beta_c) = 2\pi \times 5.10^{-5} / \lambda \approx 2.4 \times 10^{-4} \mu\text{m}^{-1}$ , and, therefore, an error of roughly 0.7 rad ( $+40^\circ$ ) for the phase angle  $\phi_c$  if a device length  $L$  of typically 3000  $\mu\text{m}$  is assumed. Without even considering the possible error in  $2\phi_c$ , the expected extinction ratio with such a phase shift in  $\phi_c$  is already reduced to about  $10\log(\text{tg}^2(20^\circ)) \approx 10$  dB!. This is a worst case figure but it gives an idea of the limitations of the design procedure used in this thesis, when looking for optimized device with extinction ratios below -20 dB. However, an encouraging point when we started the design computations was that, previous work on similar TMI device using the same EIM design procedure had shown close agreement between theory and experiment [8], [18]. Later in the experimental part of the work, we also obtained high extinction ratios, in good agreement with the theory.

The results of this tolerance study are comparable to the one that can be found in the literature [6], [14] when a step-index model is considered for the index profile. Compared to equivalent integrated demultiplexer devices [8], [19], the theoretical performances are competitive.

## 4.6 Conclusion

In this chapter we have carried out the preliminary design of a single mode widened X-branch type optical WDM device and the tolerance studies assuming a side-diffused index profile for the effective index. This type of profile is more realistic than the step-index profile, and from a numerical point of view makes, a difference. Compared to other equivalent integrated devices, the theoretical performances of the present device are competitive. The requirements on the design parameters are tight. One should note, that in this study no account has been made of the radiation modes. Under this simplification extinction ratios up to infinity are attainable. The beam propagation method is used in Chapter 5 to correct these idealized figures.

**Fig 4.13: Extinction ratio  $ER(\lambda)$  vs waveguide width deviation  $\Delta(2w)$**   
 (Device design parameters  $w=6.0\mu\text{m}, t_d=257 \text{ min}, L=3100\mu\text{m}, \alpha=0.5^\circ$ )  
 x x x  $\lambda=1.31\mu\text{m}$  . . .  $\lambda=1.55\mu\text{m}$

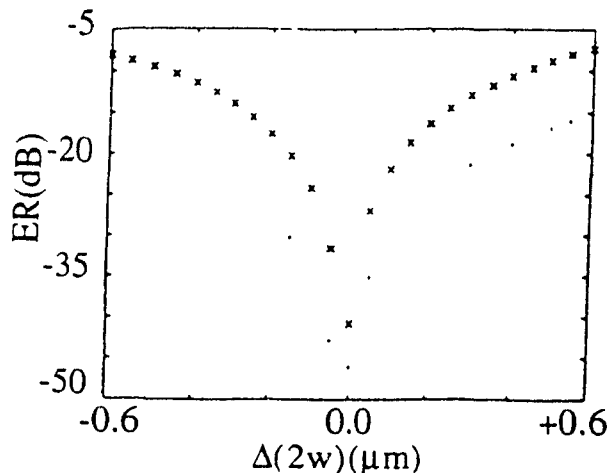


**Fig 4.14: Extinction ratio  $ER(\lambda)$  vs diffusion time deviation  $t_d$**   
 when an error of  $-0.2\mu\text{m}$  is assumed on the central width  $2w$   
 (Device design parameters  $w=6.0\mu\text{m}, t_d=257 \text{ min}, L=3100\mu\text{m}, \alpha=0.5^\circ$ )  
 x x x  $\lambda=1.31\mu\text{m}$  . . .  $\lambda=1.55\mu\text{m}$

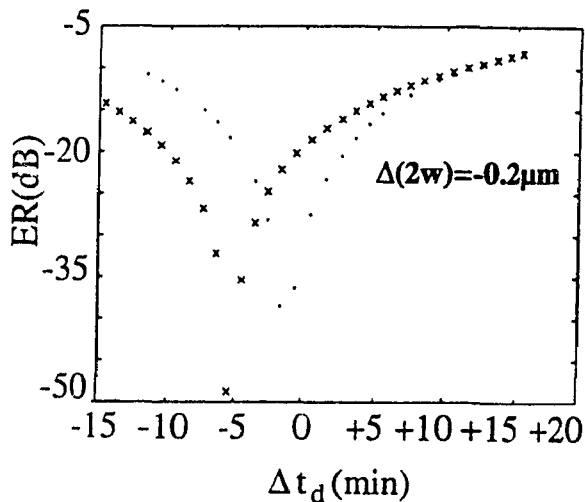


Fig 4.15: cascaded structure [6]

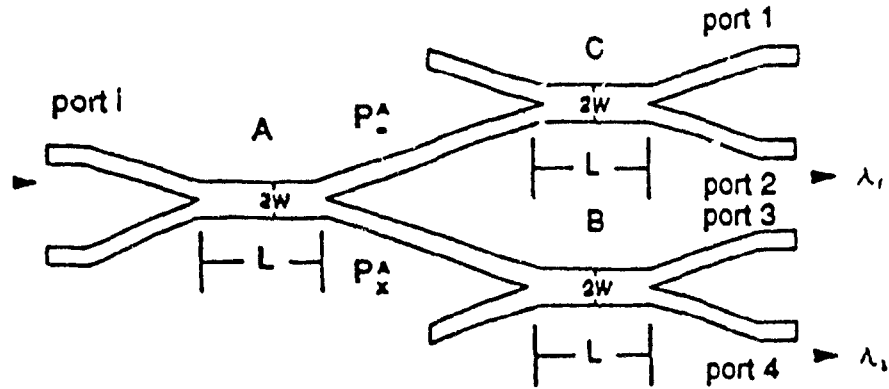


Fig 4.16: Extinction ratio  $ER(\lambda)$  of a cascaded structure vs central width deviation  $\Delta(2w)$  [6]  $\lambda \times \lambda = 1.31\mu\text{m}, \dots \lambda = 1.55\mu\text{m}$

⊙⊙⊙ improvement at  $1.31 \mu\text{m}$  due to a dielectric cladding of  $0.1, 0.2, 0.3\mu\text{m}$  respectively

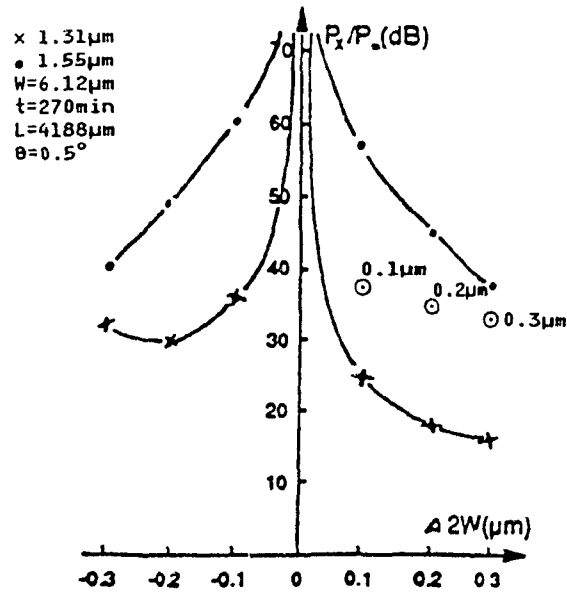
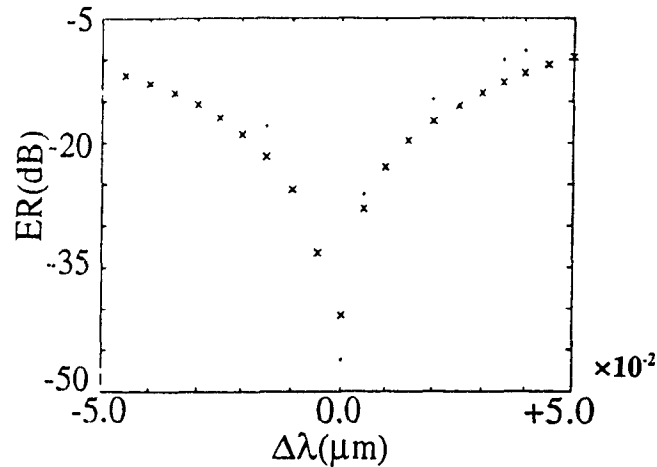


Fig 4.17: Extinction ratio  $ER(\lambda)$  vs wavelength deviation  $\Delta\lambda$   
(Device design parameters  $w=6.0\mu\text{m}, t_d=257 \text{ min}, L=3100\mu\text{m}, \alpha=0.5^\circ$ )

x x x  $\lambda=1.31\mu\text{m}$  . . .  $\lambda=1.55\mu\text{m}$



## References

- [1] Chen S. Tsai, B. Kim and F. R. El Akkari, "Optical channel waveguide switch and coupler using total internal reflection", IEEE J. of Quantum Electronics, Vol 14, pp. 513-57, 1978.
- [2] A. Neyer, "Electro-optic X-switch using single mode Ti:LiNbO<sub>3</sub> channel waveguides", Electronics Letters, pp. 553-554, 1983.
- [3] G. E. Betts and W. S. C. Chang, "Crossing channel waveguide electrooptic modulators", IEEE J. of Quantum Electronics, vol QE-22, pp. 1027-1028, 1986
- [4] A. Neyer. "Optimization of X-switch for integrated optical switching networks", Proceedings of IOOC-ECOC, Venice (Italy), pp. 369-372, 1985.
- [5] L. Thylen, "Integrated optics in LiNbO<sub>3</sub>: recent developments in devices for

## Chapter 4: Designs of a widened X-branch demultiplexer

---

- telecommunications", IEEE J. of Lightwave Technology, vol LT-6 pp 847-861, 1988.
- [6] J. Y. Chen, "Design considerations of a planar cross channel optical demultiplexer", M. Eng Thesis, Elect. Eng. Dept., pp.48-67 Mc Gill University, December 1991
- [7] G. L. Yip and J. Albert, "Characterization of planar optical waveguides by K<sup>+</sup>-ion exchange in glass", Optics Letters, Vol 10, pp. 151-153, 1985.
- [8] H. C. Cheng and R. V. Ramaswamy, "Symmetrical directional coupler as a wavelength multiplexer-demultiplexer: theory and experiment", IEEE J. of Quantum Electronics, Vol 27, pp.567-574.
- [9] E. Marom and S. Ruschin, "Relation between normal mode and coupled mode- Analyses of parallel waveguides", IEEE J. of Quantum Electronics, pp.1311-1319, 1984.
- [10] R. A. Forber and E. Marom, "Symmetric directional coupler switches", IEEE J. of Quantum Electronics, Vol 22, pp911-919, 1986
- [11] G. L. Yip, K. Kishioka, F. Xiang and J. Y. Chen, "Characterization of planar optical waveguides by K<sup>+</sup>-ion exchange in glass at 1.152 and 1.523  $\mu\text{m}$ ", OE/FIBERS'91, SPIE Proc., Boston 1991.
- [12] C De Bernardi, S. Morasca, D. Scarano, "Low Loss, high performance optical wavelength demultiplexers fabricated by Na<sup>+</sup>-K<sup>+</sup> ion exchange in glass", SPIE 1989.
- [13] H. Yajima, " Theory and applications of dielectric branching waveguides", in Proc. Symp. Optical and Acoustical Microelectronics, pp 339-359 (New York April 1974)
- [14] Y. Chung, J. Y. Yi, S. H. Kim and S. S. Choi, "Analysis of a tunable two mode interference wavelength division multi-demultiplexer", IEEE J. of Lightwave Tech., pp. 766-776, Vol LT-7, 1989.
- [15] K. Imoto, H. Sano, M. Miyazaki, H. Uethuka and M. Maeda, "Compensation for fabrication induced centre wavelength shift in a coupled waveguide type multi-demultiplexer", Appl. Opt., Vol 28, pp. 1904-1909, 1989.
- [16] K. Imoto, H. Sano and M. Miyazaki, "Guided wave multi/demultiplexers with high stopband rejection", Applied Optics, Vol 26, pp. 4214-4219, 1987.
- [17] Sakai, H. Shiraishi and M. Umeno, "AlGaAs/GaAs stripe laser diodes fabricated on Si substrates by MOCVD", IEEE J. of Quantum Electron., Vol 23, pp. 1080-1084, 1987.

#### Chapter 4: Design of a widened X-branch demultiplexer

---

[18] J. Albert and G. L Yip, "Wide single mode channels and directional coupler by two step ion exchange in glass" IEEE J of Lightwave Tech., Vol T-6, pp.552-563, 1988

[19] F Xiang and G L Yip, "Asymmetric Mach-Zender type wavelength demultiplexers", MOC/GRIN'93 Conference, Paper C4, October 1993.

## CHAPTER 5

# BEAM PROPAGATION METHOD ANALYSIS

In fiber and integrated optics, a typical waveguide problem involves the solution of Maxwell's equation in a finite domain bounded by an infinite domain, subject to the radiation condition at infinity and given an incident field or source. For many guiding structures of practical interest, there is no cylindrical symmetry and radiation losses need to be calculated. In this situation, it turns out that the classical eigenmode theory which is so successful for (closed) metal clad waveguides, is difficult to apply. The complete set of eigenmodes for such open waveguides must contain the continuum of radiation modes and this makes the use of eigenmode very unwieldy. In 1978, Feit and Fleck [1] introduced a new numerical modelling method, the so called Beam Propagation Method. Under appropriate circumstances, the BPM allows a unified treatment of guided and radiation modes in optical waveguiding structures and can provide a detailed and accurate description of the propagating field for a variety of realistic sources of illumination. Since then, this method has gained considerable popularity in the past decade in the area of guided wave optoelectronics and fiber optics. Many optical structures such as tapers [2], bends [3-4], gratings [5], couplers [6], Y-junctions [7], electrooptic waveguide modulators [8], non-linear directional couplers [9], waveguide crossings [10] and X-branch couplers [11-12] have been modeled and analyzed by the Beam Propagation Method. Also, different versions of the BPM have been proposed like the FFT-BPM [1], or more recently the faster FD-BPM [13-15].

In this Chapter the BPM is employed, in order to verify the design considerations developed in Chapter 4. The general theory of the BPM and implementation in its 2D-finite difference form, using the effective-index method (EIM), are introduced Sections 5.1, 5.2 and 5.3. The actual BPM simulations are presented in Section 5.4.

## 5.1 General Theory of the BPM

The propagation of the electromagnetic waves in an inhomogeneous medium (see Fig 5.1 p.94) is governed by the vector wave equation for the electric field as already derived (See eqn 2.7)

$$\nabla^2 \vec{E} + \nabla \left[ \frac{\vec{E} \cdot \nabla (n^2)}{n^2} \right] - k_0^2 n^2 \vec{E} = \vec{0} \quad 5.1$$

where  $k_0^2 = \omega^2 \mu_0 \epsilon_0$  and  $n = n(x, y, z)$  is the refractive index of the medium. If the refractive index varies slowly along z, from eqn (5.1), we can derive for the transverse component of the field  $E_t$ , a very similar relation to the one already derived for  $e_t$  in eqn(2.9)

$$\nabla_t^2 \vec{E}_t + n^2 k_0^2 \vec{E}_t = -\nabla_t [\nabla_t \ln(n^2) \vec{E}_t] \quad 5.2$$

This is the so called paraxial ray approximation all reflections in the z direction are neglected and the field propagates in a more or less paraxial fashion. In Chapter 2, the right-hand side term in eqn (5.2) was neglected under the weak guidance approximation. In this Chapter, we give the formulation for the full vector beam propagation method. Numerically, however, the weak guidance approximation proved to be correct. Written in terms of the y and x components, (5.2) becomes

$$\nabla_t^2 E_x + n^2 k_0^2 E_x = -\frac{\partial}{\partial x} \left( \frac{\partial \ln n^2}{\partial x} E_x \right) - \frac{\partial}{\partial x} \left( \frac{\partial \ln n^2}{\partial y} E_y \right) \quad 5.3$$

$$\nabla_t^2 E_y + n^2 k_0^2 E_y = -\frac{\partial}{\partial y} \left( \frac{\partial \ln n^2}{\partial x} E_x \right) - \frac{\partial}{\partial y} \left( \frac{\partial \ln n^2}{\partial y} E_y \right) \quad 5.4$$

Assume that  $E_{x,y} = \psi_{x,y} \exp(-jn_0 k_0 z)$  where  $n_0$  is a reference refractive index. Using this expression in (5.3) or (5.4) and making use of the slowly varying envelope approximation i.e.:

$$\left| \frac{\partial^2 \psi_t}{\partial z^2} \right| \ll 2n_0 k_0 \left| \frac{\partial \psi_t}{\partial z} \right| \quad 5.5$$

## Chapter 5: BPM simulation of a widened X-branch demultiplexer

We obtain the Fresnel vector wave equations

$$J \frac{\partial \psi_x}{\partial z} = H_{xx} \psi_x + H_{xy} \psi_y \quad (5.6)$$

$$J \frac{\partial \psi_y}{\partial z} = H_{yx} \psi_x + H_{yy} \psi_y \quad (5.7)$$

where the differential operators are defined by

$$H_{xx} \psi_x = \frac{1}{2n_0 k_0} \left[ \frac{\partial}{\partial x} \left[ \frac{1}{n^2} \frac{\partial}{\partial x} (n^2 \psi_x) \right] + \frac{\partial^2 \psi_x}{\partial x^2} + (n^2 - n_0^2) k_0^2 \psi_x \right] \quad (5.8)$$

$$H_{yy} \psi_y = \frac{1}{2n_0 k_0} \left[ \frac{\partial^2 \psi_y}{\partial y^2} + \frac{\partial}{\partial y} \left[ \frac{1}{n^2} \frac{\partial}{\partial y} (n^2 \psi_y) \right] + (n^2 - n_0^2) k_0^2 \psi_y \right] \quad (5.9)$$

$$H_{xy} \psi_y = \frac{1}{2n_0 k_0} \left[ \frac{\partial}{\partial x} \left[ \frac{1}{n^2} \frac{\partial}{\partial y} (n^2 \psi_y) \right] - \frac{\partial^2 \psi_y}{\partial x \partial y} \right] \quad (5.10)$$

$$H_{yx} \psi_x = \frac{1}{2n_0 k_0} \left[ \frac{\partial}{\partial y} \left[ \frac{1}{n^2} \frac{\partial}{\partial x} (n^2 \psi_x) \right] - \frac{\partial^2 \psi_x}{\partial x \partial y} \right] \quad (5.11)$$

Under the slowly varying envelope approximation, also known as the paraxial approximation, the transverse electric field of an electromagnetic wave propagating along the +z direction can be traced when it passes through an inhomogeneous medium by solving eqns (5.6) and (5.7) for the x and y polarized waves. The vector properties cause the polarization dependent propagation of the optical waves due to  $H_{xx} \neq H_{yy}$  and the coupling between the polarization through  $H_{xx}$  and  $H_{yy}$ . For two dimensional structures, the polarization coupling terms associated with  $H_{yy}$  and  $H_{yx}$  vanish. The vector fields may be decomposed into the TE (x-polarized transverse E field) and

TM (y-polarized transverse E field) ones which can be treated separately.

If the structures are weakly guiding (i.e. the index profile is a slowly varying function over one wavelength in the transverse directions), even the polarization dependence of the propagating waves may be neglected. Under the scalar approximation eqns(5.6) and (5.7) are replaced by a single wave equation:

$$j \frac{\partial \psi}{\partial z} = H \psi \quad 5.12$$

where  $\psi = \psi_x$  or  $\psi_y$  and.

$$H = \frac{1}{2n_0 k_0} \left[ \frac{\partial^2}{\partial x^2} + \frac{\partial^2}{\partial y^2} + (n^2 - n_0^2) k_0^2 \right] \quad 5.13$$

Equations (5.6), (5.7) or (5.12) can be solved by using a finite-difference method.

### 5.2 The EIM and the BPM method

With the BPM simulations, the EIM can be used to reduce a 2D problem in the transverse plane (variables x,y) to a 1D problem (variable x). To solve the 1D problem, a two-dimensional finite difference scheme, can be implemented, which is much more efficient in terms of the computer time than the three-level scheme that would be needed to solve a 2D problem. The index  $n(x)$  is identified with the effective index of the EIM (See Fig 5.1). In the case of the widened X-branch  $N_{\text{eff}}(x)$  is given by eqns (4.27) for the central region and (4.28) for the tapered regions respectively (the side diffused boundaries are used). It should be noted again that the  $E_x$  component in a TE mode of the device structure becomes the E-component of the TM mode in the equivalent waveguide, extending to  $-\infty$  and  $+\infty$  in the y-direction, in the EIM. When applying the vector form of the BPM, the propagation of a TE mode of the whole structure is simulated by the propagation of a TM mode of the equivalent, slab structure with refractive index  $N_{\text{eff}}(x)$ , according to the EIM rules (and vice versa for the TM modes, see Fig 2.2 and 2.3 Chapter 2).

### 5.3 The 2D finite difference method

#### 5.3.1 The Implementation

Assuming that we have a structure with an index profile  $n(x,z)$ , in the finite-difference solutions, the continuous space is discretized into a lattice structure defined in the computation region (see Fig 5.1). The fields at the lattice point of  $x=m\Delta x$  and  $z=l\Delta z$  are represented by  $\psi_x^l(m)$ (TE polarization) and  $\psi_y^l(m)$  (TM polarization) respectively.

The finite-difference expressions are [15] :

$$\frac{\partial \psi_{x,y}(x,z)}{\partial z} = \frac{\Psi_{x,y}^{l+1}(m) - \Psi_{x,y}^l(m)}{\Delta z} \quad 5.14$$

$$H_{xx} \psi_x^l = \frac{T_{m+1}^l \psi_x^l(m+1) - [2 - R_{m+1}^l - R_{m-1}^l] \psi_x^l(m) + T_{m-1}^l \psi_x^l(m-1)}{(\Delta x)^2} + (n^2(m,l) - n_0^2) k_0^2 \psi_x^l(m) \quad 5.15$$

where:

$$T_{m\pm 1}^l = \frac{2n^2(m\pm 1,l)}{n^2(m\pm 1,l) + n^2(m,l)} \quad 5.16$$

$$R_{m\pm 1}^l = T_{m\pm 1}^l - 1 \quad 5.17$$

are the transmission and the reflection coefficients across the index interface between  $m\Delta x$  and  $(m+1)\Delta x$  and  $(m-1)\Delta x$ .

$$H_{yy} \psi_y^l = \frac{\psi_y^l(m+1) - 2\psi_y^l(m) + \psi_y^l(m-1)}{(\Delta x)^2} + (n^2(m,l) - n_0^2) k_0^2 \psi_y^l(m) \quad 5.18$$

Under the scalar approximation, there is only one relation for both polarization:

$$H_{xx}\psi = H_{yy}\psi = H\psi = \frac{\psi(m+1) - 2\psi(m) + \psi(m-1)}{(\Delta x)^2} + [n^2(m,l) - n_0^2]k_0^2 \quad 5.19$$

Potassium ion-exchanged waveguides correspond to the weakly guiding case:  $n(m,l) \approx n(m \pm 1, l)$ ,  $T_{m \pm 1, l} \approx 1$  and  $R_{m \pm 1, l} \approx 0$ . Computation tests made by using the vector or scalar representations yield the same results. Therefore in the design computations for our widened X-branch we find that we can use simpler the scalar representation.

To establish a propagative relation, we can opt for the Crank-Nicolson version of the finite difference method. It is numerically the least dissipative scheme, especially when the transparent boundary conditions [16] are used as in our case. The stability of the method will be discussed later. The Crank-Nicolson scheme is an implicit scheme. The relation between the field  $\psi^{l+1}$  at  $z+\Delta z$ , and the field  $\psi^l$  at  $z$ , is given by :

$$\frac{\psi^{l+1} - \psi^l}{\Delta z} = \frac{1}{2} (vH\psi^{l+1} + (1-v)H\psi^l) \quad 5.20$$

where  $0 < v < 1$ . Under the scalar approximation, this means [14]:

$$\begin{aligned} A_{m+1}^{l+1}\psi^{l+1}(m+1) + A_m^{l+1}\psi^l(m) + A_{m-1}^{l+1}\psi^l(m-1) = \\ A_{m+1}^l\psi^l(m+1) + A_m^l\psi^l(m) + A_{m-1}^l\psi^l(m-1) \end{aligned} \quad 5.21$$

where [14]:

$$A_{m \pm 1}^{l+1} = j \frac{v \cdot \Delta z}{2k_0 n_0 (\Delta x)^2} \quad 5.22$$

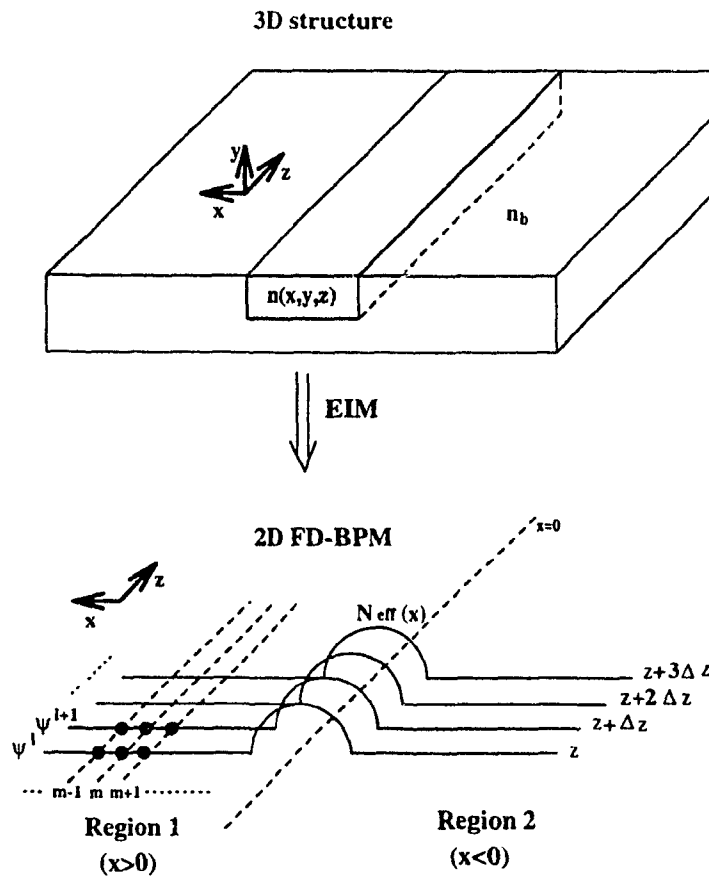
$$A_m^{l+1} = 1 + j \frac{v \cdot \Delta z}{2k_0 n_0} [(n^2(m, l+1) - n_0^2)k_0^2 - \frac{2}{(\Delta x)^2}] \quad 5.23$$

$$A_m^l = 1 - j \frac{(1-\nu) \cdot \Delta z}{2kn_0} \left[ (n^2(l,m) - n_0^2)k^2 - \frac{2}{(\Delta x)^2} \right] \quad 5.24$$

$$A_{m+1}^l = -j \frac{(1-\nu) \cdot \Delta z}{2kn_0(\Delta x)^2} \quad 5.25$$

This system can be solved using a classical LDU decomposition and the values for the field  $\psi^{l+1}(m)$  at  $z+\Delta z$  can be deduced from those for  $\psi^l(m)$  at  $z$ , for each propagation step.

Fig 5.1: Schematic representation of the 2D FD-BPM method



### 5.3.2 Stability-Step size

A finite-difference method is stable if every solution of the form [15]:

$$\psi^l(m) = g^l e^{-j(mk_x \Delta x)} \quad 5.26$$

is stable, that is for any  $m, l$  we have  $|\psi^{l+1}(m)/\psi^l(m)| = |g^{l+1}(m)/g^l| < 1$ .

Using expression (5.26) for  $\psi^m$  into the finite difference form of the (scalar wave) BPM eqn (5.19), and separating  $g^l$  and  $g^{l+1}$ , an expression for the ratio  $g^{l+1}/g^l$  can be derived for both TE and TM polarization as [15]:

$$\frac{g^{l+1}}{g^l} = \frac{1 - j \frac{(1-\nu)\Delta z}{2kn_0} [(n^2(m, l+1) - n_0^2)k_0^2 - \frac{4}{(\Delta z)^2} \sin^2(\frac{k_x \Delta x}{2})]}{1 + j \frac{\nu \Delta z}{2kn_0} [(n^2(m, l) - n_0^2)k_0^2 - \frac{4}{(\Delta z)^2} \sin^2(\frac{k_x \Delta x}{2})]} \quad 5.27$$

For small variations of  $n$  with  $z$  i.e.  $n(m, l+1) \approx n(m, l)$ , the step size  $\Delta z$  is small, it can be proved that this ratio is less than 1 for any value of  $\nu$  or  $\Delta x$  [15]. In order to minimize the power dissipation, ( $|g^{l+1}/g^l| \approx 1$ ), it is preferable however to choose  $\nu \approx 0.5$ .

For the numerical simulations, the following parameters can be used when implementing the BPM:

- a)  $0.5 < \nu < 0.55$ . As  $\nu$  gets closer to 0.5, the numerical noise tends to increase and on the BPM plots one can see anomalous ripples and oscillations in the field pattern.
- b)  $\Delta z$  between 0.1 and 2  $\mu\text{m}$ : In terms of extinction ratio calculations, using step-sizes between  $\Delta z = 2\mu\text{m}$  and  $\Delta z = 0.1\mu\text{m}$  appears to yield similar results. However, when we look at the BPM plots, the smaller the stepsize the less numerical noise we will get. On the other hand, the time duration of a simulation becomes excessive for too small a step-size. With a step-size  $\Delta z$  of 2  $\mu\text{m}$ , our BPM simulation takes already  $\approx 45$  minutes on a Sun Sparc station for a total device length of  $L + 2l_1 = 3000 + 4800 = 7800\mu\text{m}$ .
- c) window size = 100  $\mu\text{m}$ .
- d) number of points in the transverse direction  $M = 1200$ , that is a step size in the lateral direction of  $\Delta x = 100/1200 = 0.08333\mu\text{m}$ .

e) According to Huang [15] the reference index can be chosen to be  $n_0 = (\beta_s + \beta_a) / 2k_0$ , which is roughly constant along the structure.

### 5.3.3 The boundary conditions

At the edges of the computation window, the transparent boundary conditions (TBC) [16] can be applied. The TBC state that near the boundary at the right (or left) end of the computation window along the x-axis ( ie  $x = m\Delta x$  ) the field should satisfy a relation of the form [16].

$$\psi(x,z) = \psi_0 e^{-jk_x x} \quad 5.28$$

where  $\psi_0$  and  $k_x$  are complex constants. The real part of  $k_x$  should be positive if we want radiative energy to flow out of the problem region and not be reflected back in at the boundary [16]. In the finite difference form, we can write (for the right boundary):

$$\psi^{l+1}(M) = \psi^{l+1}(M-1) e^{-jk_x \Delta x} \quad 5.29$$

where  $\exp(-jk_x \Delta x)$  is computed from the previous step by calculating the ratio  $\psi^{l+1}(M) / \psi^{l+1}(M-1) = \exp(-jk_x \Delta x)$ . The transparent boundary conditions are superior to the conventional absorbing boundary conditions because they are more efficient and accurate. In addition, the implementation of the transparent boundary conditions is relatively independent of the waveguide structures simulated. Therefore, the transparent boundary conditions are more robust than the conventional absorbing boundary conditions.

### 5.3.4 The input excitation

When we consider a graded-index profile, usually there is no exact analytical expression for the fundamental mode of a waveguide. This is the case for an erf-type refractive-index profile such as the one in our widened X-branch. The fundamental mode of an input branch of width  $w$ , with a step index taken as  $N_{\text{erf}}(x=0)$ , is used as an approximation. Indeed, for such a step index structure, an analytical expression is readily available for the fundamental mode. This input is close to the exact eigenmode, still it has to adjust itself at the initial stage of propagation in order to become the eigenmode of the branch. This mismatch causes small radiation loss in the first few steps of propagation.

### 5.3.5 The output power evaluation

Applying the BPM to the analysis and design of our widened X-branch demultiplexer requires the power evaluations in the two particular output regions  $r=1$  and  $r=2$  (See Fig 5.1 shown previously). The output field might be written in each region as

$$\psi_{out} = c_g \phi_g + \sum c_i \phi_i \quad 5.30$$

where  $\phi_g$  is the fundamental guided mode of an output branch, and  $\phi_i$  are spurious radiative modes. The output power in each region is given by  $\sum c_i(r)^2 = \text{Output power}$ . The actual guided power is  $c_g(r)^2$ , which, when normalized to the input power, is given by:

$$P_g(r) = \left( \int_r \psi_{out} \cdot \phi_g^* dx \right)^2 \quad 5.31$$

With  $P_g(r=1)=P_+$  .  $P_g(r=2)=P_x$  . As mentioned above, in our simulations we do not have the analytical expression for  $\phi_g$ . We can approximate it with the value of the field calculated by the BPM after a few propagation steps, once it is adjusted to the propagation conditions.

The normalized radiated power is defined as:

$$P_{rad} = 1 - (P_x + P_+) \quad 5.32$$

The extinction ratio at a given wavelength  $\lambda$  in decibels is defined as

$$ER(\lambda) = 10 \log \left( \frac{P_+}{P_x} \right) \quad 5.33$$

For the radiation loss we use the following convention:

$$L_R = 10 \cdot \log(1 - P_{rad}) = 10 \cdot \log((P_x + P_+)) \quad 5.34$$

Thus, when the radiation loss are null, we get  $L_R=0\text{dB}$ .

## 5.4 BPM simulations

### 5.4.1 Preliminary tests

To test the accuracy of our BPM we can simulate the propagation of the first and second order mode only in the centre region of the widened X-branch structure. From previous theory, we know that if the symmetric (even) and antisymmetric (odd) modes are excited with equal amplitudes  $\alpha_s = \alpha_a = 1$  at the input of a straight waveguide, the optical power in the first half of the device  $P_1(z)$  varies with  $z$  as  $\cos^2(\Delta\beta_c z/2)$ . If we look at the BPM plot (See Fig 5.2) it actually describes the beating between the first and second order mode. The power function  $P_1(z)$  calculated from BPM is a sinus type function (See Fig 5.3). If we calculate  $P_1(z)$  over a propagation distance about  $Z=5\text{cm}$  (See Fig 5.4), it is possible, by taking the Fourier transform of  $P_1(z)$ , to locate in the frequency spectrum a peak that corresponds to the beating frequency  $\Delta\beta_c$  (see Fig 5.5) [17] (the error in  $\Delta\beta_c$  is about  $1/Z=1/(5 \times 10^4)=2 \times 10^{-5} \mu\text{m}^{-1}$ ). To minimize the sidelobes when estimating the fourier transform of  $P_1(z)$  an Hanning window[18] can be used (See Fig 5.4).

$$FT(P_1(z)) \approx \int_0^z P_1(z) \cdot W(z) \cdot e^{-j2\pi(\Delta\beta)z} dz \quad 5.35$$

Where  $W(Z)$  is the Hanning window. A classic FFT procedure helps to solve this integral [18]. The  $\Delta\beta_c$ s calculated by the BPM are close to those calculated by the Runge-Kutta method up to the fifth digit (that is the accuracy of the Runge-Kutta method).

A second accuracy test is to calculate the phase angle due to the tapered region and compare it with the results obtained, using the Runge-Kutta method (see Chapter 3). There is a good agreement between both methods for small branching angles (see Fig 5.6).

The discrepancies between both method for larger angles can be explained by the fact that the BPM takes into account the radiation modes whereas the (EIM+ Runge Kutta) method does not (see Fig 5.7). As they appear, the radiation modes tend to reduce the isolation of the two separate channels and, when they are taken into account, the values calculated for  $\phi_1$  are larger.

Looking at Fig 5.7 we can observe that there is non negligible of light from one arm to the other in the tapered regions, especially at smaller angles. For instance, for  $\alpha=0.5^\circ$ , there is total power transfer from one arm to the other.

**Fig 5.2: Guided field propagating along a uniform two moded single waveguide with side diffused boundaries ( $t_d=270\text{min}$ ,  $w=12.0\mu\text{m}$ , the even and odd order TM modes are excited with the same amplitude at the input)**

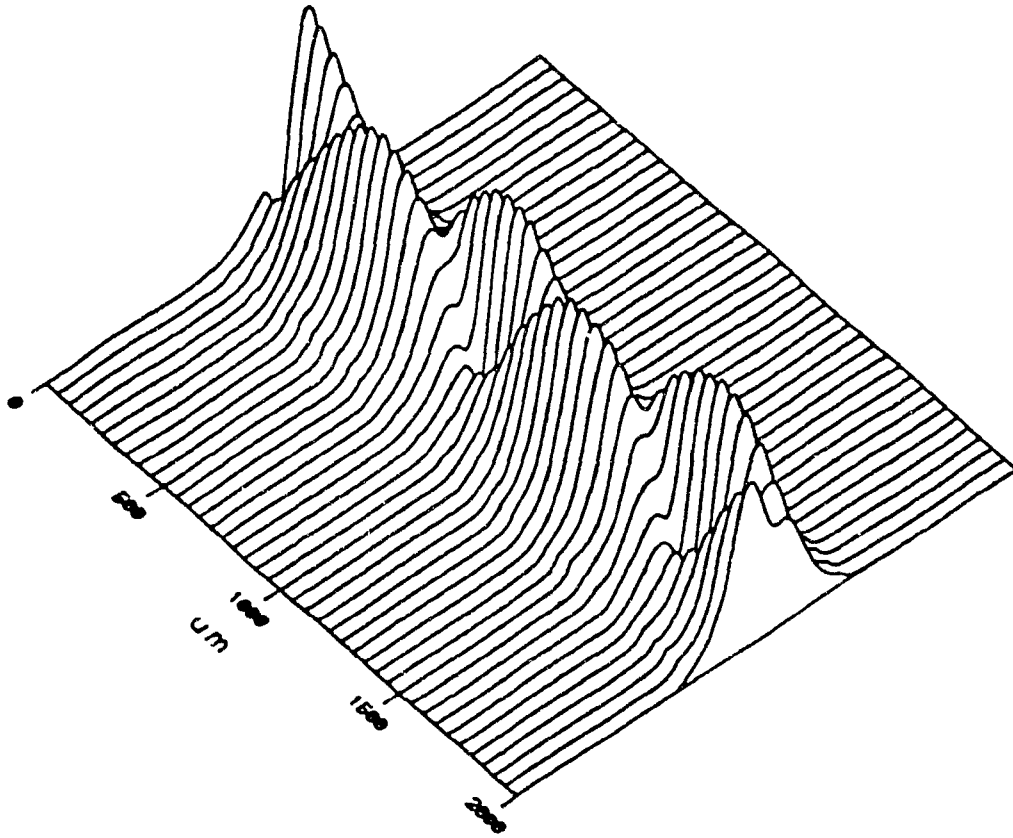


Fig 5.3: Normalized power  $P_1(z)$   
in region 1 ( $x>0$ ), ( $0<z<2000\mu\text{m}$ )  
( $\nu=0.55$  in the BPM)

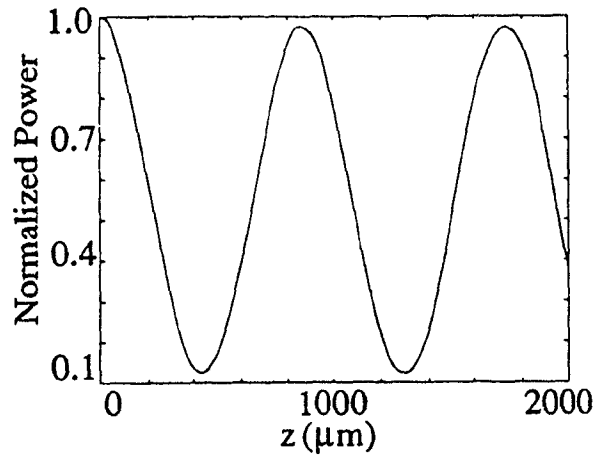


Fig 5.4:  $W(z)$  (---),  $P_1(z).W(z)$  (—)  
 $W(z)$ (Hanning window) $=1-\cos(2\pi z/Z)$   
( $z=50000\mu\text{m}, 0<z<Z$ ), ( $\nu=0.55$  in the BPM)

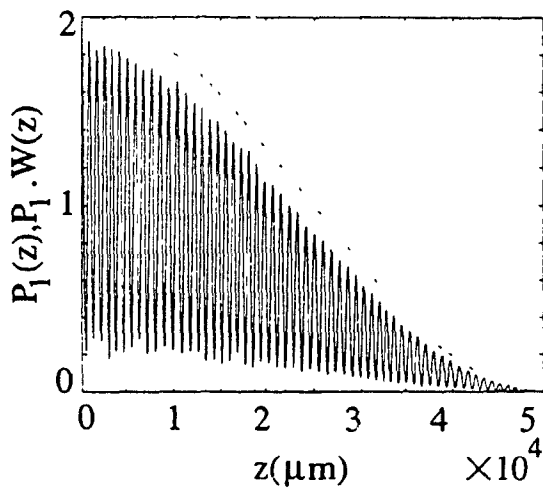


Fig 5.5: Fast Fourier Transform (FFT)  
of  $P_1(z)$

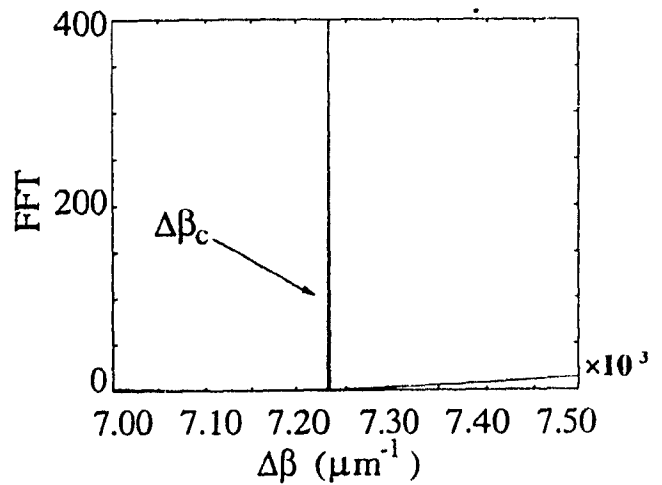
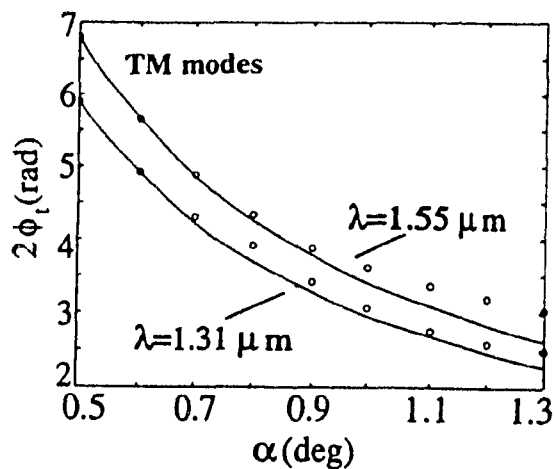
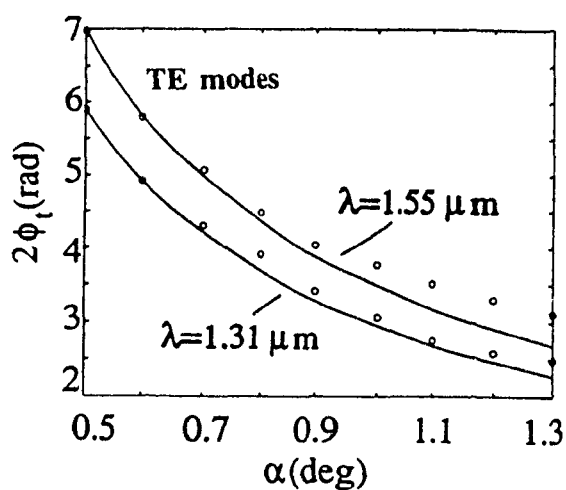


Fig 5.6a,b: Phase angle  $2\phi_t(\lambda)$  vs branching angle  $\alpha$   
 at  $\lambda=1.31, 1.55\mu\text{m}, (t_d=270\text{min}), w=6.0\mu\text{m}$

— Calculated by the Runge-Kutta method (see Chapter 4) ○○ Calculated by the BPM

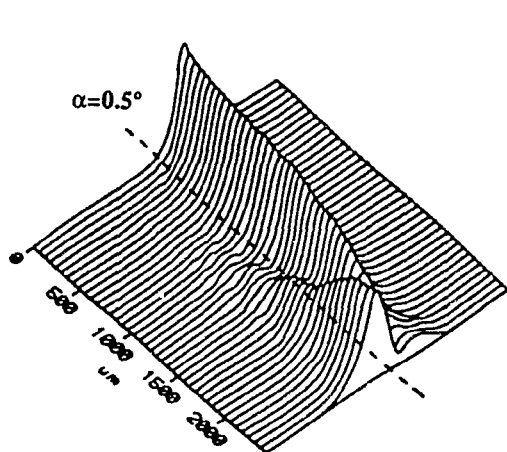


5.6a) TM modes

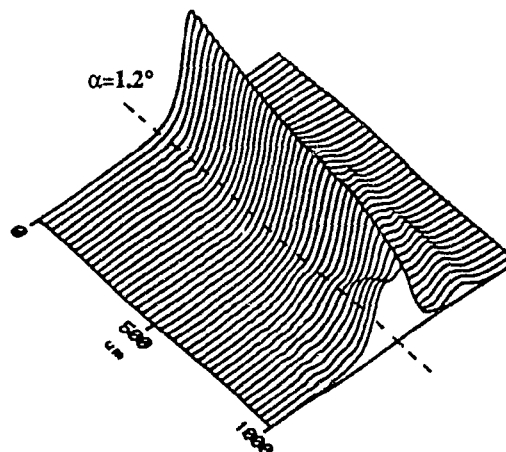


5.6b) TE modes

Fig 5.7a,b: Optical field in the tapered regions ( $w=6.0\mu\text{m}, t_d=270\text{min}, \text{TM mode}, \lambda=1.55\mu\text{m}$ )



5.7a)  $\alpha=0.5^\circ$



5.7b)  $\alpha=1.2^\circ$

### 5.4.2 Numerical results for the design of the widened X-branch

Using the EIM+BPM method to simulate the device function, we find a good agreement with the results derived in Chapter 4 using the (EIM + Runge Kutta) method, for small branching angle of the tapered regions  $\alpha=0.5^\circ$ . The difference in the diffusion time needed for the ion exchange  $t_d$ , calculated by both method is between 0 and 5 minutes (see Fig 5.8b,d). For the length of the device  $L$ , we find differences around  $30\mu\text{m}$  (see Fig 5.8a,c) This is well within the tolerance requirements. The discrepancies tend to increase when the radiation modes which are taken into account by the BPM but not the Runge-Kutta method, tend to appear (that is, for smaller  $t_d$  (See the next section) ). In most cases these discrepancies are well under the tolerance requirements. Therefore, from the design curves (5.8a,b,c,d) we can derive practical design values for the experimental part of our work. For a given width  $w$ , the length  $L$  required for a demultiplexing operation for either TM or TE polarization is about the same but the diffusion time needs to be adjusted. The device is polarization sensitive as stated in Chapter 4. BPM plots are shown Fig 5.9-5.13. The device functions are well simulated and the local normal even-odd mode interference due to the propagation phase differences can be seen clearly by the peak variations of the guided fields in the two-mode central region. The number of peaks counted at  $\lambda=1.31\ \mu\text{m}$  is the number  $n$  of coupling length  $l_c$  ( $l_c=\pi/(\Delta\beta)$ ,  $L=n.l_c$ ) needed for a demultiplexing operation. In the best case, extinction ratios of -35 dB are obtained as well as a low radiation loss (around 0.02 dB)

### 5.4.3 Radiation modes

An important point with the radiation modes is that it limits the range of possible values for the branching angle  $\alpha$ . As underlined in Chapter 3 there is a tradeoff if one wants to minimize the device length  $L$ , which decreases with larger angles and at the same time optimize the extinction ratio (ER) and radiation loss ( $L_R$ ) which decreases for a smaller angle. For a branching angle of  $\alpha=0.5^\circ$ , we obtained extinction ratio up to 40 dB for both wavelength 1.31, 1.55  $\mu\text{m}$ , whereas for a branching angle of  $\alpha=1.2^\circ$  we could not get better than 20 dB. Moreover, radiation losses up to 1.2 dB were obtained for large branching angles (see Table 5.1, Fig 5.14).

Another important point about scattering losses is that they are larger at 1.55  $\mu\text{m}$  than at 1.31  $\mu\text{m}$ , as the modes are weakly guided at this wavelength. In fact, looking at Table 5.1 and Fig 5.15 we can see that, for the given wavelength of 1.55  $\mu\text{m}$ , the closer we get to the cutoff frequency

## Chapter 5: BPM simulation of a widened X-branch demultiplexer

---

for the second order mode in the centre region (decreasing diffusion time) the more radiation losses we get, and also the more the extinction ratio is deteriorated. Indeed some radiated power is coupled back into the guided modes in both branches. The BPM plots illustrate this point

Clearly from these considerations, smaller branching angle ( $\alpha \approx 0.5^\circ$ ) and larger diffusion times should be preferred for optimum design. In fact, even for small branching angle, extinction ratios of  $-\infty$  (complete isolation of the two output waveguides), are not attainable.

### 5.4.4 Fabrication tolerances

The same fabrication tolerance study as carried out in Chapter 4 can also be performed by the BPM. Running extensive BPM computations, very little discrepancies can be found in the calculated tolerances on  $w, t_d, \lambda$ , to get an extinction ratio below -20dB, for devices with different design values  $w, t_d$ , optimized for either TE or TM polarization. The numerical results (Tables [5.2-5.5], Figs [5.15-5.18] presented here are for a device optimized for TM polarization with  $t_d = 257 \text{ min}$ ,  $w = 6.0 \mu\text{m}$ ,  $L = 3100 \mu\text{m}$ ,  $\alpha = 0.5^\circ$ .

Qualitatively the results obtained are the same as those found in Chapter 4: the device is more sensitive to width deviations at shorter wavelength and to diffusion time deviations at longer wavelength, extinction ratio degradation can be compensated by tuning the diffusion time. However, numerically, the tolerance figures predicted by the BPM, to get an extinction ratio below -20 dB, are tighter:  $\Delta(2w) \approx \pm 0.25 \mu\text{m}$  at  $\lambda = 1.55 \mu\text{m}$ ,  $\approx \pm 0.1 \mu\text{m}$  at  $\lambda = 1.31 \mu\text{m}$ ;  $\Delta t_d \approx \pm 3 \text{ min}$  at  $\lambda = 1.55 \mu\text{m}$ ,  $\approx \pm 5 \text{ min}$  at  $\lambda = 1.31 \mu\text{m}$  and;  $\Delta \approx \pm 0.01 \mu\text{m}$  at  $\lambda = 1.55 \mu\text{m}$ ,  $\approx \pm 0.015 \mu\text{m}$  at  $\lambda = 1.31 \mu\text{m}$ . These figures are believed to be more accurate than those presented Chapter 4, since the effect of the radiation modes is taken into account by the BPM (See previous section)

## 5.5 Conclusion

In this chapter we have presented the powerful and accurate numerical beam propagation method for solving the wave equation and its application in integrated optics. It helped us to accurately simulate the device function of our widened X-branch. The effect of radiation modes was also investigated.

Fig 5.8a,b,c,d: L and  $t_d$  vs w (TE, TM modes,  $\alpha=0.5^\circ$ )

— Calculated by the Runge-Kutta method ○○○ Calculated by the BPM

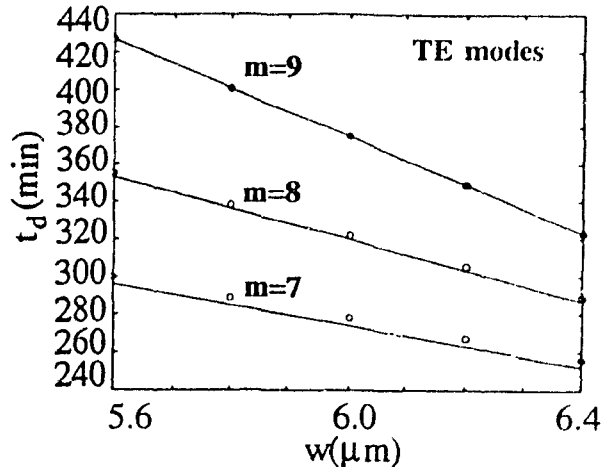
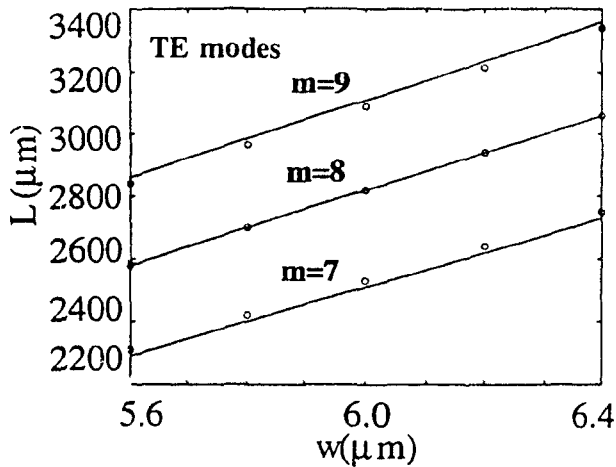
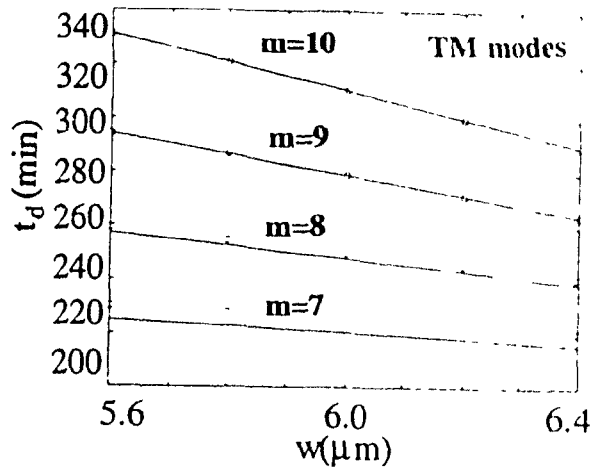
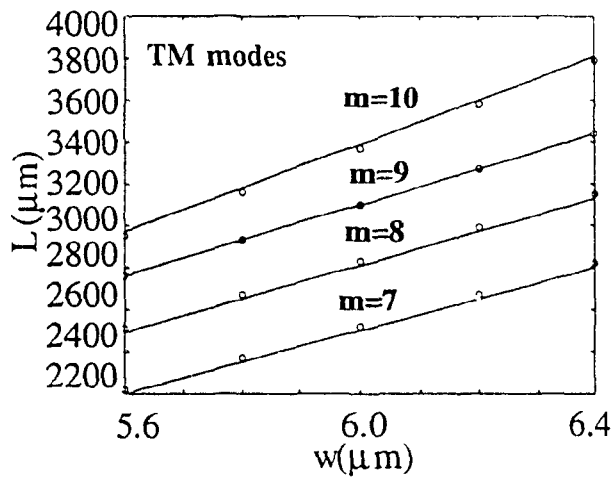
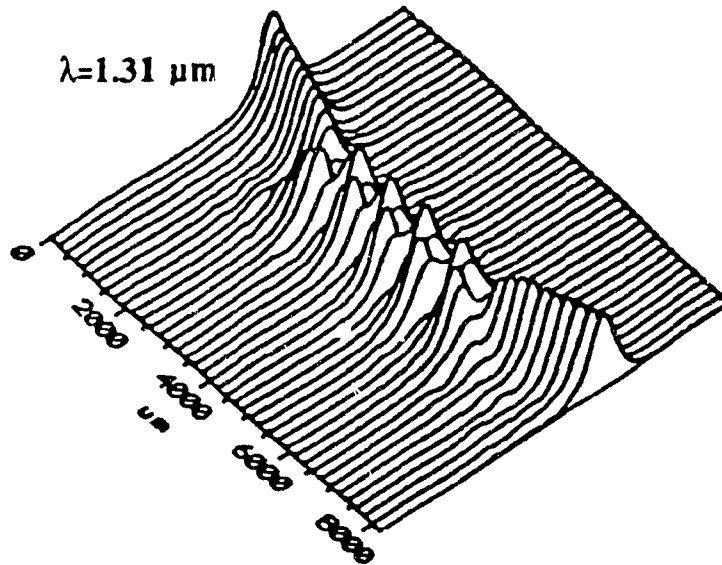
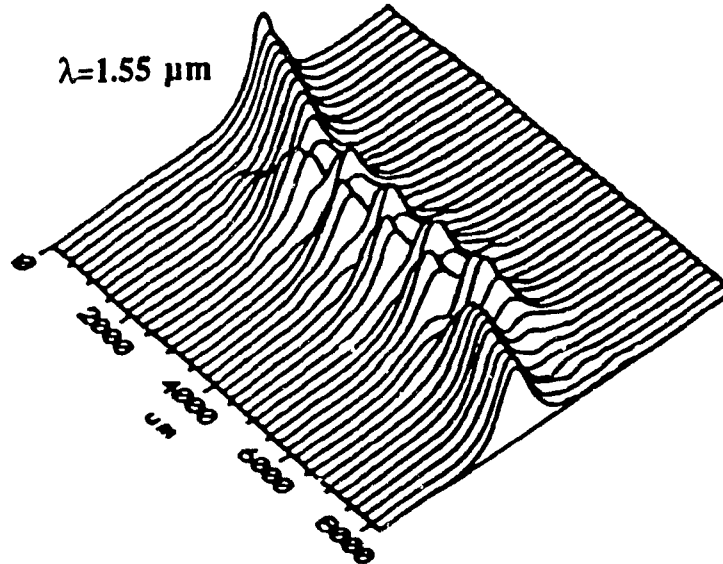


Fig 5.9: BPM simulation of the widened X-branch demultiplexer.

$m=10, t_d=287\text{min}, L=3370\mu\text{m}, w=6.0\mu\text{m}, \alpha=0.5^\circ, \text{TM modes}$

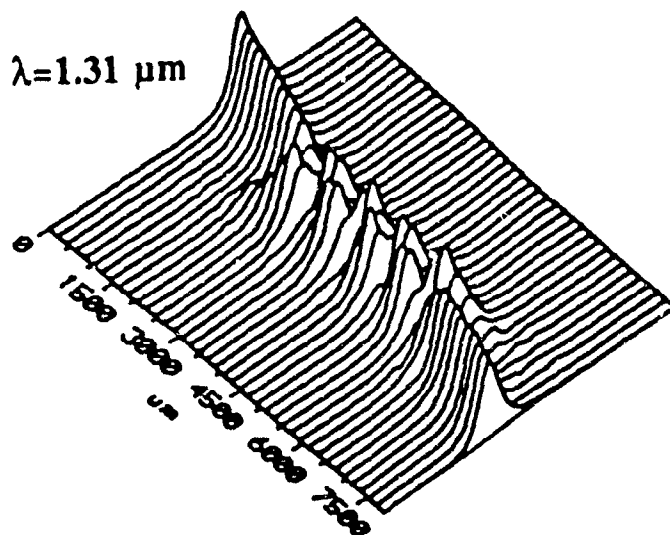


5.9a)  $\lambda=1.31\mu\text{m}, \text{ER}=-35\text{dB}, L_R=-0.016\text{dB}$

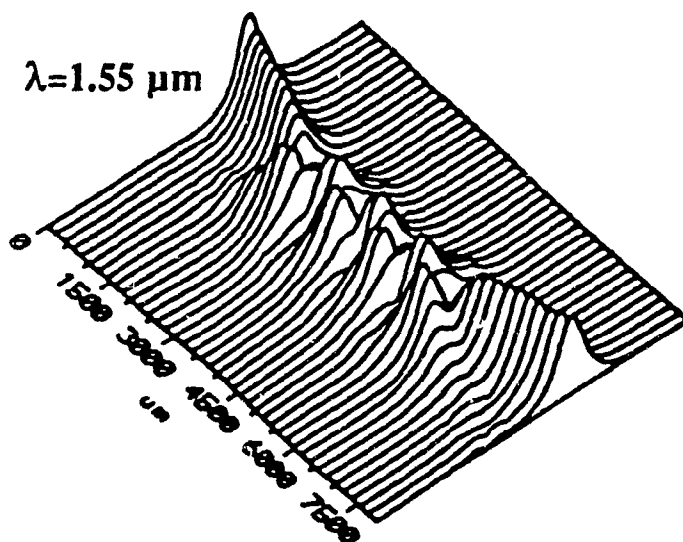


5.9b)  $\lambda=1.55\mu\text{m}, \text{ER}=-35\text{dB}, L_R=-0.017\text{dB}$

Fig 5.10: BPM simulation of the widened X-branch demultiplexer.  
 $m=9, t_d=257\text{min}, L=3100\mu\text{m}, w=6.0\mu\text{m}, \alpha=0.5^\circ, \text{TM modes}$



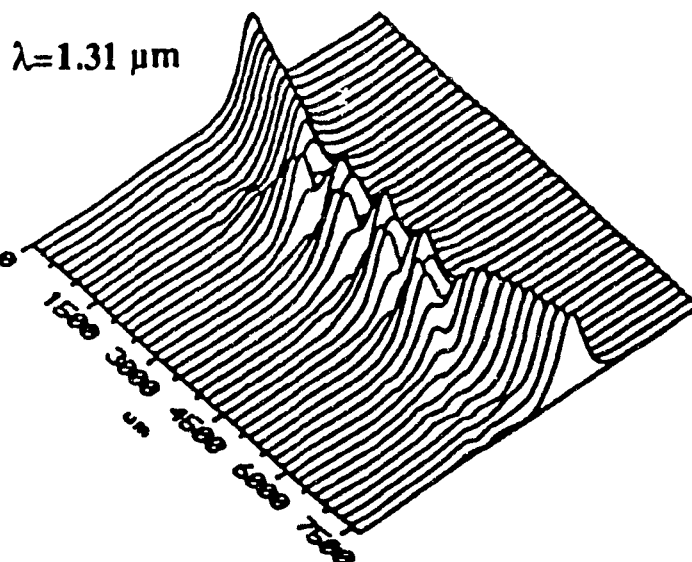
5.10a)  $\lambda=1.31\mu\text{m}, \text{ER}=-35\text{dB}, L_R=-0.016\text{dB}$



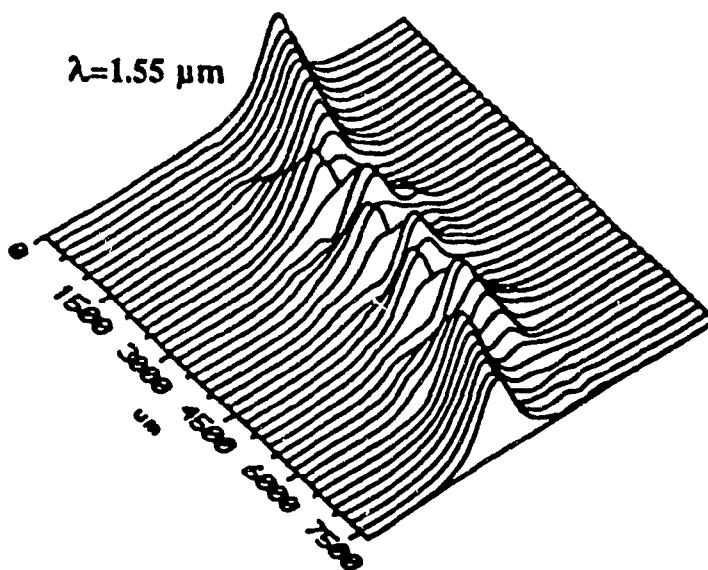
5.10b)  $\lambda=1.55\mu\text{m}, \text{ER}=-35\text{dB}, L_R=-0.019\text{dB}$

Fig 5.11: BPM simulation of the widened X-branch demultiplexer.

$m=8, t_d=232\text{min}, L=2830\mu\text{m}, w=6.0\mu\text{m}, \alpha=0.5^\circ, \text{TM mode}$



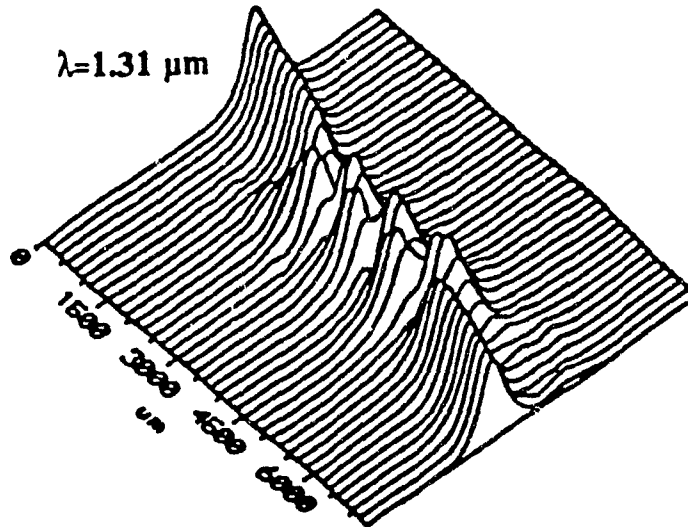
5.11a)  $\lambda=1.31\mu\text{m}, ER=-35\text{dB}, L_R=-0.016\text{dB}$



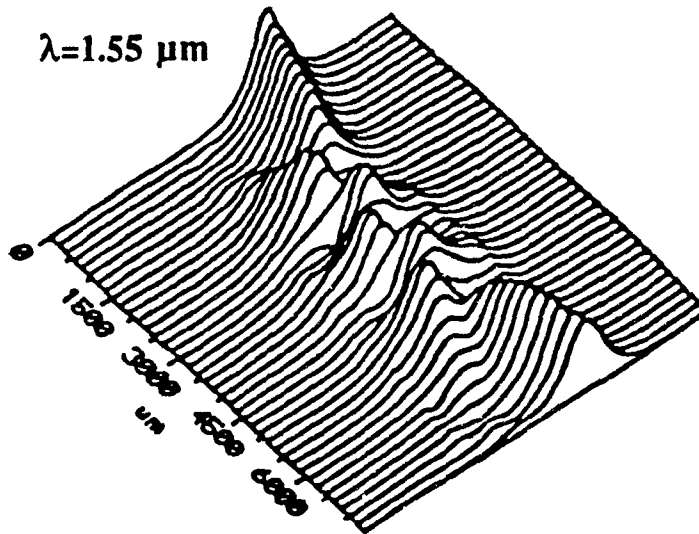
5.11b)  $\lambda=1.55\mu\text{m}, ER=-30\text{dB}, L_R=-0.037\text{dB}$

Fig 5.12: BPM simulation of the widened X-branch demultiplexer.

$m=7, t_d=209\mu\text{m}, L=2570\mu\text{m}, w=6.0\mu\text{m}, \alpha=0.5^\circ, \text{TM modes}$

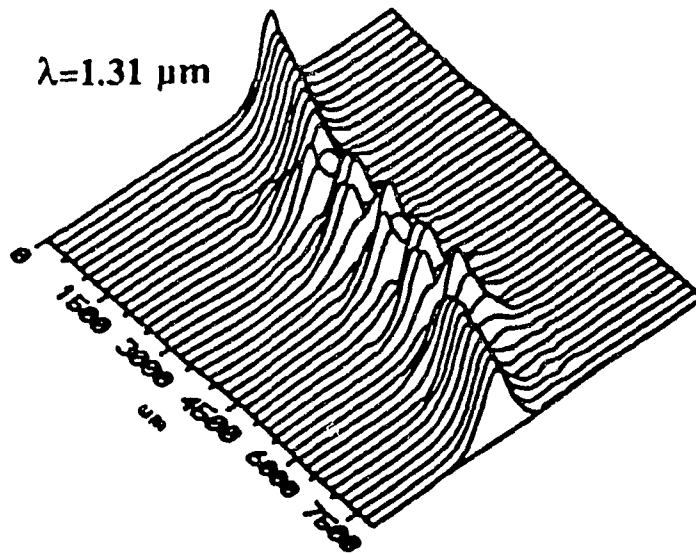


5.12a)  $\lambda=1.31\mu\text{m}, ER=-35\text{dB}, L_R=-0.024\text{dB}$

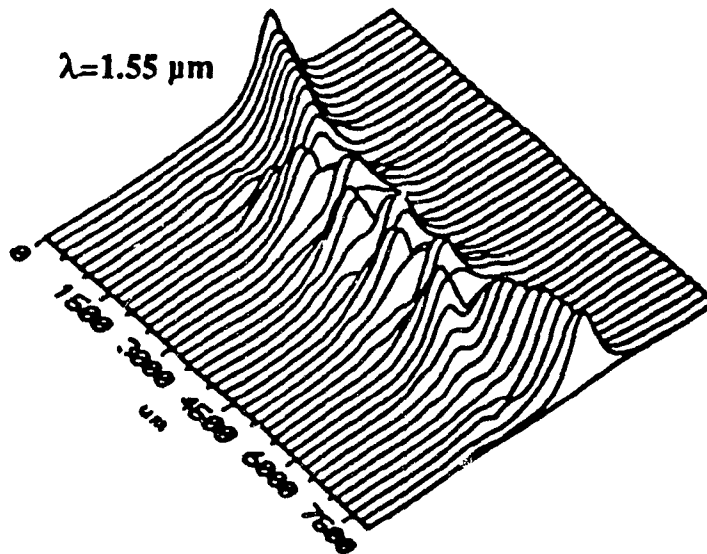


5.12b)  $\lambda=1.55\mu\text{m}, ER=-22\text{dB}, L_R=0.052\text{dB}$

Fig 5.13: BPM simulation of the widened X-branch demultiplexer.  
 $m=10, t_d=375\text{min}, L=3140\mu\text{m}, w=6.0\mu\text{m}, \alpha=0.5^\circ, \text{TE modes}$



5.13a)  $\lambda=1.31\mu\text{m}, ER=-35\text{dB}, L_R=-0.018\text{dB}$



5.13b)  $\lambda=1.55\mu\text{m}, ER=-35\text{dB}, L_R=-0.029\text{dB}$

Table 5.1a,b: ER( $\lambda$ ) and  $L_R(\lambda)$  vs branching angle  $\alpha$

$\alpha$ (deg)	ER(dB) $\lambda=1.31\mu\text{m}$	ER(dB) $\lambda=1.55\mu\text{m}$	$P_{\text{out}}/P_{\text{in}}$ (%) $\lambda=1.31\mu\text{m}$	$P_{\text{out}}/P_{\text{in}}$ (%) $\lambda=1.55\mu\text{m}$	$L_R$ (dB) $\lambda=1.31\mu\text{m}$	$L_R$ (dB) $\lambda=1.55\mu\text{m}$
0.5°	-35	-35	96.5	95.5	-0.015	-0.020
0.8°	-35	-35	95	93.5	-0.023	-0.029
1.2°	-35	-28.5	83	75	-0.087	-0.12

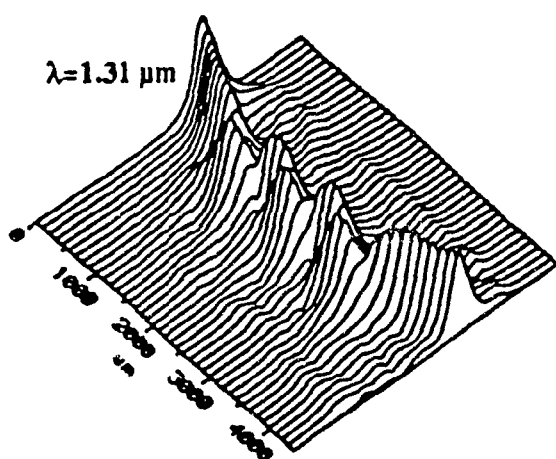
Tab 5.1a)  $w=6.0\mu\text{m}$ , (TM modes). (For each angle  $t_d$  is chosen around 270 nm)

$\alpha$ (deg)	ER(dB) $\lambda=1.31\mu\text{m}$	ER(dB) $\lambda=1.55\mu\text{m}$	$P_{\text{out}}/P_{\text{in}}$ (%) $\lambda=1.31\mu\text{m}$	$P_{\text{out}}/P_{\text{in}}$ (%) $\lambda=1.55\mu\text{m}$	$L_R$ (dB) $\lambda=1.31\mu\text{m}$	$L_R$ (dB) $\lambda=1.55\mu\text{m}$
0.5°	-35	-30	96.4	92	-0.016	-0.037
0.8°	-35	-30	90	90	-0.046	-0.046
1.2°	-30	-26	90	69	-0.046	-0.16

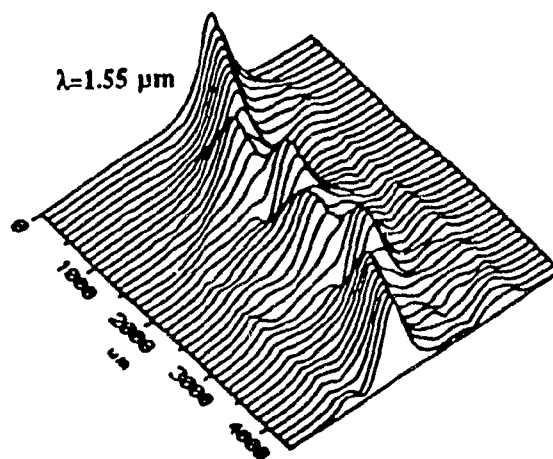
Tab 5.1b)  $w=6.0\mu\text{m}$ , (TM modes). (For each angle  $t_d$  is chosen around 230 nm)

Fig 5.14: BPM simulation of the widened X-branch demultiplexer.

$m=10, t_d=227\text{nm}, L=2400\mu\text{m}, w=6.0\mu\text{m}, \alpha=1.2^\circ$ , TM modes



5.14a)  $\lambda=1.31\mu\text{m}, ER=-35\text{dB}, L_R=-0.087\text{dB}$



5.14b)  $\lambda=1.55\mu\text{m}, ER=-28.5, L_R=-0.12\text{dB}$

**Tab 5.2, Fig 5.15: ER vs  $\Delta(2w)$  waveguide width deviation**

(Device design parameters  $w=6.0\mu\text{m}, t_d=257 \text{ min}, L=3100\mu\text{m}, \alpha=0.5^\circ, \text{TM modes}$ )

(x x x  $\lambda=1.31\mu\text{m}$  . . .  $\lambda=1.55 \mu\text{m}$ )

$\Delta t_d(\text{min})$	ER(dB)	
	$\lambda=1.55\mu\text{m}$	$\lambda=1.31\mu\text{m}$
-10	-9	-12
-8	-11.5	-15
-6	14	-18.5
-4	-17	-22.5
-2	-22	-29.5
0	-35	-35
+2	-26	-31
+4	-19	-23
+6	-15	-20
+8	-13	-17
+10	-11	-14

Tab 5.2

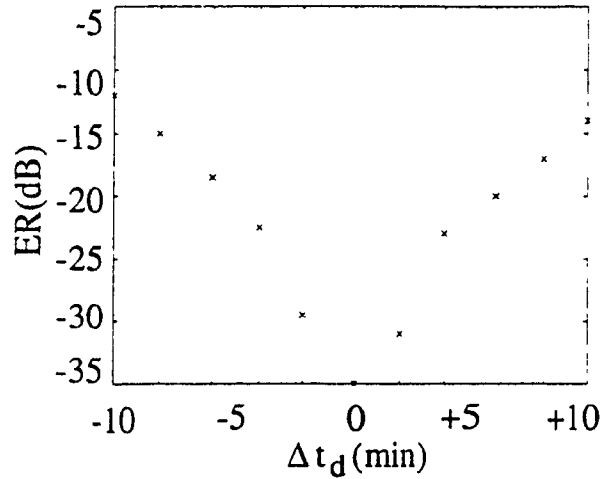


Fig 5.15

**Tab 5.3, Fig 5.16 : ER vs  $\Delta t_d$  diffusion time deviation**

(Device design parameters  $w=6.0\mu\text{m}, t_d=257 \text{ min}, L=3100\mu\text{m}, \alpha=0.5^\circ, \text{TM modes}$ )

(x x x  $\lambda=1.31\mu\text{m}$  . . .  $\lambda=1.55 \mu\text{m}$ )

$\Delta(2w)(\mu\text{m})$	ER(dB)	
	$\lambda=1.55\mu\text{m}$	$\lambda=1.31\mu\text{m}$
-0.6	-8	-2
-0.5	-10	-4
-0.4	-12.5	-7
-0.3	-17	-10
-0.2	-21.5	-13
-0.1	-27.5	-18
0	35	-35
+0.1	26	-20
+0.2	-19.5	-14
+0.3	-16.5	-10.5
+0.4	-13.5	-7.5
+0.5	-11.5	-3.5
+0.6	9.5	-1.5

Tab 5.3

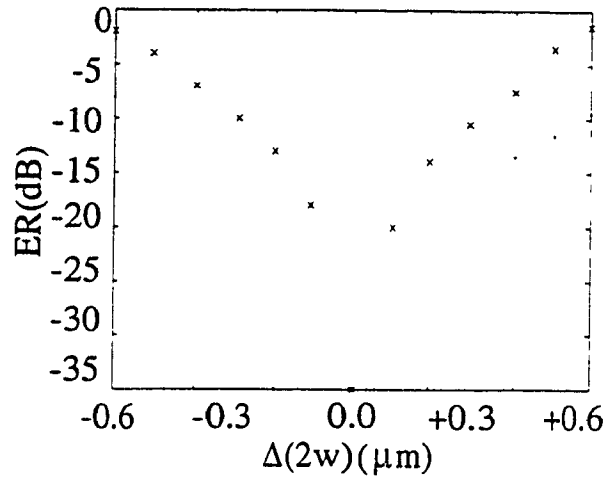


Fig 5.16

Tab 5.4, Fig 5.17 : ER vs  $\Delta t_d$  diffusion time deviation when an error of  $-0.2\mu\text{m}$  is assumed on the central width  $2w$  (Device design parameters  $w=6.0\mu\text{m}, t_d, 257 \text{ min}, L=3100\mu\text{m}, \alpha=0.5^\circ$ , TM modes) ( $x \times x \lambda=1.31\mu\text{m} \dots \lambda=1.55 \mu\text{m}$ )

$\Delta t_d(\text{min})$	ER(dB) $\lambda=1.55\mu\text{m}$	ER(dB) $\lambda=1.31\mu\text{m}$
-10	-12	-30
-8	-15	-35
-6	-19	-24
-4	-26	-19
-2	-35	-16
0	-22	-14.5
+2	-17	-12.5
+4	-13.5	-11
+6	-11.5	-9.5
+8	-9.5	-8.5
+10	-8	-8

Tab 5.4

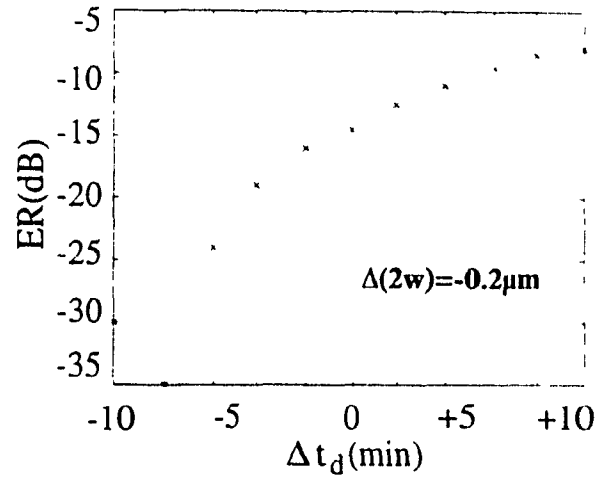


Fig 5.17

Tab 5.5, Fig 5.18 : ER vs wavelength deviation  $\Delta\lambda$   
(Device design parameters  $w=6.0\mu\text{m}, t_d, 257 \text{ min}, L=3100\mu\text{m}, \alpha=0.5^\circ$ , TM modes)  
( $x \times x \lambda=1.31\mu\text{m} \dots \lambda=1.55 \mu\text{m}$ )

$\Delta\lambda(\mu\text{m})$	ER(dB) $\lambda=1.55 \mu\text{m}$	ER(dB) $\lambda=1.31 \mu\text{m}$
-0.05	-7	-11.5
-0.04	-9	-13
-0.03	-11	-15.5
-0.02	-15	-19.5
-0.01	-23	-26
0	-35	-35
+0.01	-23	-24
+0.02	-16.5	-18
+0.03	-13	-14.5
+0.04	-11	-12.5
+0.05	-9.5	-9.2

Tab 5.5

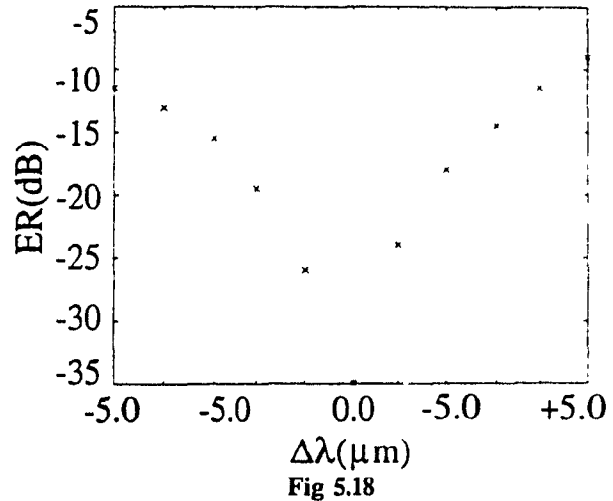


Fig 5.18

**References**

- [1] M. D. Feit and J. A. Fleck, "Light propagation in graded index optical fiber", *Applied Optics*, Vol 17, n°17, pp.3990-3998, 1978.
- [2] B. Hermansson, D. Yevick and Danielsen, "Propagation beam analysis of multimode waveguide tapers", *IEEE J. of Quantum Electronics*, Vol 19, n°8, pp.1146-1251, 1983.
- [3] R. Baets and P. E. Lagasse, "Loss calculation and design of arbitrarily curved integrated optic waveguides", *J. Opt. soc. Am.*, Vol 73, n°2, pp.177-162, 1983.
- [4] J. Saijonmaa and D. Yevick, "Beam propagation analysis of loss in bent optical waveguides and fibers", *J. Opt. Soc. Am.*, Vol 73, n°12, pp.1785-1791, 1983.
- [5] D. Yevick and L. Thylen, "Analysis of gratings by the beam propagation method", *J. Opt. Soc. Am.*, Vol 7, n°8, pp.73-79, 1990.
- [6] D. Yevick and L. Thylen, "Analysis of rib waveguides and couplers by the beam propagating method", *J. Opt soc Am*, Vol 7, n°1, pp.73-79, 1990.
- [7] R. Baets and P. E. Lagasse, " Calculation of radiation loss in integrated optic tapers and Y-junctions", *Applied Optics*, Vol 21, n°11, pp.1972-1978, 1981.
- [8] M. S. Bajbus, G. L. Yip and N. Goto, "BPM design optimization and experimental improvement of a Ti: LiNbO<sub>3</sub> ridge waveguide linear mode confinement modulator", *IEEE J. of Lightwave Technology*, Vol 8, pp.1742-1749, 1990
- [9] L. Thylen, E. M. wright, G. I. Stegeman, C. T. Seaton and J. V. Moloney, "Beam propagation method analysis of a nonlinear directional coupler", *Optics Letters*, Vol 11, n°11, pp.739-741, 1986.
- [10] A. Neyer, W. Mevenkamp, L. Thylen and B. Lagerstrom, "A beam propagation method analysis of active and passive waveguide crossings", *IEEE J. of Lightwave Technology*, Vol LT-3, n°6, pp.635-642, 1985
- [11] M. D. Feit and J. A. Fleck, "An analysis of intersecting diffused channel waveguides", *IEEE J. of Quantum Electronics*, Vol 21, pp.1799-1804, 1985.
- [12] Y. Chung, J. C. Yi, S. H. Kim, S. S. Choi, " Analysis of a tunable two mode interference wavelength division multiplexer-demultiplexer", *IEEE J. of Lightwave Technology*, Vol LT-6, n°5, pp 766-776, 1989

## Chapter 5: BPM simulation of a widened X-branch demultiplexer

---

- [13] Y. Chung and N. Dagi, "An assessment of finite difference beam propagation method", IEEE J. of Quantum Electronics, Vol 26, n°8, pp.1335-1339, 1990.
- [14] W. Huang, C. Xu, S. T. Chu and S. K. Chaudhuri, "A vector beam propagation method for guided wave optics", IEEE Photonics Technology Letters, Vol 3, n°10, pp.910-913, 1991.
- [15] W. Huang, C. Xu, S. T. Chu and S. K. Chaudhuri, "The finite difference vector beam propagation method: analysis and assessment", IEEE J. of Lightwave Technology, Vol LT-10, n°3, 1992.
- [16] G. R. Hadley, "Transparent boundary condition for beam propagation", Opt. Letters, Vol 16, n°9, pp.624-626, 1991.
- [17] M. D. Feit and J. A. Fleck, "Computation of mode eigenfunctions in graded-index optical fibers by the propagating beam method", Applied optics, Vol 19, n°10, pp.2241-2247, 1980.
- [18] E. O. Brigham, "The Fast Fourier transform and its applications", Englewood Cliffs, Prentice Hall, pp180-195.

## CHAPTER 6

### EXPERIMENTAL STUDY

After completion of the design simulations we took on the task to actually fabricate and test some widened X-branch demultiplexers. The generally established photolithographic techniques and measurement procedures were used. This Chapter summarizes the experimental part of our work. In Section 6.1 we will explain how the photolithographic mask was designed. In 6.2 the fabrication process will be described. The measurement procedure and experimental results are to be presented in the last section.

#### 6.1 The photolithographic mask design

A photolithographic mask, bearing the design waveguide structure, is expensive. Therefore, one should be careful when designing it. In this chapter the notations introduced in Section 4 Chapter 4 are used. The channel width in the central region is noted  $2w_c$  and the channel width in the tapered region is noted  $w_t$ . One of the problem we had to consider in the design of our mask was the low reproducibility of the photolithographic technique, when compared to the tight requirements on the channel width of the widened X-branch demultiplexer in the tapered and central regions (See Fig 5.15, Chapter 5). For each batch of samples fabricated (4-5 samples), the channel widths  $2w_c$ ,  $w_t$  actually obtained for the diffusion mask opening on the sample after photolithography, could be very different from the width specified on the photomask used (error up to  $0.8 \mu\text{m}$ ). For specified values of  $2w_c=2w=12.0\mu\text{m}$ ,  $w_t=w=6.0\mu\text{m}$  on the photomask we could

## Chapter 6: Experimental study

---

get on the sample actual widths of any value between  $12.8\mu\text{m}$  and  $11.2\mu\text{m}$  for  $2w_c$ , and  $5.2\mu\text{m}$  and  $6.8\mu\text{m}$  for  $w_t$ . Unfortunately, from the design study (See Fig 5.8 Chapter 5), we know that for each change in  $2w_c$  and  $w_t$ , the length  $L$  of the widened X-branch should be adjusted for optimized device performances. If we had designed a photomask with only one device pattern of given length  $L$ , we would have had to dispose most of the samples after the photolithography, since the channel width obtained would have not been matched to the length  $L$ . To speed up the experimental process, we designed a photomask with three devices with the same waveguide width  $6.0\mu\text{m}$  and adjusted values for the length  $L$  optimized for TM modes, assuming respectively an error in  $w_t$  and  $2w_c$  of  $0.0, -0.4, -0.8\mu\text{m}$  (D1, D2, D3 on Fig 6.1). Thus, after completion of the photolithographic process for one batch of samples, we could expect to have on each sample at least one device pattern, among the three, that was close to optimum design. Using this mask we were also able to test devices with different design parameters. The length  $L_1$  of the device D1 was taken from the design computations presented in Chapter 5 ( See Fig 5.8). D1 was designed for the case when no error was made in the channel width due to the photolithographic process:  $2w_c=12.0\mu\text{m}$ ,  $w_t=6.0\mu\text{m}$ , looking at the curve  $m=9$  for TM polarization,  $\alpha=0.5^\circ$ , in Fig 5.8a, we found  $L_1=3100\mu\text{m}$ , the corresponding diffusion time for the ion-exchange was  $t_d=255$  min (See Fig 5.8b). The design of  $L_2$  and  $L_3$  required additional computations. Indeed, when designing D2 and D3, we just mentioned, that the errors made on the specified  $2w_c$  and  $w_t$  due to the imperfections of the photolithography, were assumed to be the same (which is reasonable if the photolithographic process is uniform along the longitudinal direction). As derived in Chapter 4 (eqn 4.32) this means that on the sample one actually gets  $2w_c \neq 2w_t$  (or  $w_c \neq w_t$ ). For instance, if an error of  $-0.4\mu\text{m}$  is assumed in the specified width  $2w_c$ ,  $w_t$ , one actually gets  $2w_c=12-0.4=11.6\mu\text{m}$ ,  $w_c=5.8\mu\text{m}$  whereas  $w_t=6-0.4=5.6\mu\text{m} \neq w_c$ . Therefore, the values for the length  $L_2$ ,  $L_3$  of the devices D2, D3 (adjusted values when an error in the specified width of  $-0.4$  and  $-0.8\mu\text{m}$  was made) were not exactly  $L(2w_c=2w_t, w_t=w_c)$  as taken from Fig 5.8 in Chapter 5, where we assumed  $w_c=w_t$ . Instead, we chose slightly corrected values (calculated by the BPM)  $L(2w_c=2w_t, w_t \approx w_c)$ , which was more rigorous. We found  $L_2=2930\mu\text{m}$  (for  $m=9, \alpha=0.5^\circ, t_d=270\text{min}$ , TM modes),  $L_3=2710\mu\text{m}$  (for  $m=9, \alpha=0.5^\circ, t_d=280\text{min}$ , TM modes). The value found for  $L_3$  was also calculated to be an adjusted value of the length, when an error of  $-0.2\mu\text{m}$  was made in the specified widths  $2w_c, w_t$ , if the diffusion time of the ion exchange was

## Chapter 6: Experimental study

chosen to be  $t_0=255 \text{ nm}$  ( $m=8, \alpha=0.5^\circ$ , TM modes)

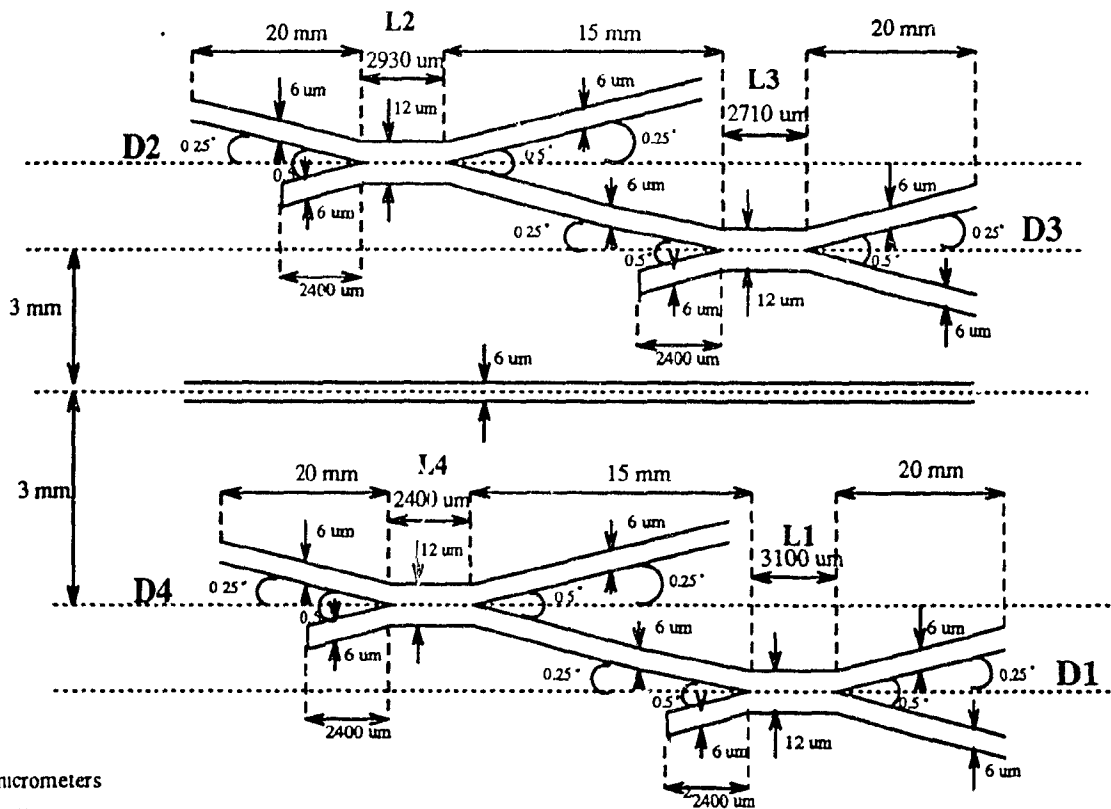
Besides D1, D2 and D3 there were two other device patterns on the photomask

-The device D4 was first designed for TE mode operation, but we did not use in this experimental study. In our experimental work we studied only TM modes.

-A single channel waveguide (specified width on the mask:  $6.0 \mu\text{m}$ ) was also added. This pattern was just used as a test pattern.

The fact that before extinction measurement we had to cut the samples was also considered when designing the mask (see section 6.2.6)

Fig 6.1: Photolithographic mask



$\mu\text{m}$  = micrometers  
 $\text{mm}$  = millimeters

## 6.2 The fabrication process

### 6.2.1 Substrate cleaning

The substrates used in the experiments were ordinary microscope slides made of soda lime silicate glass. Manufactured by the Fisher Scientific and Co, the slide measure 75mmx25mmx1mm and has a good surface quality. The main advantage in using this type of substrate is that it is very cheap. It is not of high enough optical quality to be used as the substrate for the demanding low-loss performances of commercial IO devices but is ideal for research purposes.

The microscope slides are packed pre-cleaned in sealed boxes but they must be cleaned thoroughly in a clean room environment if they are to be used as substrates. This step is compulsory to avoid contamination of the melt and subsequent diffusion of foreign impurities into the waveguide layer. In addition, the surface must be defect-free because imperfections as small as a fraction of a wavelength of the light source can cause scattering losses. The cleaning procedures were performed in a suitable clean-room environment. The slides were rinsed in flowing deionized (D.I.) water (10Mohm) and then blown dry with nitrogen, Using soft cotton swabs, they were cleaned in a non-abrasive Sparkleen detergent solution and rinsed again with DI water. Then, they were placed in an aluminium holder for further cleaning steps that included:

- 1) a three-minute wash in an ultrasonic bath containing a few grains of detergent in 300 ml of D.I water.
- 2) a rinse in flowing D.I. water
- 3) a three-minute ultrasonic wash in D.I water
- 4) an organic cleaning which consisted of placing the holder in an empty beaker containing 20ml of propanol and then placing the breaker for three-minutes in the ultrasonic bath. The cleansing action of propanol is effective for organic decontamination
- 5) a final rinse in D.I. water

To finish the cleaning job, the samples were blown dry with nitrogen and put into the oven at 80°C for 15 minutes.

### 6.2.2 Metallization

After cleaning and baking the substrates in an oven, we performed the metallization of the samples which forms the preliminary step to the photolithographic process. The technique used was aluminium evaporation which is a relatively simple procedure (compared to sputtering for instance). This process was performed in a vacuum station at a pressure around  $5 \cdot 10^{-6}$  Torr by heating 2 tungsten hooks on which a 10 to 20 cm long Al wires (high purity (Marz Grade) furnished by MRC Corp.) had been suspended. Upon heating the wires, by passing a high current through, the aluminium evaporated in the vacuum enclosure. A part of the evaporated aluminium landed and became condensed on the glass slide as a very uniform film, thick enough to block the diffusion process (thickness  $\approx 10$  to  $20 \mu\text{m}$ ).

### 6.2.3 Photolithography

After metallization, to remove the aluminium from the waveguide pattern, where the exchange was to take place, we followed the following steps in a clean-room environment:

#### 1) Photoresist coating

First a 4:1 mixture of photoresist (Shipley) and thinner (Shipley AZ) was deposited onto the aluminium surface by spinning the substrate at 4000 RPM for 20 seconds and baking the resulting film for 30 minutes at  $80^\circ\text{C}$  (pre-baking).

#### 2) UV-exposure

After prebaking, the photolithographic mask was used to expose the resist to UV light through the mask opening for 80-90 seconds. Under or over exposure would lead to an ill defined pattern after exposition.

#### 3) Development

Development of the resist was done in a 3:2 mixture of Mirroposit developer and D.I. water for 60-75 seconds (depending on the freshness of the solution), resulting in the removal of the resist from the exposed areas. After that, the substrate was baked for 30 minutes at  $120^\circ\text{C}$  to harden the resist pattern.

The development is the most delicate part of the fabrication process. The waveguide width obtained on the sample when the photolithographic stage is complete strongly depends on the

## Chapter 6: Experimental study

---

development conditions like the solution freshness or dilution, or the developing time. To insure the reproducibility of the process one should keep the developer solution as fresh as possible by stowing it in the refrigerator, and use a diluted solution (See above for dilution ratio). That way, the developing process is slowed down and becomes more controllable

Despite these precautions small variations (around 5 to 15 s) in the developing time can result in large variations for the waveguide width (0.4  $\mu\text{m}$  to 1  $\mu\text{m}$ !). A good way to get the right width is to make two or three batches of samples the same day, trying to adjust the developing time, from the results obtained for the previous batch. The photoresist pattern observed under the microscope should be well defined and with smooth edges as the one shown Fig 6.2.

**Fig 6.2: Resist pattern (after developing)**



## Chapter 6: Experimental study

---

### 4) Etching

After the development and postbaking, the aluminium was etched away from the areas where the resist was previously removed by immersion in a solution of phosphoric acid, nitric acid, acetic acid and D.I. water (16:1:2:1) for 2-10 minutes (depending on the freshness of the solution). To check this process, the patterns were observed under a microscope at the end. We made sure that they were free of residual particles and well defined (See Fig 6.3).

### 5) Resist removal

Finally, the photoresist which was used as a mask against the etchant was removed by dissolution in a remover solution (Microposit remover diluted with DI water 1:1). In preparation for the ion exchange, the substrate was dipped in a D.I. water bath, blown dry gently and placed inside an oven.

**Fig 6.3: Al diffusion mask pattern  
(after etching and resist removal)**



### 6.2.4 The channel-guide width measurement

Before proceeding to the ion-exchange, we wanted to measure for each sample the channel width in the central region of the three devices D1,D2,D3 that were on the pattern (See Fig 6.1 for the pattern). To perform our measurements, we used a diffraction method (See Fig 6.4). The samples to be measured were mounted on a x-z micropositionner, and a laser beam was shone through the mask opening of the waveguides. On the screen, we could see the one dimensional diffraction pattern. The light intensity follows the well known approximation (diffraction by a narrow aperture, infinitely long in one direction):

$$I(x) = I_0 \text{sinc}^2\left(\frac{\pi \cdot 2w_c \cdot \sin[\text{Arctg}(x/d)]}{\lambda}\right) \quad \text{where} \quad \text{sinc}(X) = \frac{\sin(X)}{X} \quad 6.1$$

The minima of intensity correspond to the values such that

$$\frac{\pi \cdot 2w_c \cdot \sin[\text{Arctg}(X_m/d)]}{\lambda} = m\pi \quad \text{where } m \text{ is an integer} \quad 6.2$$

In practice, only the first two minima on each side of the pattern ( $m=\pm 1$ ,  $m=\pm 2$ ) were visible because the power of our laser source was limited.

Measuring  $X_{m=\pm 1, \pm 2}$  with a ruler gave us four values of the waveguide width  $w_c$  by inverting eqn(6.2):

$$2w_c = \frac{\lambda m}{\sin[\text{Arctg}(X_m/d)]} \quad 6.3$$

( with  $X_m \ll d$ , a rough expression for  $w$  is  $w \approx \lambda d / X_m$  ).

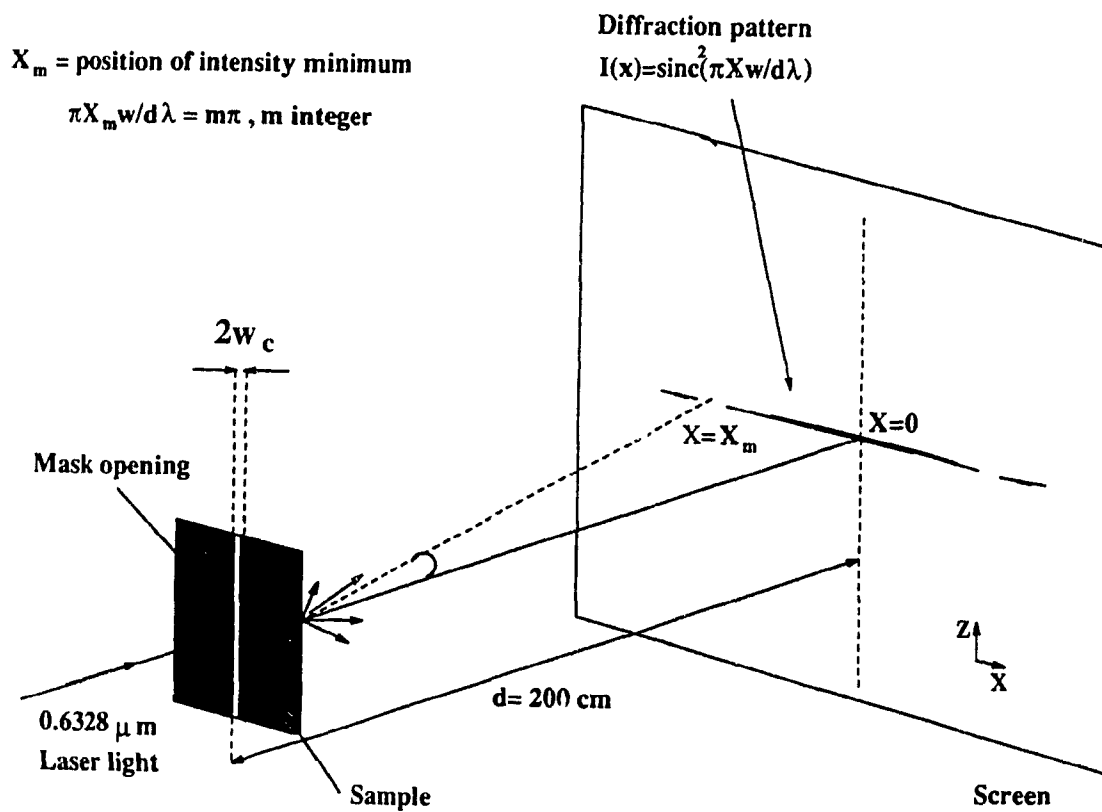
Averaging these two values ( trying to minimize the error), we found  $w_c$ . The exact minima were difficult to locate, the uncertainty on each  $X_m$  was around  $\pm 0.25\text{cm}$  and  $\pm 0.5\text{cm}$ . Therefore, the resulting uncertainty on  $2w_c$  was  $\Delta(2w_c) = \lambda d (\Delta(X_m)) / X_m^2$ . With  $\lambda = 0.6328 \mu\text{m}$  and  $d = 200 \text{ cm}$  and  $X_m \approx 9 \text{ cm}$ , we got  $\Delta(2w) \approx 0.4 - 0.8 \mu\text{m}$ .

By averaging on the 4 values, we can expect to reduce the error in the width measurement to a value around  $0.2 - 0.4 \mu\text{m}$  (sqrt(n) error law with  $n=4$ ). Usually we found very close values for the measured  $2w_c$  for the 3 device D1,D2,D3. The photolithographic process was checked to be

## Chapter 6: Experimental study

uniform Once we had measured the waveguide width  $w_c$ , we could choose an appropriate diffusion time for the ion exchange, according what we explained in Section 6.1.

Fig 6.4: The waveguide width measurement set-up



### 6.2.5 Ion-exchange

After the above measurement, the sample was ready for the ion exchange bath, that took place in a furnace. The furnace has a vertical core and can be used in the 20 to 1200° C range . The temperature can be fixed by a temperature controller to within 1° C. The potassium nitrate crystals ( $\text{KNO}_3$ ) are placed in a steel crucible inside the furnace which is closed at the top with an asbestos cover. A small hole in the cover allows the insertion of a brass rod terminating in a steel clip which is used to hold two substrates and to lower them into the melt without opening the cover. The fact that the process takes place in a liquid smooths out any temperature gradient along the length of the substrate ( because of convection currents arising from non uniform heating) and also any temporal fluctuations.

Using gloves the substrate was placed in the steel clip to hold it in the furnace. The whole assembly was suspended over the melt for a heating period of 10 minutes to bring the entire substrate to the exchange temperature and then lowered in the  $\text{KNO}_3$  melt. The pre-heating stage ensures that the exchange begins at the right temperature and prevents the creation of surface cracks resulting from a thermal shock. After the desired period of time, the substrate was removed from the melt and from the furnace, the whole process lasting about 15 seconds until the residual  $\text{KNO}_3$  recrystallized on the glass, indicating that the exchange had ended. The sample was taken from the clip and put in a box to cool down.

### 6.2.6 Preparation of the samples for measurement

#### 1) Width measurement

Following the ion exchange, the waveguide width on the diffusion mask was measured again, as a verification.

#### 2) Diamond cutting:

When the extinction ratio measurement is considered, we want to keep the propagation loss as low as possible. We do not want the output and input branch of a device to be too long. Obviously, four 8 mm long devices occupy only a small space on a 75 mm long substrate. Before our measurement tests we had to cut our samples (See Fig 6.5). Using a microscope to inspect

## Chapter 6: Experimental study

---

the samples, as they were still coated with the diffusion mask, we could spot the input and output branches of the devices. Using a diamond cutter, we proceeded to cut off small pieces each with a device on it. When cutting we took care to keep enough separation between the output branches so that during the extinction ratio measurement tests the two output spots were distinguishable.

The cutting was also done such that there was only one input branch, to make sure that we had the same input conditions in the measurement as those assumed in the theory: when measuring coupling light from a multimode fiber at the input (diameter  $20\mu\text{m}$ ) (See Section 6.3.1) all of the input light should be coupled in one of the input arm of the device and none of it in the other (equal excitation of the symmetric and antisymmetric modes) (See Fig 6.5). Much care should be taken when cutting. If the edges of the sample are too rough then the measurement will be difficult if not impossible. After cutting, the sample was dipped into an etching solution to remove the Al diffusion mask and washed clean, ready to be tested. The different stages of the fabrication process are depicted Fig 6.6.

Fig 6.5: Diamond cutting of a sample

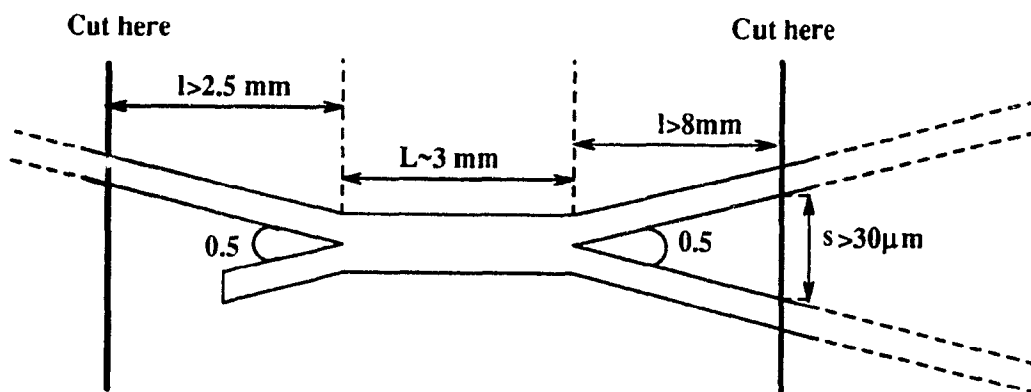
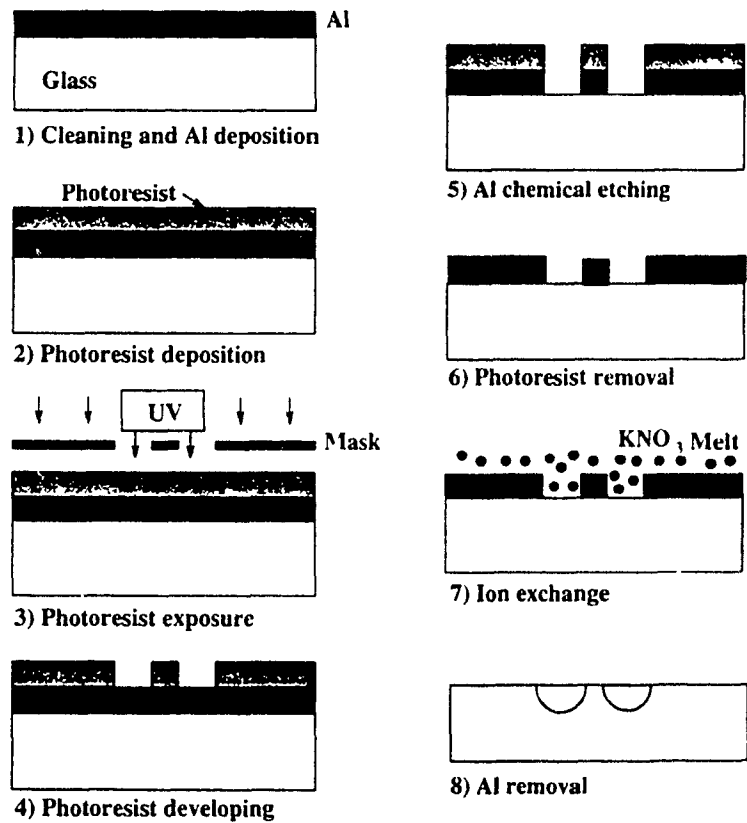


Fig 6.6: Device fabrication process



### 6.3 Device testing

#### 6.3.1 Extinction ratio measurement tests

The measurement setup used to test our devices is described Fig 6.7. When we measured one device, one of our concern was to get as much power as possible into the waveguide and as little as possible to scatter into the planar structure that surrounds it. This was not easy since the

channels were at the same time small and weakly guiding, due to the very small index change. We found that fiber butt-coupling (See Fig 6.8) was a practical solution. Mounting the sample on an adjustable plate, we could move it in the x,y,z directions on micropositioners. We succeeded in coupling a satisfying amount of the light into our devices, from a multimode fiber output.

A 0.6328 $\mu\text{m}$  He-Ne laser was used to help with the alignment. Indeed, using visible light is more convenient when one just wants to find the waveguide on the substrate. Adjusting the focusing length of the output lens  $L_2$  we could obtain good definition for the output spots (output near-field pattern) at the end facet of our samples (output ports 1 and 2 see Fig 4.1 Chapter 4).

Once good coupling was obtained, we connected the fiber to the 1.31-1.55 $\mu\text{m}$  laser diode light sources. Turning on the IR vidicon camera, we could look on the TV monitor connected to the camera, at the output spots at the end facet of the samples. Usually, we had to slightly adjust the focus as we changed wavelength, to get the best definition. A TE-TM polarizer was placed, at the output of the device. Indeed, we mentioned before, that the devices were polarization dependent (see Chapter 4,5) As, in the fabrication process, the design parameters  $L$  and  $t_d$  were optimized for TM mode operation (See section 6.1), when measuring a device, we used the TE-TM polarizer to select only the TM mode at the output of the device.

In order to actually measure the extinction ratios, the video signal was also observed on the oscilloscope, connected to the camera, by a raster scan. At each wavelength, by measuring the heights of the two peaks corresponding to the two output spots of one device (output ports 1 and 2), we could find the extinction ratio. In the best cases, of course, one of the two spots/peaks would be very weak, while the other very strong at one wavelength and reciprocally at the other ( $ER(\lambda=1.31,1.55\mu\text{m}) > 15$  dB). This last point is elaborated in the next section where examples of actual measurements are presented.

### 6.3.2 Experimental results

As shown in Fig 6.9 and 6.11, and in Fig 6.10 and 6.12 respectively, pictures of the output spots at the sample end facet, as well as the video signal on the oscilloscope screen, were taken for two devices. The design parameters for these two devices are those proposed in Section 6.1 for D2:  $L_2=2930\mu\text{m}$  (Fig 6.9-10) and D1:  $L_1=3100\mu\text{m}$  (Fig 6.11-12).

For the device (D2), in Fig 6.10, the heights of the peaks, corresponding to the intensity of the output spots at the output ports 1 and 2 of the device, can be measured with a ruler to be

## Chapter 6: Experimental study

---

$h_1 \approx 0.25\text{cm}$ ,  $h_2 \approx 4.2\text{cm}$  at  $1.31\mu\text{m}$  (See Fig 6.10a) and  $h_1 \approx 4.2\text{cm}$ ,  $h_2 \approx 0.25\text{cm}$  at  $1.55\mu\text{m}$  (See Fig 6.10b). The photodetector in the Hamamatsu camera is a square root law detector: the measured height of the peaks are proportional to the square root of the light intensity in each port. Therefore, the extinction ratio in dB for device D2, should be calculated as:  $ER(1.31\mu\text{m}) \approx 10\log[(0.25/4.2)]^2 \approx -20\text{dB}$ ,  $ER(1.55\mu\text{m}) \approx 10\log[(0.25/4.2)]^2 \approx -20\text{dB}$ .

For the device D1 (Fig 6.11-6.12) we can measure  $h_1 \approx 0.4\text{cm}$ ,  $h_2 \approx 4.4\text{cm}$  at  $\lambda = 1.31\mu\text{m}$  (See Fig 6.12a), and  $h_1 \approx 0.6\text{cm}$ ,  $h_2 \approx 4\text{cm}$  at  $\lambda = 1.55\mu\text{m}$  (See Fig 6.12b). The extinction ratios for this device are, therefore,  $ER(1.31\mu\text{m}) \approx 20\text{dB}$ ,  $ER(1.55\mu\text{m}) \approx 15\text{dB}$ .

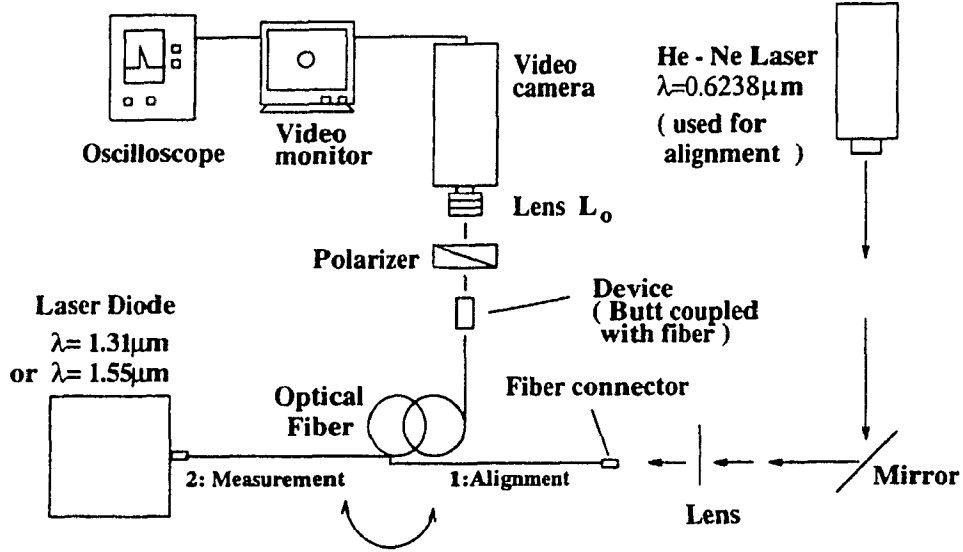
In both cases, the presence of spurious peaks in the video signal in both cases should be noted. After cutting (see Section 6.2.6), the output edge of the sample is not very smooth. Because of the surface roughness, part of the output light is diffracted, giving rise to these peaks.

Devices with the two other design parameters proposed in 6.1 were tested. The best experimental results are reported in Table 6.1. Extinction ratios around 20 dB were measured. The theoretical extinction ratios are supposed to be around -35 dB (optimized design). The measured values might have been limited by the possible non linearity in the photodetector of our Hamamatsu camera. Actual extinction ratios could be higher. Overall the agreement with the theory is good, given the tight tolerance on the design parameters, especially  $w$  which was found hard to realize and measure experimentally.

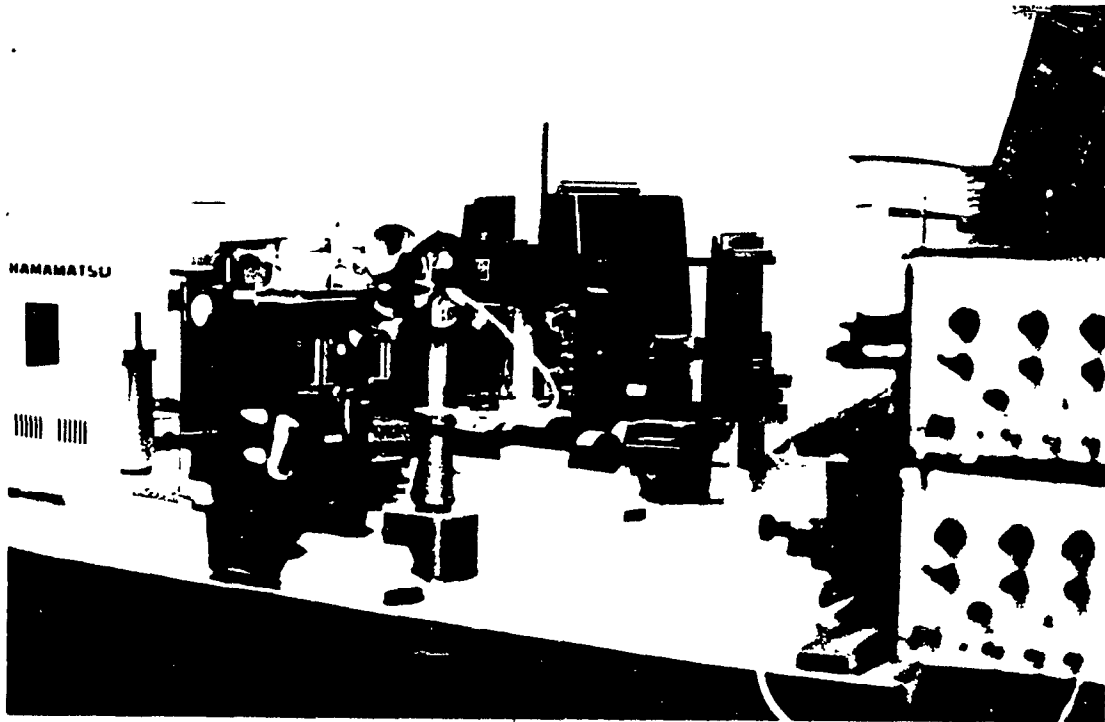
## 6.4 Conclusion

Despite the difficulties of the fabrication process, we succeeded in realizing devices designed for TM polarization with satisfactory extinction ratios (ER around 20 dB). This is a reasonable assessment of the design procedure. Due to the limitation of the photodetector in the vidicon camera, due to non linear and noise factors, the actual extinction ratios should be somewhat higher, hence offering good agreement in comparison with the designed ER values.

Fig 6.7a,b: Measurement set-up

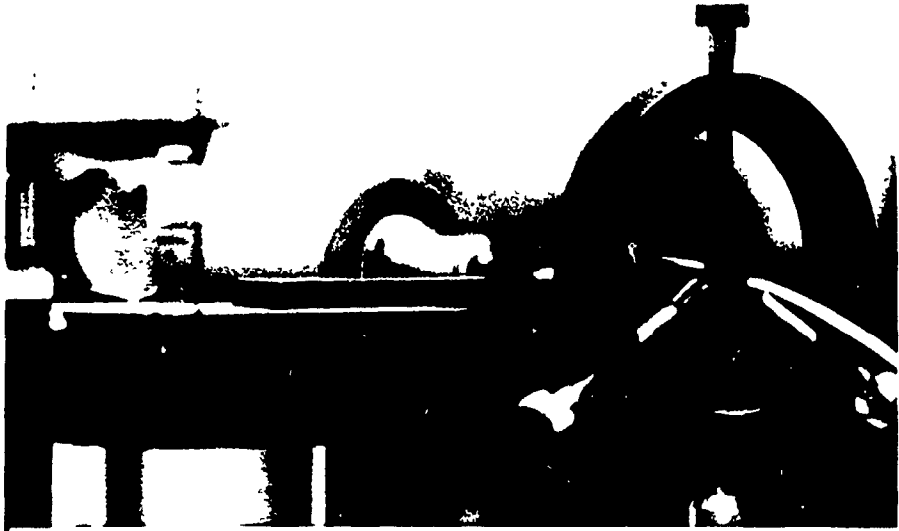


6.7a) Schematic representation



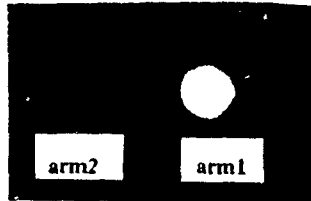
6.7b) Picture of the set-up

Fig 6.8: Fiber butt coupling

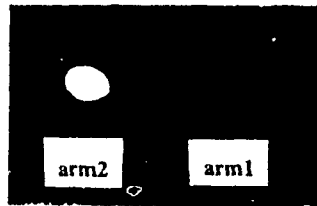


(In Figs 6.9 and 6.10 the parameters are:  
 $\alpha=0.5^\circ$ ,  $L=2930\mu\text{m}$ ,  $2w_c=11.6\mu\text{m}$ ,  $t_d=270\text{min}$ , TM modes)

Fig 6.9: Output spots at end facet

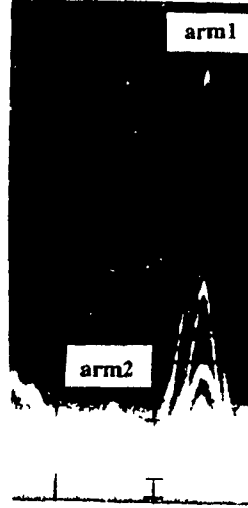


6.9a)  $\lambda=1.55\mu\text{m}$

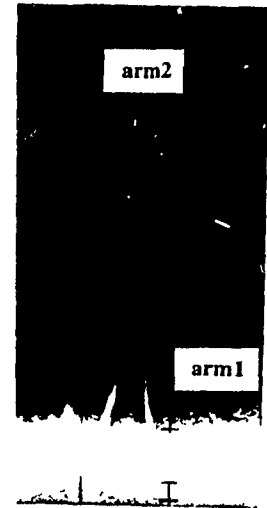


6.9b)  $\lambda=1.31\mu\text{m}$

Fig 6.10: Video signal on the oscilloscope



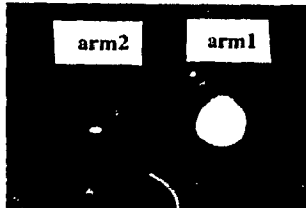
6.10a)  $\lambda=1.55\mu\text{m}$



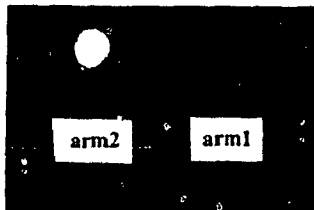
6.10b)  $\lambda=1.31\mu\text{m}$

(In Figs 6.11 and 6.12 the parameters are:  
 $\alpha=0.5^\circ$ ,  $L=3100\mu\text{m}$ ,  $2w_c=12.0\mu\text{m}$ ,  $t_d=255\text{min}$ , TM modes)

Fig 6.11: Output spots at end facet

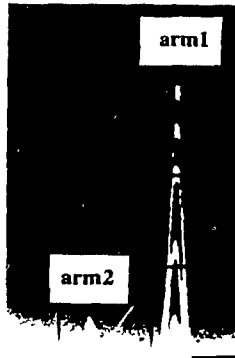


6.11a)  $\lambda=1.55\mu\text{m}$

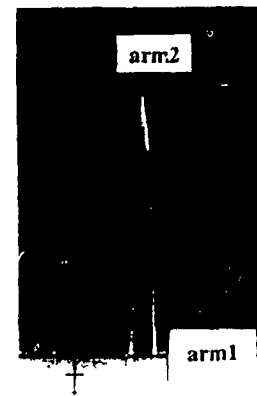


6.11b)  $\lambda=1.31\mu\text{m}$

Fig 6.12: Video signal on the oscilloscope



6.12a)  $\lambda=1.55\mu\text{m}$



6.12b)  $\lambda=1.31\mu\text{m}$

Tab 6.1: Measured extinction ratios (TM modes,  $\alpha=0.5^\circ$ )

Fabrication conditions	ER( $\lambda=1.31\mu\text{m}$ ) (dB)	ER( $\lambda=1.55\mu\text{m}$ ) (dB)
$2w_c=12.0\mu\text{m}$ , $L=3100\mu\text{m}, t_d=255\text{min}$	20	15
$2w_c=11.6\mu\text{m}$ , $L=2930\mu\text{m}, t_d=270\text{min}$	20	20
$2w_c=11.2\mu\text{m}$ , $L=2710\mu\text{m}, t_d=280\text{min}$	15	18
$2w_c=11.8\mu\text{m}$ , $L=2710\mu\text{m}, t_d=255\text{min}$	15	20

The values given for  $2w_c$  are measured values (See Section 6.2.). The uncertainty on these values is about  $\pm 0.2\mu\text{m}$ .

## CHAPTER 7

### CONCLUSION

The goal of this thesis was to design and fabricate a widened X-branch demultiplexer in glass by a single  $K^+$ - $Na^+$  ion exchange technique.

In the design part of the work, we followed the procedure indicated in introduction (See Fig 1.2). Firstly, we presented the numerical method used in this thesis: the effective index method (EIM) and the Runge-Kutta method. In Chapter 3, we solved the diffusion equation for channel waveguides built by the single  $K^+$ - $Na^+$  ion-exchange. From the calculated index profile, we could derive an improved model (erf fit function) for the effective index profile  $N_{eff}(x)$ , in the lateral direction, in the EIM, of the widened X-branch. Thus, the effective index method could be applied with improved accuracy in Chapter 4 to calculate design values and tolerance figures for the device. We verified that the improved side diffused model we had derived for the lateral effective index was a much better model than the classic but rough step index model. The devices were found to be polarization dependent, due to the properties of the  $K^+$ - $Na^+$  ion exchange. In Chapter 5 the beam propagation method was used to simulate the device. Using the BPM we could take into account the effect of the radiation modes, which had been neglected in Chapter 4. Slightly corrected figures for the design values and tolerances were thereby calculated. Extinction ratio around -35 dB were calculated for optimized device at both TE, TM polarizations. In the experimental part of the work (Chapter 6), we succeeded in fabricating devices designed for TM polarization with satisfying extinction ratio (about -20 dB). The discrepancies between the experimental and theoretical results were attributed to the limitations of the fabrication process (photolithography) and non linearities in the measurement apparatus.

In the next sections, we propose and discuss some possible improvements to the design and experimental procedure that could help to optimize the performances of the widened X-branch demultiplexer. Then we conclude on the prospects for this type of structure, for wavelength demultiplexing applications.

### Possible improvements

#### -Design procedure:

The best method to minimize the design error is probably to use a direct 3D FD-BPM algorithm without using the effective index method which always introduces some error (See Chapter 2 and 4, [1-2]). Unfortunately this method is extremely time consuming and there is always the problem to find an accurate model for the index profile of the structure to be used in the BPM simulations. Solving the diffusion equation with the simplified boundary conditions as done in Chapter 3 gives a good idea of the solutions, but still one has to fit the numerical solution by an analytical solution to be able to use the BPM efficiently.

#### -Experimental work:

. Post-annealing: In our experimental study, we did not really examine radiation losses as these measurements require a lot of time. However we can expect to obtain quite some radiation losses from structure fabricated by one-step-ion exchange as reported by Wilkinson [3]. Excessive radiation losses are not acceptable if one wants to implement the device in a real communication system. Also, we know that the extinction ratio can be reduced as a result of large radiation losses (See Chapter 5). This might have been one of the factor that limited our measured extinction ratios to about- 20 dB. In a further study of the device, this problem should be adressed. An alternative fabrication procedure to decrease the radiation losses is to use postannealed waveguides. After the first diffusion the aluminium mask can be removed from the glass samples and a second ion exchange can take place or simple thermal post annealing. Waveguides obtained with this technique have smoother edges (see Fig Chapter3) and, hence, scattering is reduced [3-4]. Also, when we calculated the effective profile for the post annealed waveguides we found that it was closer to a steplike one. In the case of our widened X-branch, this means that isolation between the two output channels should increase using this technique. Another way to deal with this isolation problem would be to use ion milling of the sides of the diffused waveguides.

. Cascaded structures: To compensate for the design errors and increase the extinction ratio cascaded structures, as mentioned in Chapter 4.

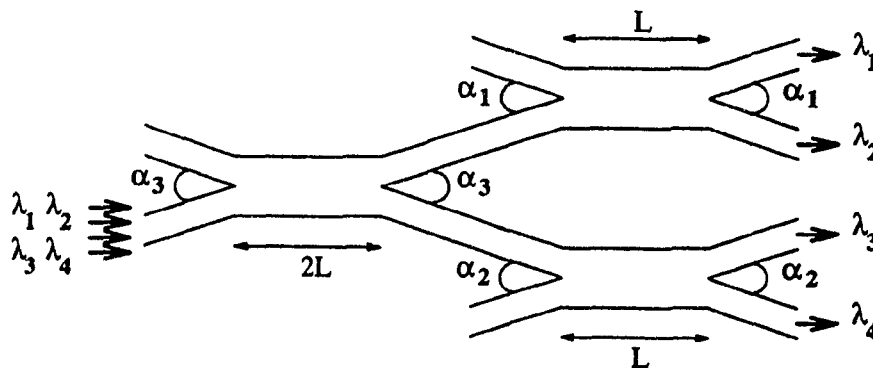
## Chapter 7: Conclusion

. Polarization dependence: Using  $\text{Na}^+\text{-K}^+$  ion-exchange, polarization dependence of the device is to be expected. Silver ion-exchange might be an alternative technique, however it would probably lead to increased losses and increased complexity in the fabrication procedure (anodized mask required [3] )

## Prospects

Already, given its simplicity of fabrication (single photolithographic process), the widened X-branch structure is a competitive structure compared to other two-mode interference (TMI) structures. The requirements on the dimension parameters are tight like for any TMI devices but no symmetry problems have to be considered as in the case of directional coupler for instance. By using cascaded structures, one can expect to improve somewhat the extinction ratios and at the same time separate several wavelengths [5-6] (see Fig 7.1).

Fig 7.1: Multichannel wavelength demultiplexer using cascaded widened X-branch



## References

- [1] Y. Chung and N. Dagli, "Analysis of a Z-invariant and Z-variant semiconductor rib waveguides by explicit finite difference beam propagation method with nonuniform mesh configuration", *IEEE J. of Quantum Electron.*, Vol 27, pp.2297-2305, 1991.
- [2] M. D. Feit and J. A. Fleck, "An analysis of intersecting diffused waveguides", *IEEE J. of Quantum Electron.*, Vol 21, pp.1799-1804, 1985.
- [3] R.G. Walker, C. D. Wilkinson and J. A. Wilkinson, "Integrated optical waveguide made by silver ion exchange in glass 1,2", *Applied Opt.*, Vol 22, pp.1923-1933, 1983.
- [4] H. Zhenguang, R. Srivastava, R. V. Ramaswamy, " Low-loss small-mode passive waveguides and near adiabatic tapers in BK7 glass", *IEEE J of Lightwave Tech.*, Vol 7, pp.1590-1595, 1989.
- [5] K. Imoto, H. Sano, M. Miyazaki, H. Uethuka and M Mineda, "Compensation for fabrication induced wavelength shift in a coupled waveguide type multi-demultiplexer", *Applied Opt.*, Vol 28, pp.1904-1907, 1989.
- [6] Y.Chung, J.C. Yi , S.H. Kim and S.S. Choi, "Analysis of a tunable two-mode interference wavelength division multiplexer/demultiplexer", *IEEE J. of Lightwave Tech.*, Vol 7, pp.766-776, 1989.